Synthetic topological quantum matter in nanostructured 2D materials for quantum information processing

Alina Wania Rodrigues

Thesis submitted to the University of Ottawa
in partial fulfillment of the requirements for the
PhD degree in Physics

Department of Physics
Faculty of Sciences
University of Ottawa

Abstract

In this thesis, we contribute to understanding the electronic properties of two-dimensional materials, with a strong emphasis on graphene-based nanostructures, such as twisted multilayer graphene and triangular graphene quantum dots. The thesis is organized into six chapters, including an introduction and a conclusion.

In Chapter 2, we present the theoretical methods used to carry out the calculations in this thesis. We begin by defining the geometry of twisted graphene multilayers, which serves as the basis for the methods described later. We then introduce the general many-body problem and focus on various approximations commonly used to solve it. The tight-binding model is derived, and its application to moiré materials is demonstrated, followed by a comparison with the continuum approach. We then discuss mean-field methods, specifically Density Functional Theory (DFT) and Hartree-Fock. In the final section, we introduce methods for studying electron correlations and evaluate their applicability to specific systems. These include the Configuration Interaction (CI) method, hybrid approaches combining DFT and CI, and tensor network techniques.

Chapters 3-5 include the results of our work. We first focus on twisted graphene multilayers - magic angle twisted bilayer graphene and mirror-symmetric twisted trilayer graphene. In Chapter 3, we start with a Hofstadter's butterfly spectrum for the magic angle twisted bilayer graphene obtained using an *ab initio* based multi-million atom tight-binding model. A nanoribbon geometry is studied, and the quantum size effects for the sample widths up to 1μ m are analyzed. For sufficiently wide ribbons, where the role of the finite geometry is minimized, we obtain and plot the Hofstadter spectrum and identify the in-gap Chern numbers by counting the total number of chiral edge states crossing these gaps. Subsequently, we examine the Wannier diagrams to identify the insulating states at charge neutrality. We establish the presence of three types of electronic states: moiré, mixed, and conventional.

We then move on to study trilayer structures in Chapter 4. Here, the electronic properties are described by a Hubbard model with long-range tunnelling matrix elements. The

electronic properties are obtained by solving the mean-field Hubbard model. We obtain the band structure with characteristic flat bands and a Dirac cone. At charge neutrality, turning on electron-electron interactions results in a metallic to antiferromagnetic phase transition, for Hubbard interaction strength considerably smaller than in other graphene multilayers. We analyze the stability of the antiferromagnetic state against the symmetry-breaking induced by hexagonal boron nitride encapsulation and mirror symmetry-breaking caused by the application of electric fields that mix the Dirac cone with the flat bands. Additionally, we explore the topological properties of the system, revealing a hidden quantum geometry.

In Chapter 5, we focus on triangular graphene quantum dots. We present a method for probing the wave functions of a degenerate shell in such dots by introducing a localized substitutional impurity. Specifically, we demonstrate this approach using a triangular graphene quantum dot containing a nitrogen impurity. Starting from the analytical solution for the degenerate states of a pristine all-carbon triangular graphene quantum dot, we predict the structure of the zero-energy shell in the presence of an impurity. We show that the impurity enables selective probing of the wave functions at the carbon site where it is located. These predictions are validated through comparison with tight-binding and *ab initio* calculations and experimental results. We then study a triangular graphene quantum dot with armchair edges with a nitrogen impurity. We use a technique combining the Density Functional Theory and Configuration Interactions to analyze the energy spectrum and determine the effect the nitrogen impurity has on it. Additionally, we show that including excitations lowers the ground state energy for all considered geometries. Finally, we focus on bilayer triangular graphene dots with zig-zag edges and analyze the behaviour of the degenerate zero-energy shell as a function of size and the twist angle.

Chapter 6 includes conclusions and prospects for future work.

Acknowledgements

I would like to thank my supervisor, Prof. Pawel Hawrylak, for his guidance, support, and encouragement throughout the course of my thesis. His advice and insight have been invaluable to both this project and my growth as a researcher. I am also especially grateful for all his support outside academia - settling into a new country, new culture - thank you for making the process smoother.

I also wish to thank two special figures in my scientific journey: Dr. Maciej Bieniek and Dr. Daniel Miravet. Maciej has been with me since the very beginning of my research path - been a constant presence throughout my B.Sc., M.Sc., and Ph.D. studies. His great patience, insightful guidance, and steady encouragement have been instrumental at every stage of my academic development. Daniel has provided invaluable support throughout my Ph.D., from my comprehensive exam to the final stages of this thesis. His mentorship, generosity with his time, and thoughtful advice have made a lasting impact - not only as a teacher and mentor, but also a friend.

I also would like to thank all the members of the Quantum Theory group - I have learned a lot from you, particularly throughout the group meetings. I am especially grateful to Dr. Guan-Hao Peng, Dr. Iann Cunha, and Dr. Ludmila Szulakowska who were not only great colleagues, but also trusted friends.

I am also thankful to Dr. Pawel Potasz and Dr. Marek Korkusinski, from whom I have learned a great deal - not only through their scientific knowledge, but through their conduct and approach to research.

I also wish to thank Dr. Manuel Ferrer Garcia for being my coffee buddy and office mate, and making sure that there was more to my day than just physics.

I am deeply grateful to my parents for their support, love, and encouragement throughout this journey.

Finally, I would like to thank my husband, Kaleb, whose unfailing presence has been a constant source of strength throughout the trials and triumphs of my Ph.D. His belief

in me, especially during times when I struggled to believe in myself, has meant more than words can express. I am profoundly grateful for his thoughtful advice, emotional support, and steadfast encouragement, all of which have carried me through this experience.

Acronyms

MLG	Monolayer graphene
BLG	Bilayer graphene
TGQD	Triangular graphene quantum dot
MATBG	Magic angle twisted bilayer graphene
TBG	Twisted bilayer graphene
TTG	Twisted trilayer graphene
TB	Tight-binding
NN	Nearest neighbour
DFT	Density functional theory
HF	Hartree-Fock
CI	Configuration interaction
TN	Tensor Network
MPS	Matrix product state

Contents

List of Figures

Chapter 1

Introduction

1.1 Introduction to 2D materials

Since the mechanical exfoliation of monolayer graphene from bulk graphite in 2004 [4], the field of 2D materials has grown rapidly. The success of graphene not only demonstrated the viability of isolating stable, atomically thin crystals but also sparked intense interest in discovering other 2D materials with complementary properties or entirely new functionalities.

This effort soon led to the discovery and isolation of a broader class of 2D materials, including the family of transition metal dichalcogenides (TMDs), such as MoS_2, WS_2, and others [5]. These materials, unlike graphene, can be semiconducting or insulating, thereby enabling a wider range of applications in electronics, optoelectronics, and valleytronics. The field has since expanded to include dozens of other layered compounds, including hexagonal boron nitride (hBN), black phosphorus, and various magnetic or topological 2D materials, each offering distinct physical properties [6].

A defining feature of 2D materials is the possibility to tailor their electronic, optical, and mechanical behaviour without altering their chemical composition. This can be achieved through external means such as electrostatic gating, applying strain, size quantization,

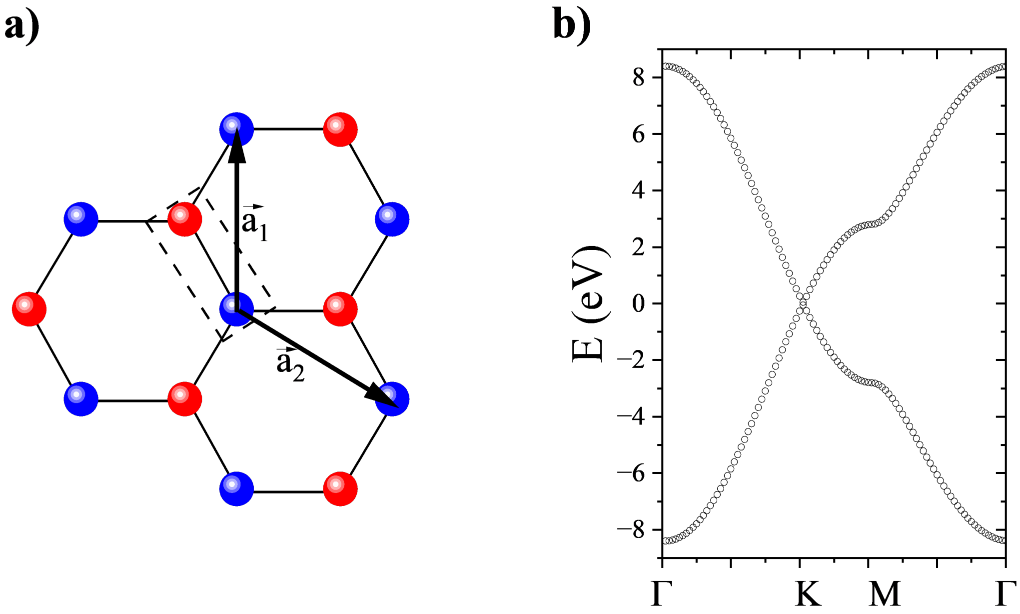

Figure 1.1: Graphene: (a) lattice geometry with two atoms A (red dots) and B (blue dots) in a unit cell, marked by a dashed line. Two primitive lattice vectors $\vec{a}_1$ and $\vec{a}_2$ are denoted with black arrows. (b) Low energy spectrum of graphene along the $\Gamma - K - M - \Gamma$ path in the Brillouin zone.

introducing moiré patterns by stacking different layers with relative twists, or modifying the dielectric environment. In particular, stacking individual 2D layers into heterostructures or applying a small twist angle between them can lead to emergent phenomena that are not present in the individual components, such as flat electronic bands, superconductivity, and correlated insulating states [7–9]. These tunable properties make 2D materials a rich platform for exploring fundamental physics and developing next-generation nanoscale devices.

1.1.1 Graphene

Monolayer graphene is a two-dimensional (2D) material composed of carbon atoms arranged in a honeycomb lattice. Its unit cell contains two carbon atoms, labelled A and B, which form two triangular sublattices, see Fig. 1.1 (a). Theoretical foundations for graphene were laid in 1946 by P.R. Wallace, who analyzed the band structure of graphite by first considering an isolated graphene layer [10]. He was the first to solve the tight-binding model for this system and derive its distinctive band structure, characterized by Dirac cones that touch at the K points of the Brillouin zone (BZ).

Despite considerable theoretical effort over subsequent decades [11–14], graphene remained experimentally elusive due to technological limitations. It was not until 2004 that Geim and Novoselov successfully isolated a single atomic layer of graphite using mechanical exfoliation with adhesive tape, a breakthrough that earned them the Nobel Prize in 2010. This discovery sparked widespread interest in graphene and other 2D materials. Graphene was soon dubbed the 'wonder material of the 21st century', due to its exceptional properties: high carrier mobility exceeding 47,000 $\mathrm{cm}^2/\mathrm{Vs}$ under ambient conditions [15], excellent conductivity, mechanical strength, unique optical characteristics, and exhibiting the quantum Hall effect [16].

The presence of two inequivalent sublattices enables the definition of a quantum degree of freedom known as pseudospin. It plays a crucial role in shaping graphene's unique transport properties, including its high carrier mobility and topological characteristics such as non-zero Berry curvature. Graphene is a gapless semimetal with a vanishing density of states at the Fermi level and linear quasiparticle dispersion near the K points (see Fig. 1.1 (b)). The direction of the pseudospin is momentum-dependent, leading to chiral, massless Dirac fermion excitations that travel at a velocity of approximately 1000000 m/s. These relativistic, chiral carriers give rise to exotic phenomena such as Berry phase accumulation and Klein tunnelling [17, 18].

The relativistic nature of charge carriers in graphene significantly impacts the role of electron-electron interactions in shaping its electronic properties. In contrast to non-relativistic systems—where the balance between kinetic and Coulomb energy depends on the typical distance between electrons—in graphene, this ratio is instead determined by the Fermi velocity and the degree of dielectric screening. Consequently, graphene's electronic characteristics, such as the carrier mobility or presence of a band gap, are highly dependent on the surrounding environment [19].

1.1.2 Triangular graphene quantum dots

Synthetic correlated electron systems provide a powerful platform for engineering topological quantum matter with emergent properties that differ dramatically from those of their individual components. Notable examples include superconductivity in twisted layers of natively non-superconducting components, ferromagnetism, and the incompressible liquids of the fractional quantum Hall effect. These emergent phenomena arise from strong electronic correlations and entanglement driven by electron-electron (e–e) interactions within flat bands—highly degenerate electronic shells. Flat bands can be realized in the lowest Landau level of a 2D electron gas [20–26], in twisted bilayer graphene (TBG) [8, 9, 27], or through the on-surface synthesis of triangular graphene quantum dots (TGQDs) with broken sublattice symmetry [3, 28–34].

Graphene quantum dots (GQDs) are promising candidates for a broad range of applications in optoelectronics, photonics, and electronics. As carbon-based light emitters, they offer outstanding stability, low production costs, and material abundance. As a result, the design and development of light-emitting GQDs have garnered significant interest over the past two decades. Among various geometries, equilateral triangular GQDs have attracted particular attention due to the tunability of their electronic structure via both size and edge configuration [3, 28–34]. Graphene edges can be classified into two distinct types: armchair and zigzag (see Fig. 1.2). Zigzag edges break sublattice symmetry by introducing an imbalance between the number of A and B sublattice atoms, leading to the emergence of a degenerate zero-energy shell. In the following, we examine both edge types and discuss the resulting electronic and magnetic properties of the corresponding quantum dots.

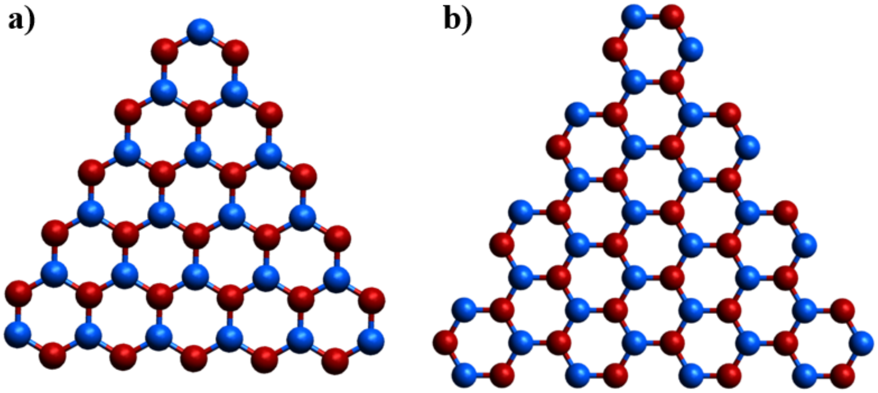

Figure 1.2: TGQD: (a) TGQD with zig-zag edges. (b) TGQD with armchair edges, A sublattice is marked in red, B in blue.

Triangular graphene quantum dots with zig-zag edges

TGQDs with zig-zag edges (Fig. 1.2 (a)) can now be fabricated with atomic precision via on-surface synthesis, enabling the controlled design of a degenerate electronic shell at the Dirac point [3, 16, 28–37]. In recent years, interest in TGQDs has grown significantly, driven by advancements in their synthesis across various sizes and configurations, progress previously hindered by the structures' high chemical reactivity.

The presence of zigzag edges induces a sublattice imbalance in TGQDs, giving rise to a shell of degenerate states near the Fermi energy, with the number of such states increasing linearly with system size. This behaviour was first demonstrated at the single-particle level using analytical and tight-binding methods [38, 39], and has since been corroborated by mean-field approaches—including *ab initio* and Hartree-Fock calculations—as well as by exact diagonalization studies [40–43].

The magnetic properties of these quantum dots can be understood through Lieb's theorem for the bipartite Hubbard model, which predicts that the ground-state total spin is determined by the difference in the number of A and B sublattice atoms in the graphene lattice [44].

To open a band gap in the energy spectrum of TGQDs and make them suitable for logic device applications, one can employ strategies such as size quantization, chemical modification, or adding a second layer combined with an external electric field. We note, that the gap we refer to here is a quantum dot gap defined as the difference in energy between the highest occupied state and the lowest unoccupied one. It is a different concept than the fundamental semi-conductor gap [45].

Another class of TGQD are TGQDs with a nitrogen defect, in which one or more of the carbon atoms have been replaced by nitrogen [46–49]. For example, N-doped TGQD, with five benzene rings in a given edge, consisting of 46 atoms, has been recently realized experimentally [3, 50]. Replacing a carbon atom with a nitrogen atom introduces an extra electron and proton. This substitution removes an unpaired electron from one sublattice, thereby altering the system's total spin.

Triangular graphene quantum dots with armchair edges

In TGQDs with armchair edges (Fig. 1.2 (b)), sublattice symmetry is preserved, and as a result, a degenerate zero-energy shell does not form. Instead, a band gap opens around the Fermi energy, whose magnitude can be tuned by varying the size of the system—the larger the triangle, the smaller the gap. Remarkably, this size-dependent tunability allows the band gap to span a broad spectral range, from the ultraviolet to the terahertz regime [51–54].

This tunable optical response makes armchair-edged TGQDs particularly attractive for optoelectronic applications such as photodetectors, light-emitting devices, and quantum information technologies. Moreover, the absence of zero-energy states simplifies their many-body spectrum and facilitates clearer identification of excitonic effects and impurity-induced states. From a theoretical standpoint, these systems offer a clean platform for exploring confinement, edge effects, and electron–electron interactions in low-dimensional graphene-based nanostructures. The well-defined energy gap also makes them promising candidates for integrating graphene with conventional semiconductor technologies.

1.1.3 Moiré materials

When two or more 2D crystals are stacked, lattice mismatch or layer misalignment can give rise to moiré patterns. This phenomenon was observed relatively early using scanning tunnelling microscopy (STM) in multilayer graphene samples [55], as well as in graphene placed on an hBN substrate. Theoretical calculations for bilayer graphene predated these experimental observations and predicted a renormalization of the Fermi velocity [56]. In 2011, the seminal work by Bistritzer and MacDonald [27] predicted a flattening of the electronic bands near the Fermi level at a so-called magic twist angle, suggesting that the resulting crystal becomes strongly correlated and can host a variety of quantum phases. It is so because the width of the flat bands is of the order of a few meV, so that the electron-electron correlations are dominant and can give rise to correlated phenomena. This theory awaited experimental confirmation for seven years, which finally arrived in 2018 [8, 9], when a necessary tear-and-stack technique was perfected. It allows precise control of the twist angle, which is necessary to produce specific TBG. The MIT group observed, first, correlated insulating behaviour and subsequently superconductivity in bilayer graphene twisted by $\theta = 1.1^\circ$, the predicted magic angle.

This discovery was remarkable not only because untwisted bilayer graphene is a semimetal, but also due to the unconventional nature of superconductivity in magic-angle twisted bilayer graphene (MATBG), which remains poorly understood. It arises from an electron system with an exceptionally low carrier density, yet displays strong coupling and a critical temperature unusually high relative to its ultra-low Fermi temperature, comparable only to high-temperature superconductors [57]. The presence of strong electronic correlations initially prompted comparisons to other correlated systems like cuprates, pnictides, and heavy fermion compounds, suggesting a correlation-driven mechanism. However, recent studies have not excluded a conventional electron–phonon origin. The pairing symmetry still remains an open question [58–60]. The discovery of topologically nontrivial bands in MATBG has further raised the possibility of topological superconductivity.

Following MATBG, a wide variety of moiré systems have been realized, featuring different numbers of layers, twist angle sequences and materials. These include, but are not limited to, mirror-symmetric trilayers [61–63], helical trilayers [64], double bilayers [65], and pentalayers [66]. Several of these systems have been shown to host a rich array of correlated and topological states, such as correlated insulators [8,67–72], the quantum anomalous Hall effect [73], ferromagnetism [74], and a generalized Wigner crystal state [75].

The most characteristic feature of all of these materials is the presence of tunable flat bands. Those can be controlled primarily through the twist angle, which can now be precisely adjusted. Changing the twist angle changes the ratio between the interaction strength and kinetic energy, allowing for modelling systems in weak, intermediate, and strong coupling regimes. Other tuning knobs are strain, alignment with the substrate, and electric field, all of which are still vigorously studied.

We now focus on four representative moiré materials: magic-angle twisted bilayer graphene, mirror-symmetric twisted trilayer graphene, rhombohedral graphene, and twisted TMDs.

Magic angle twisted bilayer graphene

MATBG is the most and best studied member of the moiré materials family, both experimentally [8,9,73,74,76–90] and theoretically [7,91–179]. Since the discovery of correlated insulating and superconducting states in MATBG, various other emergent phases have been observed. These include correlated Chern insulators, quantum Hall insulators, ferromagnetism, orbital magnetism, and many others [86,87,180–182].

Here, the moiré potential gives rise to two nearly flat energy bands — a valence and a conduction band — near charge neutrality. Owing to the presence of spin, valley, and layer degrees of freedom, there are numerous possible ground states at partial fillings of these flat bands, where the filling is measured in terms of electrons per moiré unit cell. The eight flat bands are typically described using the filling factor $\nu \in [-4, 4]$, with $\nu = -4$ corresponding to empty flat bands and $\nu = 4$ to fully filled bands. The interacting electrons in these bands give rise to a rich landscape of strongly correlated phases, offering a unique platform to explore the interplay between electron-electron interactions and topology.

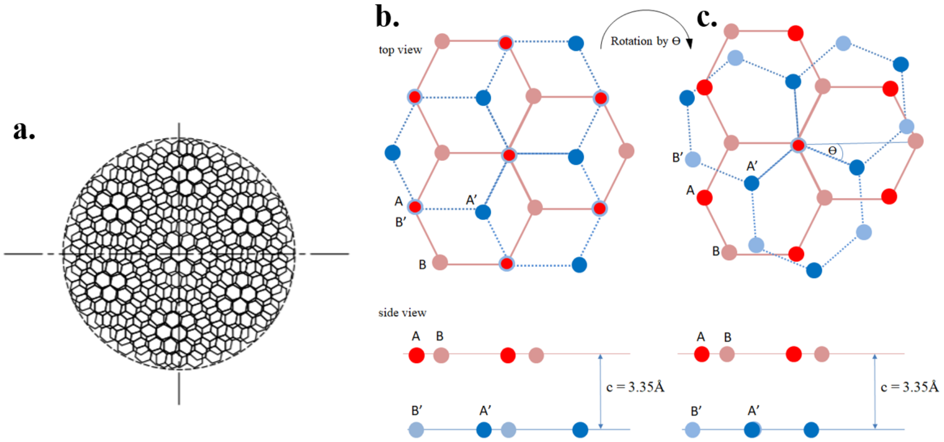

Figure 1.3: TBG: (a) Moiré pattern forming for two graphene sheets twisted by $\theta = 11.4°$. (b) Graphene lattice before and (c) after the twist by θ. Red dots refer to A sublattice, blue atoms to B. The top panel shows the top view of the lattice, and the bottom panel shows the side view.

By tuning the charge carrier density, experiments reveal a variety of phases, including the already mentioned insulating and superconducting states, as well as correlated metallic and magnetic phases. Several competing ground-state candidates have been proposed, all close in energy. These include the Kramers intervalley-coherent state, the valley-polarized state, and incommensurate Kekulé spiral states. This near-degeneracy suggests that the true ground state is sample-dependent and influenced by strain [136,170,183] and relaxation effects. Contributing factors include also alignment with the hBN substrate [2, 184–196] and twist-angle disorder [80, 167].

Significant effort has been devoted to modelling these structures at the atomistic level—a computationally intensive task, as smaller twist angles lead to larger supercells that must be periodically repeated. Some density functional theory (DFT) studies have successfully tackled the exact MATBG structure [197]. However, due to the high computational cost, several approximate methods have been developed. These include studies focusing on larger twist angles or untwisted structures in various stacking configurations, with the results interpolated to the magic angle regime [198]. Another widely used approach involves tight-binding models, which are considerably less demanding computationally [198–202]. By assuming that electrons are tightly bound to atoms, these models maintain atomistic resolution while offering a practical balance between accuracy and efficiency.

In parallel, a range of continuum models has been developed, many of which have proven remarkably accurate despite relying on idealized assumptions. The most prominent is the Bistritzer-MacDonald model [7, 80, 88, 92–97, 102, 103, 130, 132, 134–137], which treats the system as two separate graphene layers with interlayer hopping. This simplification efficiently captures the low-energy spectrum of MATBG. However, to account for finer spectral features, such as electron–hole asymmetry, additional corrections and more refined theories are required. Other modeling strategies include Hubbard-like lattice models [83, 84, 89, 99, 105–107, 109, 110, 112, 114, 118, 119, 127, 164, 203], as well as heavy fermion approaches [151, 204, 205].

Recently, a considerable effort has been put into studying the electronic properties of MATBG in a magnetic field. The intriguing aspect lies here in the comparable MATBG moiré and magnetic length scales for experimentally accessible magnetic fields. Focusing on the insulating states, a rich phase diagram in the magnetic flux versus the filling factor has been observed [2, 73, 78–81, 85–88, 90, 181, 182, 184, 206–219] in magnetotransport and local electronic compressibility measurements. Streda's formula can be used to determine their topological properties [211, 220]. However, if the observed insulating states are topologically trivial (have zero Chern number), they might originate, e.g., from a combination of two states with opposite Chern numbers. This can especially occur if there is no energy gap between the flat conduction and the flat valence bands. This energy gap can be opened by breaking the inversion and time reversal symmetry at a single particle level, which in practice is done by aligning the MATBG sample with hBN [2, 73, 210, 211].

For magnetic fields around 27 Tesla, the entire flux quantum per moiré unit cell is already achieved [27], and physics related to Hofstadter's fractal structure of the electronic gaps can be observed. Numerous aspects have already been elucidated through the effective models [27, 95, 183, 205, 221–240]. Initial studies concentrated on the general accessibility of the Hofstadter physics with experimentally available magnetic fields [27, 200, 241]. The

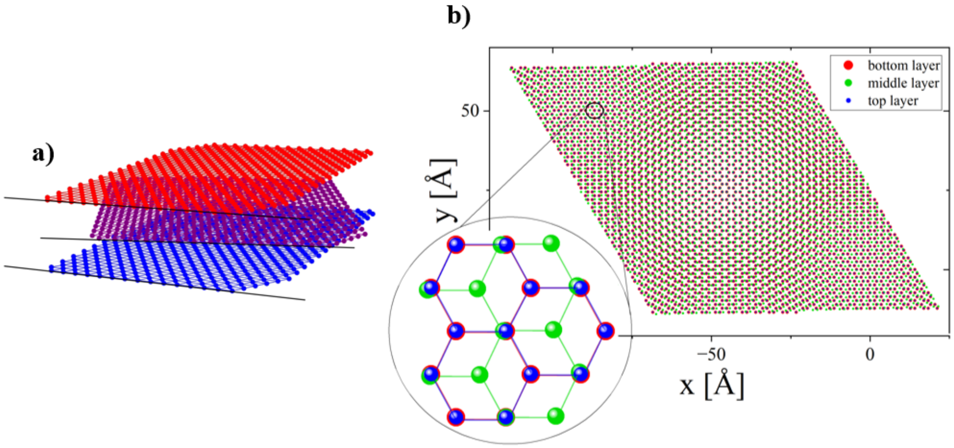

Figure 1.4: Mirror-symmetric TTG: (a) side view of the structure, (b) top view of a moiré UC for the magic angle $\theta = 1.54°$. The inset shows the arrangement of the layers in AB stacking, where the top and bottom layers are aligned (blue and red dots, respectively) and the middle layer is twisted (green dots).

topological aspects of the flat band Landau levels (LLs) have been analyzed [95,97,128,201, 223–225,230,232,239] and the Hofstadter butterfly in the chiral limit has been studied in Refs. [227,231]. The physics of flat bands in strong magnetic fields and possible re-entrant superconductivity have been addressed [234,235,239,240,242].

Magic angle twisted trilayer graphene

Mirror-symmetric magic-angle twisted trilayer graphene (TTG) is often regarded as the closest relative of MATBG. It consists of a middle graphene layer twisted by the magic angle relative to two aligned outer layers [243], see Fig 1.4. Like MATBG, TTG hosts two flat bands (per spin and valley) near the Fermi level. However, its band structure is distinguished by additional Dirac cones intersecting the gap at the K points [138,243–250], a feature also confirmed by ARPES measurements [251].

The electronic spectrum of TTG is highly tunable by several external parameters. As in MATBG, hBN alignment and the twist angle play a crucial role. However, TTG introduces an additional control knob: a perpendicular electric field that can be used to significantly renormalize the band structure. TTG provides a more stable and versatile platform for engineering correlated electronic phases than TBG. Remarkably, TTG exhibits robust and reproducible superconductivity across a broad range of tuning parameters [61, 62, 78, 212, 252–260].

As a result, TTG has become the subject of intense theoretical investigation, encompassing both continuum models [243, 245–248, 250] and atomistic approaches, including *ab initio* [244, 261] and tight-binding methods [261]. The effects of electron interactions have been explored in Refs. [247, 249, 262], while several theoretical proposals address the nature of superconductivity in TTG [261, 263–265]. Phonon-related properties have also been investigated [266].

Despite this progress, a comprehensive theoretical framework for TTG remains elusive. Many of its fundamental properties—such as the detailed magnetic and topological phase diagrams—are still not fully understood.

Rombohedral stacked graphene

The rhombohedrally stacked multilayer graphene family is another class of materials that hosts flat bands. In these systems, a pair of nearly flat bands touch at zero energy, giving rise to correlated electron phenomena that can be further tuned by an external electric field. As the number of layers increases, the bands become progressively flatter, reaching an effective limit around seven graphene layers. Unlike twisted systems, these structures consist of ABC-stacked graphene sheets with no twist angle, resulting in a much smaller unit cell. However, when encapsulated in hBN, a moiré pattern still forms between the outer graphene layer and the aligned substrate. A key advantage of these systems is their simpler fabrication process, as they do not require precise control of a twist angle.

Rhombohedral multilayer graphene has proven to be a fertile ground for strongly correlated electronic phases. Recent experiments have observed correlated insulating states, superconductivity, and magnetism in ABC-stacked trilayer graphene aligned with hBN

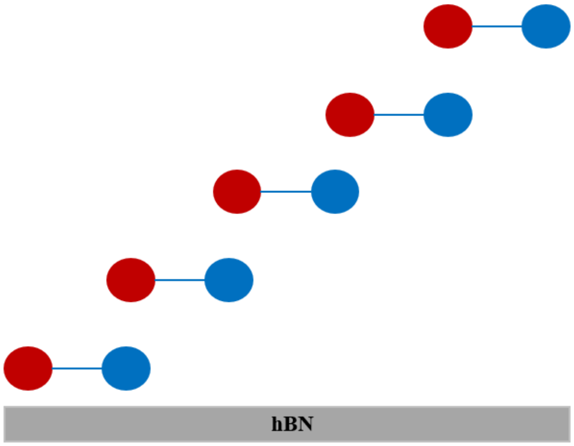

Figure 1.5: Rhombohedral stacked pentalayer graphene: side view. The red dots denote A atoms, blue dots denote B atoms. The sample is positioned on top of an hBN substrate.

[72, 267, 268]. Soon after, a wide range of correlated and topological phenomena were also reported in ABC-stacked tetralayer and pentalayer graphene [269–272].

In the case of rombohedral stacked pentalayer graphene, the presence of a moiré pattern leads to the system exhibiting fractional quantum anomalous Hall effect (FQAHE), which has so far only been observed experimentally in twisted $MoTe_2$. FQAHE is a phenomenon that, like the fractional quantum Hall effect, leads to the fractional quantization of the Hall conductance. However, it does not need strong magnetic fields to occur - in principle, it can be observed at zero magnetic field. This discovery confirmed interest in the rhombohedral group of materials and sparked intensive research into understanding the exact role of the moiré potential.

Twisted TMDs

Shortly after the isolation of monolayer graphene, another class of van der Waals materials drew considerable attention: the TMDs [5]. These materials can exhibit metallic, insulating, or semiconducting behaviour, with the semiconducting members—such as MoS_2,

WS_2, MoSe_2, and WSe_2—being particularly relevant for optoelectronic applications [273]. A widely studied subgroup of TMDs follows the chemical formula MX_2, where M denotes a transition metal (e.g., Mo or W), and X is a chalcogen atom (S, Se, or Te). In contrast to graphene's single-atom thickness, TMD monolayers comprise three atomic planes: a layer of transition metal atoms sandwiched between two chalcogen layers. These materials can adopt several crystal structures, with the most common polymorphs being trigonal (1T), hexagonal (2H), and rhombohedral (3R) [274].

A notable feature of semiconducting TMDs is the transition from an indirect band gap in the bulk to a direct band gap in the monolayer limit, accompanied by strong excitonic effects due to reduced dielectric screening in two dimensions [275]. The electronic structure is largely governed by the localized d orbitals of the transition metal atoms [276–278], which, together with weak screening, enhance electron correlation effects and result in the formation of tightly bound excitons [279–282]. Furthermore, strong spin-orbit coupling in these materials lifts the spin degeneracy in the valence band at the K and –K points in the BZ, giving rise to spin-valley locking—a phenomenon particularly pronounced in tungsten-based compounds such as WSe_2, where the spin-orbit splitting reaches 500 meV [283,284].

Twisted TMD bilayers present a richer playground for correlated and topological phenomena, due to their stronger spin-orbit coupling, multiorbital character, and greater flexibility in stacking configurations. Moiré superlattices can be formed either by twisting two identical monolayers, stacking two different TMDs, or exploiting the natural lattice mismatch between layers, even without a twist. The resulting moiré potentials can give rise to isolated flat bands, enhanced correlation effects, and complex phase diagrams, including Mott-like insulators, generalized Wigner crystals, and interlayer exciton condensation. One of the most striking experimental breakthroughs in this field was the observation of the FQAHE in twisted bilayer MoTe_2—a topological state long predicted but only recently realized [285].

1.2 Quantum information processing

Recent advances in quantum information processing (QIP) have highlighted the promise of engineered 2D materials as versatile platforms for realizing synthetic quantum matter with topological properties. Twisted and nanostructured systems, particularly those based on graphene and related van der Waals materials, offer unprecedented control over electronic correlations, symmetry breaking, and quantum coherence. For example, gate-defined Josephson junctions in MATBG [286], and electrically switchable bistable moiré superconductors [287], demonstrate robust and tunable superconducting states, crucial for scalable quantum circuitry. Similarly, highly tunable junctions and non-local Josephson effects in MATBG tunnelling devices [288] open avenues for topological qubits and quantum interference control.

Further, recent implementations of Hubbard simulators using moiré superlattices provide a platform for emulating strongly correlated lattice models relevant to quantum many-body physics and quantum simulations. On-chip multi-degree-of-freedom control of 2D materials [289] and the development of a quantum twisting microscope [290] enable real-time, local manipulation of interlayer twist angles and strain fields—essential tools for dynamically reconfigurable quantum states and designer Hamiltonians.

These advances illustrate how synthetic topological states in nanostructured 2D systems can be not only observed but also controlled with high precision, supporting the development of programmable, error-resilient quantum devices based on quantum materials engineering.

1.3 Thesis contributions

The contents of this thesis are based on research published in peer-reviewed journals, manuscripts currently under peer review, as well as unpublished research conducted during my PhD degree. A list of manuscripts related to this thesis is:

1. **A. Wania Rodrigues**, M. Bieniek, D. Miravet and P. Hawrylak, *Magnetism and*

hidden quantum geometry in charge neutral twisted trilayer graphene, under review in Nature Communications (2025).

2. **A. Wania Rodrigues**, M. Bieniek, P. Potasz, D. Miravet, R. Thomale, M. Korkusiński, and P. Hawrylak, *Atomistic theory of the moiré Hofstadter butterfly in magic-angle graphene*, Phys. Rev. B 109, 7 (2024).
3. **A. Wania Rodrigues**, D. Miravet and P. Hawrylak, *Absorption spectrum in triangular graphene quantum dots with armchair edges*, in preparation.
4. **A. Wania Rodrigues**, D. Miravet, J. Lawrence and P. Hawrylak, *Probing the zero energy shell wave functions of triangular graphene quantum dots with broken sublattice symmetry using a localized impurity*, Solid State Communications, 41, 115899, (2025).
5. J. Lawrence, Y. He, H. Wei, J. Su, S. Song, **A. Wania Rodrigues**, D. Miravet, P. Hawrylak, J. Zhao, J. Wu, J. Lu, Jiong, *Topological Design and Synthesis of High-Spin Aza-triangulenes without Jahn–Teller Distortions*, ACS Nano, 17(20), (2023).
6. D. Miravet, A. Altıntaş, **A. Wania Rodrigues**, M. Bieniek, M. Korkusiński, and P. Hawrylak, *Interacting holes in gated* $\mathrm{WSe_2}$ *quantum dots*, Phys. Rev. B, 108, 19, (2023).

I have conducted all the calculations mentioned in articles 1-2, 4 in collaboration with the coauthors listed. In article 3, I have conducted the DFT calculation. In article 5, I have reproduced and confirmed the results using DFT. In article 6, I have conducted the CI calculations in collaboration with Daniel Miravet. The tools are in place to reproduce the results if needed.

1.4 Thesis outline

This thesis is organized as follows: the opening section (Chapter 1) introduces the materials under consideration and presents a broader overview of the field and the current state of knowledge. In Chapter 2, we describe various theoretical methods which are later used to study relevant 2D nanostructures.

In Chapters 3-4, we focus on twisted graphene multilayers. In Chapter 3, we start by considering a nanoribbon geometry of MATBG and the effects of the magnetic field. We focus on the topological properties, calculating Chern numbers for this structure. We also obtain the Wannier diagrams and compare them with experimental findings, and finally study the edge and bulk features. We then move on to study the interaction effects in MATBG at different fillings. In Chapter 4, we study the magnetic properties of mirror-symmetric twisted TTG and its hidden quantum geometry.

In Chapter 5, we turn to study TGQDs. We first carry out analytical analysis for TGQDs with a nitrogen impurity, and then compare the results with *ab initio*, numerical tight-binding calculations and with experiment. We also analyze the many-body spectrum of TGQDs using a combination of DFT and Configuration Interaction (CI). Finally, we study a bilayer TGQD with a relative twist between layers and check how the size of the dot and the twist angle influence the degenerate electronic shell present in the energy spectrum of the system.

Chapter 6 includes conclusions of the above work and perspectives for future projects.

Chapter 2

Electronic properties of 2D materials

This chapter gives an overview of the theoretical methods used to study the electronic properties of 2D materials. We start by defining the geometry of twisted graphene multilayers, to which we apply the methods described later. We then describe the general many-body problem and focus on different approximations used to solve it. We derive the tight-binding model and show how it can be applied to moiré materials and compare it with the continuous approach. Later, we focus on the mean-field methods, namely DFT and Hartree-Fock. In the last section, we introduce methods used to study electron correlations and discuss their applicability to specific systems. Finally, we describe the CI method, a combination of DFT and CI, and tensor networks.

2.1 Geometry of twisted multilayer graphene

Here we focus on MATBG and mirror-symmetric magic angle TTG. Given their structural similarities, we begin by describing the construction of TBG and then outline the modifications required to extend the analysis to TTG.

Graphene is composed of carbon atoms arranged on a honeycomb lattice, with two atoms, A and B, inside a unit cell. The primitive lattice vectors are given by $\vec{a}_1 = (0, \sqrt{3}a)$

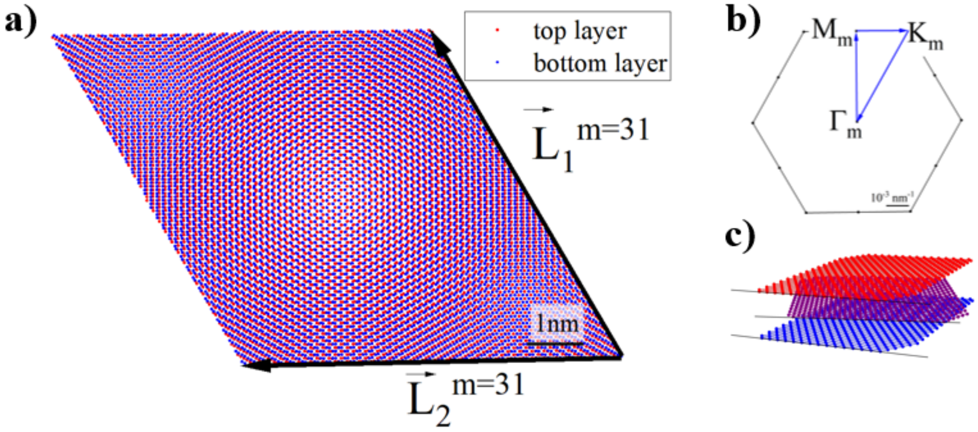

Figure 2.1: Structural properties of moiré lattice. (a) Moiré unit cell for MATBG consisting of 11908 atoms, spanned by the superlattice vectors $\vec{L}_1$ and $\vec{L}_2$. (b) Moiré BZ defined by the reciprocal lattice vectors $\vec{G}_1$ and $\vec{G}_2$ with high symmetry points marked. (c) Side view of TTG.

and $\vec{a}_2 = \frac{a}{2}(3, -\sqrt{3})$, where $a = 1.412$ Å is the carbon–carbon bond length. This lattice structure is illustrated in Fig. 1.1(a).

Twisted bilayer graphene

TBG is defined as two graphene sheets in e.g. Bernal stacking [291], rotated by an angle θ around the (0,0) point. This angle θ in principle can be arbitrary, but not every θ will lead to a moiré periodicity arising in the system. For that to occur, θ has to belong to a set of commensurate angles. Only then, the periodicities of the two overlapping lattices will coincide and a moiré supercell can be defined. When θ is incommensurate the lattice forms a quasicrystal instead. In the commensurate case, if we rotate the two layers by a point (A_1, B_2), at which atom B in the lower layer is directly above atom A in the top layer, such stacking will occur elsewhere in the structure, at a distance $\vec{L}_M$. In order to obtain the A_1B_2 stacking, a B_2 site must rotate to an A_1 site. Vectors L_{Mi} (see Fig. 2.2)

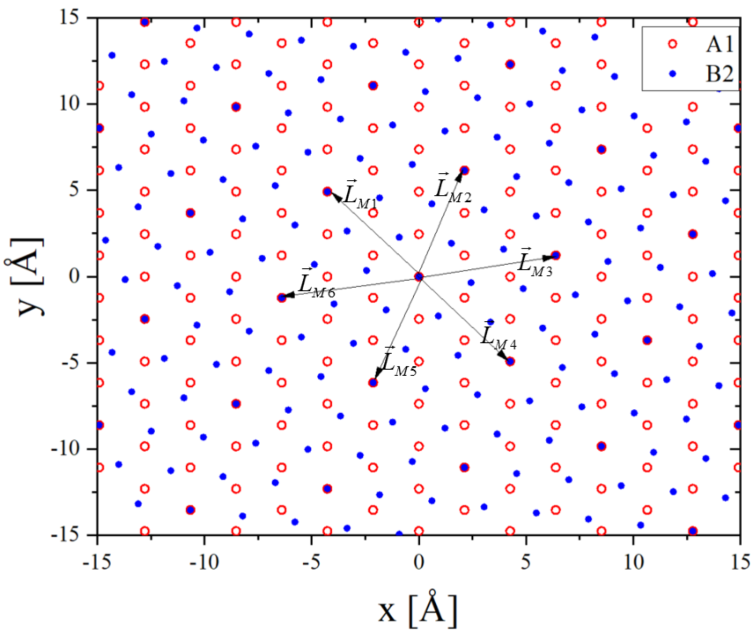

Figure 2.2: Moiré lattice of A_1 and B_2 atoms. The arrows mark vectors connecting the same stacking configurations

connecting these two stackings with the origin have to have the same length:

$$k\vec{a_1} + l\vec{a_2} \rightarrow m\vec{a_1} + n\vec{a_2} \quad k, l, m, n \in \mathbb{Z}, \tag{2.1}$$

meaning

$$|k\vec{a_1} + l\vec{a_2}|^2 = |m\vec{a_1} + n\vec{a_2}|^2, \tag{2.2}$$

which gives us a condition:

$$k^2 + l^2 - kl = n^2 + m^2 - mn. \tag{2.3}$$

This is a Diophantine equation, solving which leads to a lengthy calculation and is described in detail in Ref. [292]. Alternatively, one can consider the point symmetries of the hexagonal lattice and follow the arguments presented in Ref. [293]. Both approaches lead to an expression of a twist angle that results in a commensurate structure [91]:

$$\cos(\theta_m) = \frac{3m^2 + 3m + 1/2}{3m^2 + 3m + 1}, \tag{2.4}$$

where m is an integer. Here, the larger the m, the smaller the θ_m. We focus on the magic angle $m = 31$, which corresponds to $\theta = 1.05°$. The number of atoms within a moiré unit cell can be calculated through the relation $N_{\text{at}} = 4(m^2 + (m+1)^2 + m(m+1))$, which, for the magic angle, yields $N_{\text{at}} = 11908$ atoms.

Using the law of cosines, one can then obtain the linearly independent moiré primitive vectors:

$$\begin{aligned} \vec{L}_1^{(m)} &= m\vec{a}_1 - (m+1)\vec{a}_2, \\ \vec{L}_2^{(m)} &= -(m+1)\vec{a}_1 - (2m+1)\vec{a}_2. \end{aligned} \tag{2.5}$$

See Fig. 2.1(a).

Using the superlattice vectors $\vec{L}_1$ and $\vec{L}_2$, we determine the corresponding reciprocal space primitive vectors $\vec{G}_1$ and $\vec{G}_2$, which are used to construct a moiré Brillouin zone (BZ). Using the definition $\vec{G}_i \cdot \vec{L}_j = 2\pi \cdot \delta_{ij}$ we derive $\vec{G}_1$ and $\vec{G}_2$ in the form:

$$\begin{aligned} \vec{G}_1 &= \frac{2\pi}{3a}\frac{1}{3m^2 + 3m + 1}\left[-1, \sqrt{3}(2m+1)\right], \\ \vec{G}_2 &= \frac{2\pi}{3a}\frac{1}{3m^2 + 3m + 1}\left[-3m + 1, \sqrt{3}(m+1)\right]. \end{aligned} \tag{2.6}$$

After obtaining $\vec{G}_1$ and $\vec{G}_2$, we proceed to construct a moiré BZ, in which high symmetry points Γ_m, K_m, M_m can be identified, as illustrated in Fig. 2.1 (b). The size of the moiré BZ depends on the integer m - the larger the m, the smaller the twist angle and the smaller the BZ.

The distance between the two graphene layers depends on the relative stacking and is nonuniform in the moiré unit cell. We account for the lattice relaxation effects along the z-axis by varying the inter-layer distance based on the stacking configuration. The layers are closest to each other in the AB stacked regions where $z_{\text{AB}} = z_{\text{min}} = 3.34$ Å. The

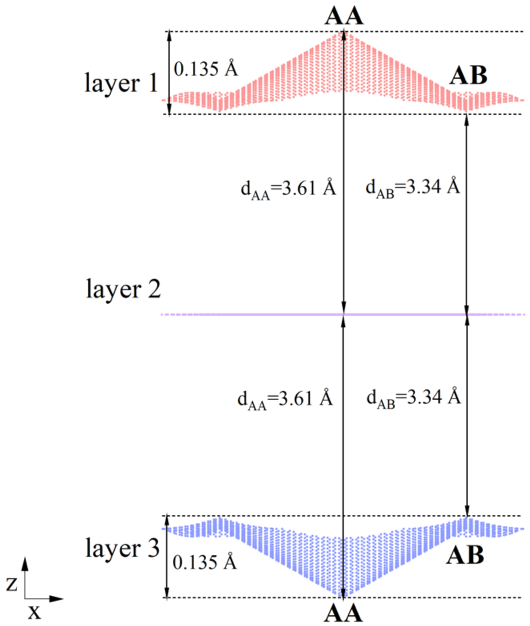

Figure 2.3: TTG relaxation details: side view of the structure with the widths of layers and gaps marked by black arrows. Stacking configurations are indicated.

largest distance arises in AA stackings, for which we adopt $z_{\mathrm{AA}} = z_{\max} = 3.61$ Å [294]. To determine the relaxed interlayer distance z_{relax}, we introduce a stacking parameter δz assigned to each atom. This parameter depends on the distance in the xy plane between the considered atom and its nearest neighbour of a different type in the other layer. Specifically, it is defined as $\delta z = a^{-1}\sqrt{(x_1 - x_2)^2 + (y_1 - y_2)^2}$, where x_1 and y_1 describe the position of the considered atom, and x_2 and y_2 refer to its nearest neighbour in the other layer. The factor a^{-1} is included, so that $\delta z = 0$ in the AA stacking and $\delta z = 1$ for the AB stacking. The relaxed inter-layer distance is then calculated as $z_{\mathrm{relaxed}} = z_{\max} - \delta z(z_{\max} - z_{\min})$.

Twisted trilayer graphene

Mirror-symmetric TTG is constructed by aligning the top and bottom layers and twisting the middle layer by a given angle θ, see Fig. 2.1(c). We can treat it, therefore, as a

TBG and an extra, aligned graphene layer. The construction of the moiré vectors and the moiré unit cell is analogous to the TBG case. The magic angle is, however, slightly larger and equal to $\theta = 1.55^\circ$ ($m = 21$). The number of atoms in moiré unit cell is now $N_{\mathrm{at}} = 6(3m(m+1)+1)$, which here gives 8322 atoms. The construction of the moiré BZ is analogous to that in the TBG case.

The relaxation mechanism is also very similar to TBG, since we account for the relaxation effects along the z-axis by varying the inter-layer distance based on the stacking configuration [244, 261, 295]. We treat the middle layer as rigid and relax only the top and bottom layers. All the parameters are equal to those chosen for TBG. For details, see Fig. 2.3.

2.2 Formulation of the many-body problem

Theoretical methods used to study 2D materials can generally be divided into two main approaches: atomistic and continuum. There are also methods that combine the two, such as $k \cdot p$ + DFT or effective models for Wannier orbitals of moiré centers. Atomistic methods model materials at the scale of individual atoms and include techniques such as DFT and tight-binding models. These approaches provide detailed insight into electronic structure, atomic relaxation, and interlayer interactions. By capturing the full lattice geometry, they enable a realistic treatment of strain, defects, and local symmetry breaking—essential for understanding the complex behaviour of twisted and stacked 2D materials. Their main limitation, however, is computational cost. Realistic samples often contain millions of atoms, resulting in Hamiltonians of that dimension, making direct diagonalization highly demanding. These calculations require significant optimization and high-performance computing resources to be feasible.

Continuum models, by contrast, are far more computationally efficient. Instead of resolving individual atoms, they treat the system using effective bands that capture the relevant low-energy physics. Approaches like the Bistritzer-MacDonald model reproduce the low-energy electronic and topological features of such systems.

However, since they use strong approximations, they often fail to capture finer atomistic features, such as particle–hole asymmetry, valley coupling, strain or edge states, which are naturally present in atomistic descriptions. What is more, atomistic approaches are better suited for studies of systems in a magnetic field, since they are not limited by the magnetic UC and allow for an arbitrary magnetic field to be applied. Given our focus on achieving a realistic and microscopically resolved picture of the system, we primarily rely on atomistic methods in this work. In the case of twisted graphene multilayers, we use tight-binding techniques, which offer a good trade-off between accuracy and computation time. In the case of graphene quantum dots, we will also use *ab initio* methods, which are well suited for small nanostructures.

We start our analysis by defining the many-body problem. Let us consider a system of N electrons in a potential of M ionic positive charges:

$$H = \sum_{i}^{N} \left[\frac{\vec{p}_i^2}{2m} + V_{ext}(\vec{r}_i) \right] + \sum_{i<j} \frac{e^2}{|\vec{r}_i - \vec{r}_j|}, \tag{2.7}$$

Here, the first term corresponds to the kinetic energy of electrons with momentum $\vec{p}_i$ and mass m. The second term, $V_{ext}(\vec{r}_i) = -\sum_{\alpha=1}^{M} \frac{Z_\alpha e^2}{|\vec{r}_i - \vec{R}_\alpha|}$, is the Coulomb interaction between electrons and ions, with $\vec{r}_i$ being the electron position, $\vec{R}_\alpha$ the ion position, Z the atomic number and e the electron charge. The last term is the Coulomb interaction between pairs of electrons. In order to write our Hamiltonian in the second quantization, we define the field operators. First, we identify a one body Hamilitonian term H_0 and a two body interaction term V_{ee}:

$$\hat{H} = \underbrace{\frac{\hat{p}^2}{2m} + \hat{V}_{ext}(\vec{r})}_{H_0(\vec{r})} + \hat{V}_{ee}. \tag{2.8}$$

We will focus on the single particle part first:

$$\hat{H}_0 = \int \hat{\Psi}^\dagger(\vec{r}) H_0(\vec{r}) \hat{\Psi}(\vec{r}) d\vec{r} \tag{2.9}$$

The field operators $\hat{\Psi}(\vec{r})$ are written in terms of Wannier orbitals:

$$\hat{\Psi}(\vec{r}) = \sum_i \phi_z(\vec{r} - \vec{R}_i)\hat{c}_i. \tag{2.10}$$

The creation (annihilation) operator $\hat{c}_i^\dagger$ ($\hat{c}_i$) creates (annihilates) an electron at the orbital p_z on an atom i. We insert this expression into Eq. 2.9 to obtain the Hamiltonian in the second quantization using the basis of orthonormal states $\{\phi_z\}$ that are the eigenstates of the Hamiltonian $H_0(\vec{r})$, satisfying the Schrödinger equation:

$$\left(\frac{\vec{p}_i}{2m} + V_{ext}(\vec{r} - \vec{R}_i)\right)\phi_z(\vec{r} - \vec{R}_i) = \mathcal{E}_i\phi_z(\vec{r} - \vec{R}_i) \tag{2.11}$$

$$\hat{H}_0 = \sum_{i,j} \hat{c}_i^\dagger \hat{c}_j \int \phi_z^*(\vec{r} - \vec{R}_i) H_0(\vec{r}) \phi_z(\vec{r} - \vec{R}_j) d\vec{r} \tag{2.12}$$

and use the explicit form of $H_0(\vec{r})$:

$$H_0(\vec{r}) = \frac{\hat{p}^2}{2m} + \sum_l \hat{V}_{ion}(\vec{r} - \vec{R}_l), \tag{2.13}$$

which gives us:

$$\hat{H}_0 = \sum_{i,j} c_i^\dagger c_j \int \phi_z^*(\vec{r} - \vec{R}_i)\left[\frac{\hat{p}^2}{2m} + \sum_l \hat{V}_{ion}(\vec{r} - \vec{R}_l)\right]\phi_z(\vec{r} - \vec{R}_j) d\vec{r} \tag{2.14}$$

If we focus on the effect of the Hamiltonian on site j, we can divide the sum over l into two terms - the onsite contribution and all others:

$$\begin{aligned}
H &= \sum_{i,j} c_i^\dagger c_j \int \phi_z^*(\vec{r}-\vec{R}_i)\left[\frac{\hat{p}^2}{2m} + \hat{V}_{ion}(\vec{r}-\vec{R}_j) + \sum_{l\neq j}\hat{V}_{ion}(\vec{r}-\vec{R}_l)\right]\phi_z(\vec{r}-\vec{R}_j)d\vec{r} \\
&= \sum_{i,j} c_i^\dagger c_j \underbrace{\int \phi_z^*(\vec{r}-\vec{R}_i)\left[\frac{\hat{p}^2}{2m} + \hat{V}_{ion}(\vec{r}-\vec{R}_j)\right]\phi_z(\vec{r}-\vec{R}_j)d\vec{r}}_{\mathcal{E}_j\delta_{ij}} \\
&+ \sum_{i,j} c_i^\dagger c_j \underbrace{\int \phi_z^*(\vec{r}-\vec{R}_i)\left[\sum_{l\neq j}\hat{V}_{ion}(\vec{r}-\vec{R}_l)\right]\phi_z(\vec{r}-\vec{R}_j)d\vec{r}}_{t_{ij}}.
\end{aligned} \tag{2.15}$$

Where in the second line, we use the fact that the orbitals ϕ_z are eigenstates of $H_0(\vec{r})$, see Eq. 2.11:

$$\hat{H}_0 = \sum_i \mathcal{E}_i c_i^\dagger c_i + \sum_{\substack{i,j,\sigma \\ i\neq j}} t_{ij} c_i^\dagger c_j \tag{2.16}$$

Now we can analogously treat the interaction part $\hat{V}_{ee}$:

$$\hat{V}_{ee} = \frac{1}{2}\int\int dr dr' \Psi^+(r)\Psi^+(r')V(\vec{r}-\vec{r'})\Psi(r')\Psi(r) \tag{2.17}$$

Here:

$$V(\vec{r}-\vec{r'}) = \frac{e^2}{|\vec{r}-\vec{r'}|} \tag{2.18}$$

Again, we use the orthonormal basis ϕ_i to write $\hat{V}_{ee}$ in terms of creation and annihilation operators:

$$\hat{V}_{ee} = \frac{1}{2}\sum_{ijkl} c_i^\dagger c_j^\dagger c_k c_l \underbrace{\int\int \phi_z(\vec{r}-\vec{R}_i)\phi_z(\vec{r'}-\vec{R}_j)V(\vec{r}-\vec{r'})\phi_z(\vec{r'}-\vec{R}_k)\phi_z(\vec{r}-\vec{R}_l)d\vec{r}d\vec{r'}}_{V_{ijkl}} \tag{2.19}$$

This way we get the full many-body Hamiltonian in the second quantization form:

$$H = \sum_{i} \mathcal{E}_i c_i^\dagger c_i + \sum_{\substack{i,j,\sigma \\ i \neq j}} t_{ij} c_i^\dagger c_j + \frac{1}{2} \sum_{ijkl} V_{ijkl} c_i^\dagger c_j^\dagger c_k c_l \tag{2.20}$$

Here we are considering graphene with only one type of orbital, and since the Hamiltonian conserves the number of electrons and we will always work in situations with a fixed number of particles, therefore the $\mathcal{E}_i$ onsite term will be constant and can be neglected at this point. In this work, we will approximate the Wannier orbitals by p_z orbitals centered at atomic positions. We will also consider a sum over all i and j, assuming that when $i = j$, $t = 0$. We will now focus on the simplified form of this Hamiltonian and its single-particle properties.

2.3 Single electron physics

2.3.1 Tight-binding method for twisted graphene multilayers

We focus now on the single particle physics, and will consider the electron-electron interactions later. Our Hamiltonian simplifies then to:

$$H = \sum_{i,j} t_{ij} c_i^\dagger c_j. \tag{2.21}$$

For convenience, we will now start to make a distinction between sublattices, and enumerate them with an α index, splitting the sum over all atoms, into a sum over UC and sublattices:

$$H = \sum_{i,j}^{N_{UC}} \sum_{\alpha\beta}^{N_{at}} t_{ij}^{\alpha\beta} c_{i\alpha}^\dagger c_{j\beta}. \tag{2.22}$$

This Hamiltonian is an *ab initio*-based tight-binding model for p_z atomic orbitals [198,199] and tunnelling over all the atoms in the sample. $N = N_{\text{UC}} \cdot N_{\text{at}}$ represents the total number of atoms, equal to the number of UCs N_{UC} multiplied by the number of atoms in the unit cell N_{at}, while $c_{i\alpha}^{\dagger}$ ($c_{i\alpha}$) is the creation (annihilation) operator for a particle on the p_z orbital centered on atom in UC i, on sublattice α. The hopping parameter is defined as [198]:

$$t_{ij}^{\alpha\beta} = (1-n^2)\gamma_0 \exp\left(\lambda_1\left(1-\frac{|\vec{r}_i+\vec{\tau}_\alpha-\vec{r}_j-\vec{\tau}_\beta|}{a}\right)\right) + n^2\gamma_1 \exp\left(\lambda_2\left(1-\frac{|\vec{r}_i+\vec{\tau}_\alpha-\vec{r}_j-\vec{\tau}_\beta|}{c}\right)\right), \tag{2.23}$$

where $a = 1.412$ Å is the carbon-carbon distance, and $c = 3.36$ Å is a non-relaxed interlayer distance. The direction cosine along the z-axis is denoted by n. Intra-layer hopping is parametrized by $\gamma_0 = -2.835$ eV, while inter-layer hopping is by $\gamma_1 = 0.48$ eV. The dimensionless decay constants are $\lambda_1 = 3.15$ and $\lambda_2 = 7.50$. These parameters were obtained in Ref. [198] by fitting to the *ab initio* results of unrotated graphene bilayers in different stacking configurations, as well as bilayers rotated by larger twist angles. A general solution for all twist angles has been interpolated from these calculations. These parameters are known to reproduce well the *ab initio* band structure of MATBG [197,199], as well as the *ab initio* Dirac cone velocity renormalization for arbitrary twist angles [198]. We opt for $\gamma_0 = -2.835$ eV value to match our band structure as well as possible to state-of-the-art *ab initio* MATBG band structure in Ref. [197], focusing on the flat band width, remote gap values, and the electron-hole asymmetry in the flat band. Such parametrization works equally well for the case of trilayer graphene.

For our calculations, we consider interactions of atoms within a distance $\leq 6a$ from the considered atom. Including additional neighbours does not cause significant quantitative changes in our results. For example, if cutoff radius is set to $r_{cutoff} = 7a$, maximal flat band energy difference is 0.002 meV around Γ point in the top conduction band of the flat band. However, for a smaller hopping radius (e.g. $r_{cutoff} = 4a$), the band structure difference becomes visible, e.g. of the order of 0.5 meV around the Γ point for the flat band conduction band.

To account for the presence of an hBN substrate, we introduce a staggered potential Δ_{hBN} to the bottom layer of our system (in the bilayer case), or to the top and bottom layers (trilayer case). We can therefore define:

$$\hat{H}_{\Delta_{\text{hBN}}} = \Delta_{\text{hBN}} \sum_i \sum_\alpha \tau_i^\alpha |l_i^\alpha| c_{i\alpha}^\dagger c_{i\alpha} \tag{2.24}$$

where $l_i^\alpha = 1, 0, -1$ for top, middle and bottom layers respectively for TTG and 1, 0 for bottom and top layers for TBG. $\tau_i^\alpha = 1, -1$ when α belongs to sublattice A and B, respectively, in both cases. This way, there is a $2\Delta_{\text{hBN}}$ difference in onsite energy between A and B atoms of the top and bottom layers for trilayers. Furthermore, a perpendicular electric field is introduced in the TTG case, modifying the potential difference between the top and bottom layers:

$$\hat{H}_{\Delta_V} = \frac{\Delta_V}{2} \sum_i \sum_\alpha l_i^\alpha c_{i\alpha}^\dagger c_{i\alpha}. \tag{2.25}$$

We want to diagonalize this Hamiltonian in the reciprocal space. In order to do so, we have to rotate our creation and annihilation operators:

$$\begin{aligned} \hat{c}_{i\alpha}^\dagger &= \frac{1}{\sqrt{N_{UC}}} \sum_k e^{i\vec{k}\cdot(\vec{R}_i+\vec{\tau}_\alpha)} \hat{a}_{k\alpha}^\dagger \\ \hat{c}_{i\alpha} &= \frac{1}{\sqrt{N_{UC}}} \sum_k e^{-i\vec{k}\cdot(\vec{R}_i+\vec{\tau}_\alpha)} \hat{a}_{k\alpha}. \end{aligned} \tag{2.26}$$

Here $\vec{R}_i$ denote the position of a unit cell and $\vec{\tau}_\alpha$ the position of an atom within the unit cell, i.e. the sublattice. In the following derivation, we will not consider terms 2.25 and 2.24 separately, since they will behave as $t_{ii}^{\alpha\alpha}$ and their transformation can be adapted from the final result. We can now rewrite our Hamiltonian 2.22 in terms of operators $a_{k\alpha}^\dagger$ and $a_{k\alpha}$:

$$\begin{aligned} H &= \sum_{i,j} \sum_{\alpha\beta} t_{ij}^{\alpha\beta} \frac{1}{\sqrt{N_{UC}}} \sum_k e^{i\vec{k}\cdot(\vec{R}_i+\vec{\tau}_\alpha)} a_{k,\alpha}^\dagger \frac{1}{\sqrt{N_{UC}}} \sum_{k'} e^{-i\vec{k'}\cdot(\vec{R}_j+\vec{\tau}_\beta)} a_{k',\beta} \\ &= \frac{1}{N_{UC}} \sum_{i,j} \sum_{\alpha\beta} t_{ij}^{\alpha\beta} \sum_{k,k'} e^{i\vec{k}\cdot(\vec{R}_i+\vec{\tau}_\alpha)} e^{-i\vec{k'}\cdot(\vec{R}_j+\vec{\tau}_\beta)} a_{k,\alpha}^\dagger a_{k',\beta}. \end{aligned} \tag{2.27}$$

We now introduce a new variable $\vec{r} = \vec{R}_i + \vec{\tau}_\alpha - \vec{R}_j - \vec{\tau}_\beta$:

$$H = \frac{1}{N_{UC}} \sum_i \sum_{\alpha\beta} \sum_{\vec{r}} t(\vec{r}) \sum_{k,k'} e^{i\vec{k}\cdot(\vec{R}_i+\vec{\tau}_\alpha)} e^{-i\vec{k'}\cdot(\vec{R}_i+\vec{\tau}_\alpha-\vec{r})} a^\dagger_{k,\alpha} a_{k',\beta} \tag{2.28}$$

Rearranging the variables, we have:

$$\begin{aligned} H &= \frac{1}{N_{UC}} \sum_i \sum_{\alpha\beta} \sum_{\vec{r}} t(\vec{r}) \sum_{k,k'} e^{i(\vec{k}-\vec{k}')\cdot(\vec{R}_i+\vec{\tau}_\alpha)} e^{-i\vec{k'}\cdot\vec{r}} a^\dagger_{k,\alpha} a_{k',\beta} \\ &= \sum_{\alpha\beta} \sum_{\vec{r}} t(\vec{r}) \sum_{k,k'} e^{-i\vec{k'}\cdot\vec{r}} \underbrace{\sum_i \frac{1}{N_{UC}} e^{i(\vec{k}-\vec{k}')\cdot(\vec{R}_i+\vec{\tau}_\alpha)}}_{\delta_{\vec{k},\vec{k}'}} a^\dagger_{k,\alpha} a_{k',\beta} \\ &= \sum_k \sum_{\alpha\beta} \sum_{\vec{r}} t(\vec{r}) e^{-i\vec{k}\cdot\vec{r}} a^\dagger_{k,\alpha} a_{k,\beta}. \end{aligned} \tag{2.29}$$

When applied to twisted graphene multilayers, the moiré unit cell contains around 10^5 atoms, and because the hopping vanishes quickly with the distance, the sum over $\vec{r}$ reduces to a single non-zero element from either the considered unit cell or its nearest neighbours. Hopping terms $t^{\alpha\beta}_{ij}$ are defined in Eq. 2.23 and depend on the sublattice and unit cell position of the considered atoms. $\vec{k} = (k_x, k_y)$ represents the wave vector within the 1st moiré BZ.

If we consider the case of monolayer graphene in the NN approximation, we can consider two cases:

$$t(\vec{r}) = \begin{cases} t & \text{for } \vec{r} = \pm\vec{b_1}, \pm\vec{b_2}, \pm\vec{b_3} \\ 0 & \text{otherwise} \end{cases} \tag{2.30}$$

where $\vec{b_1}, \vec{b_2}, \vec{b_3}$ are the vectors connecting a given atom to its three NN. Then our expression becomes:

$$H = t \sum_k \sum_{\alpha\beta} \underbrace{\left(e^{-i\vec{k}\cdot\vec{b}_1} + e^{-i\vec{k}\cdot\vec{b}_2} + e^{-i\vec{k}\cdot\vec{b}_3} \right)}_{f(k)} a^\dagger_{k,\alpha} a_{k,\beta}. \tag{2.31}$$

Our Hamiltonian matrix for the graphene case is then:

$$H = \sum_{\vec{k}} (a_{kA}^{\dagger} \quad a_{kB}^{\dagger}) \begin{pmatrix} 0 & f(k) \\ f^{*}(k) & 0 \end{pmatrix} \begin{pmatrix} a_{kA} \\ a_{kB} \end{pmatrix} \tag{2.32}$$

which is the commonly used form.

2.3.2 Continuum model for twisted graphene multilayers

An alternative approach to the atomistic models for graphene multilayers is a continuum description that makes use of the periodicity of the moiré lattice. The most widely used approach is that of the Bistritzer-MacDonald (BM) model [7]. Below we present its derivation.

Geometry of twisted bilayer graphene

We start off by considering two graphene layers in an AB stacking with a relative twist θ between them. We define lattice vectors for layer j as:

$$\begin{aligned} \vec{a}_1^{(j)} &= a_0 R_{\theta/2}^{(j)} \left(-\frac{1}{2}, \frac{\sqrt{3}}{2} \right) \\ \vec{a}_2^{(j)} &= a_0 R_{\theta/2}^{(j)} \left(-\frac{1}{2}, -\frac{\sqrt{3}}{2} \right), \end{aligned} \tag{2.33}$$

where a_0 is the graphene lattice constant ($a_0 = a\sqrt{3}$) and $R_{\theta/2}^{(j)}$ is the rotation matrix for layer j. Each layer consists of two sublattices, whose position is described with the vectors

τ:

$$\begin{aligned}
\vec{\tau}_A^{(1)} &= (0,0) \\
\vec{\tau}_B^{(1)} &= \frac{a_0}{\sqrt{3}} R_{\theta/2}^{(1)}(0,1) \\
\vec{\tau}_A^{(2)} &= -\frac{a_0}{\sqrt{3}} R_{\theta/2}^{(2)}(0,1) \\
\vec{\tau}_B^{(2)} &= (0,0).
\end{aligned} \tag{2.34}$$

The reciprocal lattice vectors for layer j satisfy the relation $\vec{G}_a^{(j)} \cdot \vec{a}_b^{(j)} = 2\pi\delta_{ab}$ and are given by:

$$\begin{aligned}
\vec{G}_1^{(j)} &= \frac{4\pi}{a_0\sqrt{3}} R_{\theta/2}^{(j)} \left(-\frac{\sqrt{3}}{2}, \frac{1}{2}\right) \\
\vec{G}_2^{(j)} &= \frac{4\pi}{a_0\sqrt{3}} R_{\theta/2}^{(j)} \left(-\frac{\sqrt{3}}{2}, -\frac{1}{2}\right).
\end{aligned} \tag{2.35}$$

Moiré periodicty

A twist in real space results in a relative rotation between the BZs of the two graphene layers in reciprocal space. This rotation causes a shift between the Dirac points of the individual layers, from which a new, smaller BZ—the moiré BZ—can be defined (see Fig. 2.4 (a)). While the twist angle between the layers can, in principle, take any value, only a discrete set of angles leads to commensurability between the original graphene lattices and the emergent moiré pattern. At these special angles, known as commensurate twist angles, a new periodicity arises in the system, allowing us to define a moiré superlattice. The corresponding moiré lattice vectors were introduced earlier in Section 2.1.

The BM model contains two single-layer Dirac Hamiltonians describing isolated graphene sheets and a tunnelling term for hopping between them. Single graphene layer Hamiltonian

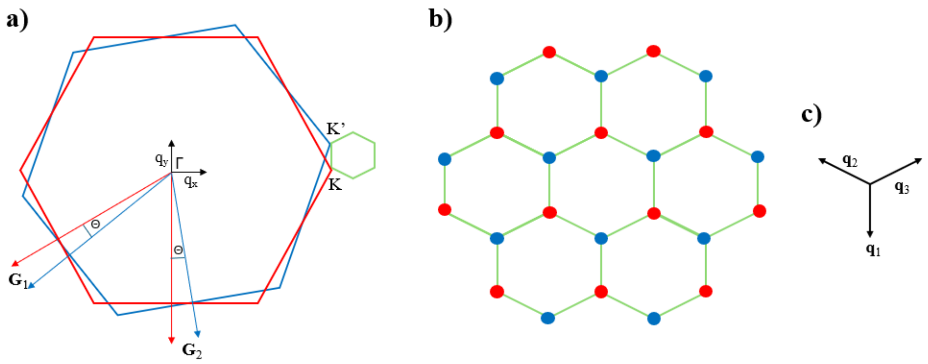

Figure 2.4: Reciprocal space geometry of TBG: (a) Two graphene BZ, in blue and red, twisted with respect to each other by angle θ. The resulting moiré BZ is shown in green. (b) Lattice of moiré BZs. Points originating from the top graphene BZ are marked in red, and the bottom in blue. (c) Vectors $\vec{q_i}$ connecting NN in the moiré reciprocal space.

for valley K has the form:

$$h^K(\vec{k}) = \hbar v_F \vec{\sigma} \cdot \vec{k} = \hbar v_F \begin{pmatrix} 0 & k_x - ik_y \\ k_x + ik_y & 0 \end{pmatrix}, \tag{2.36}$$

and for valley K':

$$h^{K'}(\vec{k}) = \hbar v_F \vec{\sigma^*} \cdot \vec{k} = \hbar v_F \begin{pmatrix} 0 & k_x + ik_y \\ k_x - ik_y & 0 \end{pmatrix} \tag{2.37}$$

where $\vec{k} = (k_x, k_y)$ and $\vec{\sigma}$ is the Pauli matrix.

We focus on the low-energy spectrum, which is governed by electronic states near the Dirac points (K and K') of the graphene BZ. Since the K and K' valleys are separated by a large momentum in reciprocal space, intervalley scattering is suppressed, and the two valleys can be treated as decoupled. We can therefore analyze each valley independently

Interlayer tunneling terms

As mentioned, our Hamiltonian can be divided into two decoupled graphene Hamiltonians, and tunnelling between them. The monolayer wavefunctions have the form:

$$\begin{aligned}
\left|\psi^{(1)}_{\vec{k},\alpha}\right\rangle &= \frac{1}{\sqrt{N}}\sum_{\vec{R}^{(1)}} e^{i\vec{k}\cdot(\vec{R}^{(1)}+\vec{\tau}^{(1)}_{\alpha})}\left|\vec{R}^{(1)}+\vec{\tau}^{(1)}_{\alpha}\right\rangle \\
\left|\psi^{(2)}_{\vec{k},\beta}\right\rangle &= \frac{1}{\sqrt{N}}\sum_{\vec{R}^{(2)}} e^{i\vec{k}\cdot(\vec{R}^{(2)}+\vec{\tau}^{(2)}_{\beta})}\left|\vec{R}^{(2)}+\vec{\tau}^{(2)}_{\beta}\right\rangle ,
\end{aligned} \tag{2.38}$$

for the top and bottom layer, respectively. Then we can write the tunnelling matrix elements as:

$$T^{\alpha\beta}_{kp} = \left\langle\psi^{(1)}_{k\alpha}\right| H_T \left|\psi^{(2)}_{p\beta}\right\rangle = \frac{1}{N}\sum_{\vec{R}^{(1)}}\sum_{\vec{R}^{(2)}} e^{i\vec{p}\cdot(\vec{R}^{(2)}+\vec{\tau}^{(2)}_{\beta})-i\vec{k}\cdot(\vec{R}^{(1)}+\vec{\tau}^{(1)}_{\alpha})}\left\langle\vec{R}^{(1)}+\vec{\tau}^{(1)}_{\alpha}\right| H_T \left|\vec{R}^{(2)}+\vec{\tau}^{(2)}_{\beta}\right\rangle . \tag{2.39}$$

Here:

$$\left\langle\vec{R}^{(1)}+\vec{\tau}^{(1)}_{\alpha}\right| H_T \left|\vec{R}^{(2)}+\vec{\tau}^{(2)}_{\beta}\right\rangle = t\left(\vec{R}^{(1)}+\vec{\tau}^{(1)}_{\alpha}-\vec{R}^{(2)}-\vec{\tau}^{(2)}_{\beta}\right) \sim e^{-\frac{1}{\lambda}\left(|\vec{R}^{(1)}+\vec{\tau}^{(1)}_{\alpha}-\vec{R}^{(2)}-\vec{\tau}^{(2)}_{\beta}|\right)^2} \tag{2.40}$$

The Fourier transform of the $t(\vec{r})$ function has the form:

$$t\left(\vec{R}^{(1)}+\vec{\tau}^{(1)}_{\alpha}-\vec{R}^{(2)}-\vec{\tau}^{(2)}_{\beta}\right) = \frac{1}{N\Omega}\sum_{\vec{k}'}\sum_{\vec{G}'^{(1)}} t_{\vec{k}'+\vec{G}'^{(1)}} e^{i\left(\vec{k}'+\vec{G}'^{(1)}\right)\cdot\left(\vec{R}^{(1)}+\vec{\tau}^{(1)}_{\alpha}-\vec{R}^{(2)}-\vec{\tau}^{(2)}_{\beta}\right)}. \tag{2.41}$$

Here $\vec{k}'$ are the momenta from the original BZ, $\vec{G}'^{(1)}$ are reciprocal vectors of one chosen layer, and Ω is the UC area. Summing over both of these vectors, we make sure to cover the whole reciprocal space. We can now calculate $T^{\alpha\beta}_{kp}$. We insert the Fourier transform 2.41 into the equation 2.39:

$$T^{\alpha\beta}_{kp} = \frac{1}{N^2\Omega}\sum_{\vec{R}^{(1)}}\sum_{\vec{R}^{(2)}}\sum_{\vec{k}'}\sum_{\vec{G}'^{(1)}} t_{\vec{k}'+\vec{G}'^{(1)}} e^{i\left(\vec{k}'+\vec{G}'^{(1)}\right)\cdot\left(\vec{R}^{(1)}+\vec{\tau}^{(1)}_{\alpha}-\vec{R}^{(2)}-\vec{\tau}^{(2)}_{\beta}\right)} e^{i\vec{p}\cdot(\vec{R}^{(2)}+\vec{\tau}^{(2)}_{\beta})-i\vec{k}\cdot(\vec{R}^{(1)}+\vec{\tau}^{(1)}_{\alpha})}. \tag{2.42}$$

We can reorder the terms in the exponents to obtain:

$$T_{kp}^{\alpha\beta} = \frac{1}{N^2\Omega} \sum_{\vec{R}^{(1)}} \sum_{\vec{R}^{(2)}} \sum_{\vec{k}'} \sum_{\vec{G'}^{(1)}} t_{\vec{k}'+\vec{G'}^{(1)}} e^{-i\vec{R}^{(1)}\cdot(\vec{k}-\vec{G}'^{(1)}-\vec{k}')} e^{i\vec{R}^{(2)}\cdot(\vec{p}-\vec{G}'^{(1)}-\vec{k}')} e^{i\left[(\vec{k}'+\vec{G}'^{(1)})\cdot(\vec{\tau}_{\alpha}^{(1)}-\vec{\tau}_{\beta}^{(2)})+\vec{p}\cdot\vec{\tau}_{\beta}^{(2)}-\vec{k}\cdot\vec{\tau}_{\alpha}^{(1)}\right]} \tag{2.43}$$

We can now use the properties of the Fourier transforms to simplify (proof in the Appendix A):

$$\frac{1}{N} \sum_{\vec{R}^{(1)}} e^{-i\vec{R}^{(1)}\cdot(\vec{k}-\vec{G}'^{(1)}-\vec{k}')} = \sum_{G^{\vec{(1)}}} \delta_{\vec{k}+\vec{G}^{(1)},\vec{k}'+\vec{G'}^{(1)}} \tag{2.44}$$

We obtain:

$$T_{kp}^{\alpha\beta} = \frac{1}{N^2\Omega} \sum_{\vec{G}^{(1)}} \sum_{\vec{G}^{(2)}} \sum_{\vec{k}'} \sum_{\vec{G'}^{(1)}} t_{\vec{k}'+\vec{G'}^{(1)}} \delta_{\vec{k}+\vec{G}^{(1)},\vec{k}'+\vec{G'}^{(1)}} \delta_{\vec{k}'+\vec{G}^{(1)},\vec{p}+\vec{G}^{(2)}} e^{i\left[(\vec{k}'+\vec{G}'^{(1)})\cdot(\vec{\tau}_{\alpha}^{(1)}-\vec{\tau}_{\beta}^{(2)})+\vec{p}\cdot\vec{\tau}_{\beta}^{(2)}-\vec{k}\cdot\vec{\tau}_{\alpha}^{(1)}\right]}. \tag{2.45}$$

We can now perform a few simplifications:

$$\begin{aligned} T_{kp}^{\alpha\beta} &= \frac{1}{N^2\Omega} \sum_{\vec{G}^{(1)}} \sum_{\vec{G}^{(2)}} t_{\vec{k}+\vec{G}^{(1)}} \delta_{\vec{k}+\vec{G}^{(1)},\vec{p}+\vec{G}^{(2)}} e^{i\left[(\vec{k}+\vec{G}^{(1)})\cdot(\vec{\tau}_{\alpha}^{(1)}-\vec{\tau}_{\beta}^{(2)})+\vec{p}\cdot\vec{\tau}_{\beta}^{(2)}-\vec{k}\cdot\vec{\tau}_{\alpha}^{(1)}\right]} \\ &= \frac{1}{N^2\Omega} \sum_{\vec{G}^{(1)}} \sum_{\vec{G}^{(2)}} t_{\vec{k}+\vec{G}^{(1)}} \delta_{\vec{k}+\vec{G}^{(1)},\vec{p}+\vec{G}^{(2)}} e^{i\left[(\vec{p}-\vec{k})\cdot\vec{\tau}_{\beta}^{(2)}+\vec{G}^{(1)}\cdot\vec{\tau}_{\alpha}^{(1)}-\vec{G}^{(1)}\cdot\vec{\tau}_{\beta}^{(2)}\right]}. \end{aligned} \tag{2.46}$$

The delta function gives us the condition:

$$\begin{aligned} \vec{k}+\vec{G}^{(1)} &= \vec{p}+\vec{G}^{(2)} \\ \vec{p}-\vec{k} &= \vec{G}^{(1)}-\vec{G}^{(2)} \end{aligned} \tag{2.47}$$

Using it, we obtain:

$$\begin{aligned} T_{kp}^{\alpha\beta} &= \frac{1}{N^2\Omega}\sum_{\vec{G}^{(1)}}\sum_{\vec{G}^{(2)}} t_{\vec{k}+\vec{G}^{(1)}}\delta_{\vec{k}+\vec{G}^{(1)},\vec{p}+\vec{G}^{(2)}} e^{i\left[\vec{G}^{(1)}\cdot\vec{\tau}_\beta^{(2)} - \vec{G}^{(2)}\cdot\vec{\tau}_\beta^{(2)} + G^{(1)}\cdot\vec{\tau}_\alpha^{(1)} - G^{(1)}\vec{\tau}_\beta^{(2)}\right]} \\ &= \frac{1}{N^2\Omega}\sum_{\vec{G}^{(1)}}\sum_{\vec{G}^{(2)}} t_{\vec{k}+\vec{G}^{(1)}}\delta_{\vec{k}+\vec{G}^{(1)},\vec{p}+\vec{G}^{(2)}} e^{-i\left[G^{(2)}\cdot\vec{\tau}_\beta^{(2)} - G^{(1)}\cdot\vec{\tau}_\alpha^{(1)}\right]} \\ . \end{aligned} \tag{2.48}$$

We will now introduce notation: $G_{n,m}^{(j)} = nG_1^{(j)} + mG_2^{(j)}$. Then the final hopping form is:

$$T_{kp}^{\alpha\beta} = \sum_{n_1,m_1}\sum_{n_2,m_2}\frac{t_{\vec{k}+\vec{G}^{(1)}}}{\Omega}\delta_{\vec{k}+\vec{G}^{(1)},\vec{p}+\vec{G}^{(2)}} e^{-i\left(\vec{G}_{n_2,m_2}^{(2)}\cdot\vec{\tau}_\beta^{(2)} - \vec{G}_{n_1,m_1}^{(1)}\cdot\vec{\tau}_\alpha^{(1)}\right)} \tag{2.49}$$

We will now make use of the NN approximation, since the BM model only includes hoppings between NN in the reciprocal space: $\vec{k} - \vec{p} = \vec{q}_j$. Here, $\vec{q}_j$ is a vector connecting NN in the reciprocal space of the lattice generated by repeated hoppings. It is schematically shown in Fig. 2.4 (b) and (c). Imposing that approximation simplifies our hopping term to three matrices $(T_i)^{\alpha\beta}$:

$$(T_i)^{\alpha\beta} = we^{-i\left(\vec{G}_{n_2,m_2}^{(2)}\cdot\vec{\tau}_\beta^{(2)} - \vec{G}_{n_1,m_1}^{(1)}\cdot\vec{\tau}_\alpha^{(1)}\right)}. \tag{2.50}$$

Here $w = \frac{t_{\vec{k}+\vec{G}^{(1)}}}{\Omega} \approx \frac{t_{K^{(1)}}}{\Omega}$. The approximation comes from the fact that the hopping t_k decays exponentially with respect to $|k|$. We will now consider the possible forms of the resulting matrices for $j = 1, 2, 3$ (details in the Appendix A). For $j = 1$, we have $(n_1, m_1) = (0, 0)$.

$$T_1 = w\begin{bmatrix} 1 & 1 \\ 1 & 1 \end{bmatrix} \tag{2.51}$$

For $j = 2$, $(n_2, m_2) = (0, 1)$:

$$T_2 = w\begin{bmatrix} e^{-i\frac{2\pi}{3}} & e^{i\frac{2\pi}{3}} \\ 1 & e^{-i\frac{2\pi}{3}} \end{bmatrix} \tag{2.52}$$

and for $j = 3$, $(n_3, m_3) = (1, 0)$:

$$T_3 = w \begin{bmatrix} e^{i\frac{2\pi}{3}} & e^{-i\frac{2\pi}{3}} \\ 1 & e^{i\frac{2\pi}{3}} \end{bmatrix} \tag{2.53}$$

The final form of the full BM Hamiltonian is then:

$$H^K(\vec{k}) = \begin{pmatrix} h_\theta^K(\vec{k}) & wT_1 & wT_2 & wT_3 & ... \\ wT_1 & h_\theta^K(\vec{k}-\vec{q_1}) & 0 & 0 & ... \\ wT_2 & 0 & h_\theta^K\vec{k}-\vec{q_2}) & 0 & ... \\ wT_3 & 0 & 0 & h_\theta^K(\vec{k}-\vec{q_3}) & ... \\ ... & ... & ... & ... & ... \end{pmatrix} \tag{2.54}$$

The Bistritzer-MacDonald model provides an effective description of the low-energy electronic structure of twisted bilayer graphene near the Dirac points. By incorporating the moiré periodicity and interlayer tunnelling between rotated graphene layers, the model captures the formation of flat bands and the emergence of correlated electron behaviour at magic angles. This Hamiltonian forms the foundation for understanding many of the novel electronic phases observed in twisted bilayer graphene, including superconductivity and correlated insulator states [8, 9, 27].

2.3.3 Topology and Chern numbers

The emergence of flat bands and correlated phases in twisted graphene multilayers has drawn attention to the role of topology in these systems. Topological band invariants, such as Chern numbers and Berry curvature, have become essential tools for understanding the unconventional superconductivity, anomalous Hall effects, and other quantum phenomena that emerge in moiré superlattices.

In particular, the understanding of various Hall effects begins with the integer quantum Hall effect, which refers to the quantization of the Hall conductance of a material at integer multiples of e^2/h. This integer is equal to the Chern number, which in turn is associated with the Berry curvature of electronic Bloch bands. Therefore, the physical meaning of non-zero Chern numbers refers to quantized conductance and is a signature of quantum Hall states. It may also indicate topological insulating behaviour of the system, if the time reversal symmetry is broken. In such systems, for specific Fermi levels, electrical transport occurs exclusively through the edge states, while the bulk remains insulating. The Chern numbers are computed as integrals of the Berry curvature, often interpreted as a fictitious magnetic fields, over the toroidal Brillouin zone. As such, they play a crucial role in identifying emergent topological phases and provide insight into the geometry of the wavefunctions. Specifically, the Chern number associated with the nth energy band is defined as:

$$c_n = \frac{1}{2\pi i} \int_{T^2} d^2k F_{12}^n(k) \tag{2.55}$$

where the Berry connection $A_\mu^n(k)$ $(\mu = 1, 2)$ and the associated field strength $F_{12}(k)$ are given by:

$$\begin{aligned} A_\mu^n(k) &= \langle n(k)| \, \partial_\mu \, |n(k)\rangle \\ F_{12}^n(k) &= \partial_1 A_2^n(k) - \partial_2 A_1^n(k). \end{aligned} \tag{2.56}$$

Here $|n(k)\rangle$ is a normalized wave function of the nth band, such that $H(k)\,|n(k)\rangle = E_n\,|n(k)\rangle$. The derivative ∂_μ stands for $\partial/\partial k_\mu$.

In this section, we focus on quantitative description of topology of the structure using Chern numbers. Depending on the system and its geometry, we employ two different methods to calculate it.

Graphical method

In the nanoribbon geometry, where the system is periodic in one direction and finite in the other, we employ a graphical method to determine the Chern number. This approach is analogous to the case of Landau levels in a magnetic field, where non-zero Chern numbers correspond to energy levels connected by chiral edge modes traversing the bulk gap. In nanoribbons, similar chiral edge states emerge within topological bands. By identifying and counting the number of edge states crossing the energy gap, we can assign an effective Chern number to the gap.

The microscopic properties of the wave functions of the flat band and the edge states are characterized by the local density of states (LDOS) for a representative choice of the magnetic field. We use the following definition of LDOS:

$$n(x_i, y_i, E) = N_{k_{\mathrm{1D}}}^{-1} \sum_{\lambda, k_{\mathrm{1D}}} |\psi_{k_{1D},\lambda}(x_i, y_i)|^2 \delta(E - E_{k_{1D},\lambda}). \tag{2.57}$$

Here, n is the LDOS for given coordinates x_i and y_i at a given energy. $N_{\mathrm{k_{1D}}}$ is the normalization constant and relates to the number of states considered, λ is the eigenvalue index, which together with the wave vector k_{1D} enumerates the eigenvalue $E_{k_{\mathrm{1D}},\lambda}$ and the eigenvector $\psi_{k_{1D},\lambda}(x_i, y_i)$.

Numerical method

In the bulk case, we calculate the Chern numbers using a numerical procedure on a discretized BZ [296]. For a single isolated band, the Chern number is given by:

$$c_n = \frac{1}{2\pi i} \sum_l F_{12}(k_l) \tag{2.58}$$

where the sum runs over the lattice points $\vec{k}_l$ in the discretized BZ, and $F_{12}(\vec{k}_l)$ is the lattice field strength defined as

$$F_{12}(k_l) \equiv \ln \left(U_1(k_l) U_2(k_l + \hat{1}) U_1(k_l + \hat{2})^{-1} U_2(k_l)^{-1} \right) \tag{2.59}$$

Here, $U_\mu(\vec{k}_l)$ are the link variables, constructed from the normalized overlap of wave functions at neighbouring k-points:

$$U_\mu(k_l) \equiv \langle n(k_l) | n(k_l + \hat{\mu}) \rangle / | \langle n(k_l) | n(k_l + \hat{\mu}) \rangle |, \tag{2.60}$$

where $\mu = 1, 2$ labels the two directions in the 2D BZ, and $\hat{\mu}$ denotes the discrete step in the μ-th direction.

This method generalizes naturally to the multiband case, where one computes the total Chern number associated with a group of n occupied bands. To do so, we define n-bands link variable $U_\mu(\vec{k}_i)$ from the chosen set of wave functions $\psi = (|\phi_1\rangle, ..., |\phi_n\rangle)$ as

$$U_\mu(\vec{k}_i) \equiv \det \psi^\dagger(\vec{k}_i)\psi(\vec{k}_i + \hat{\mu})/|\det \psi^\dagger(\vec{k}_i)\psi(\vec{k}_i + \hat{\mu})| \tag{2.61}$$

The corresponding lattice field strength is

$$F(\vec{k}_i) = \ln\left(U_1(\vec{k}_i)U_2(\vec{k}_i + \hat{1})U_1(\vec{k}_i + \hat{2})^{-1}U_2(\vec{k}_i)^{-1}\right) \tag{2.62}$$

The Chern number for the n bands is then defined

$$c_\psi \equiv (2\pi i)^{-1} \sum_j F(\vec{k}_j) \tag{2.63}$$

Note that in both cases, since $U_\mu(\vec{k}_i)$ is normalized, $F(\vec{k}_i)$ is purely imaginary, and the Chern number c_ψ is real.

2.4 Mean field approximations

In this section, we describe the mean-field approaches employed in our work to account for electron-electron interactions—namely, the Hartree-Fock method and DFT. These methods reduce the complexity of the many-body problem by approximating the interacting electron system with an effective single-particle picture, where each electron moves in a self-consistent potential generated by all other electrons. While Hartree-Fock explicitly treats exchange interactions through a non-local potential, DFT incorporates the exchange interactions via a local exchange functionals that depend on the electron density. Both approaches provide valuable insight into the electronic structure of materials and serve as the foundation for more advanced treatments of correlations.

2.4.1 Hartree-Fock approximation

The Hartree-Fock approximation replaces the many body wavefunction with a single Slater determinant of effective orbitals that are solutions of an effective Hamiltonian, which is quadratic in the electron creation and annihilation operators. This effective Hamiltonian can be readily diagonalized, making the problem computationally tractable while still capturing key interaction effects. We will use this approach to study twisted graphene multilayers.

We start by considering the many-body Hamiltonian:

$$H = \sum_{\substack{i,j,\sigma \\ i \neq j}} t_{ij} c^{\dagger}_{i,\sigma} c_{j,\sigma} + \frac{1}{2} \sum_{\substack{ijkl \\ \sigma,\sigma'}} V_{ijkl} c^{\dagger}_{i,\sigma} c^{\dagger}_{j,\sigma'} c_{k,\sigma'} c_{l,\sigma} \tag{2.64}$$

Since the second term contains two-body operators, it is the most challenging. In the Hartree-Fock approximation, we can write it as one-body terms. We will use Wick's theorem to do so, and replace two of the operators by their average. We can choose four different expectation values, which leave us with four terms:

$$\begin{aligned} H_I &= \frac{1}{2} \sum_{\substack{ijkl \\ \sigma,\sigma'}} \langle ij| V |kl\rangle \; c^{\dagger}_{i,\sigma} c^{\dagger}_{j,\sigma'} c_{k,\sigma'} c_{l,\sigma} \\ &\approx \frac{1}{2} \sum_{\substack{ijkl \\ \sigma,\sigma'}} \langle ij| V |kl\rangle \left(\langle c^{\dagger}_{j\sigma'} c_{k\sigma'} \rangle \, c^{\dagger}_{i\sigma} c_{l\sigma} + \langle c^{\dagger}_{i\sigma} c_{l\sigma} \rangle \, c^{\dagger}_{j\sigma'} c_{k\sigma'} \right) \\ &\quad - \frac{1}{2} \sum_{\substack{ijkl \\ \sigma,\sigma'}} \langle ij| V |kl\rangle \left(\langle c^{\dagger}_{j\sigma'} c_{l\sigma} \rangle \, c^{\dagger}_{i\sigma} c_{k\sigma'} + \langle c^{\dagger}_{i\sigma} c_{k\sigma'} \rangle \, c^{\dagger}_{j\sigma'} c_{l\sigma} \right) \delta_{\sigma\sigma'} \end{aligned} \tag{2.65}$$

Here $\langle ij| V |kl\rangle = V_{ijkl}$. We note, that $\langle c^{\dagger}_{i\sigma} c_{k\sigma'} \rangle$ will be zero if $\sigma \neq \sigma'$, hence we have $\delta_{\sigma\sigma'}$. Since $\langle ij| V |kl\rangle = \langle ji| V |lk\rangle$, we can simplify our expression to:

$$H_I = \sum_{\substack{ijkl \\ \sigma,\sigma'}} \langle ij| V |kl\rangle \left(\langle c^{\dagger}_{j\sigma'} c_{k\sigma'} \rangle \, c^{\dagger}_{i\sigma} c_{l\sigma} \right) - \sum_{\substack{ijkl \\ \sigma,\sigma'}} \langle ij| V |kl\rangle \left(\langle c^{\dagger}_{j\sigma'} c_{l\sigma} \rangle \, c^{\dagger}_{i\sigma} c_{k\sigma'} \, \delta_{\sigma\sigma'} \right) \tag{2.66}$$

In the second term, we will exchange the dummy index k with l. This gives us:

$$H_I = \sum_{\substack{ijkl \\ \sigma,\sigma'}} \langle ij|\, V \,|kl\rangle \left(\langle c^\dagger_{j\sigma'} c_{k\sigma'} \rangle \, c^\dagger_{i\sigma} c_{l\sigma} \right) - \sum_{\substack{ijkl \\ \sigma,\sigma'}} \langle ij|\, V \,|lk\rangle \left(\langle c^\dagger_{j\sigma'} c_{k\sigma} \rangle \, c^\dagger_{i\sigma} c_{l\sigma'} \, \delta_{\sigma\sigma'} \right). \tag{2.67}$$

We can now factor out the operators:

$$H_I = \sum_{\substack{ijkl \\ \sigma,\sigma'}} \left(\langle ij|\, V \,|kl\rangle - \langle ij|\, V \,|lk\rangle \, \delta_{\sigma\sigma'} \right) \langle c^\dagger_{j\sigma'} c_{k\sigma'} \rangle c^\dagger_{i\sigma} c_{l\sigma}. \tag{2.68}$$

The full Hartree-Fock Hamiltonian then has the form:

$$H_{HF} = \sum_{\substack{i,j,\sigma \\ i\neq j}} t_{ij} c^\dagger_{i,\sigma} c_{j,\sigma} + \sum_{\substack{ijkl \\ \sigma,\sigma'}} \left(\langle ij|\, V \,|kl\rangle - \langle ij|\, V \,|lk\rangle \, \delta_{\sigma\sigma'} \right) \langle c^\dagger_{j\sigma'} c_{k\sigma'} \rangle c^\dagger_{i\sigma} c_{l\sigma}. \tag{2.69}$$

To simplify the notation we will define $\rho^0_{jk\sigma'} = \langle c^\dagger_{j\sigma'} c_{k\sigma'} \rangle$. This Hamiltonian can be diagonalized in a self-consistent manner, in which we start with a trial density $\rho^0_{jk\sigma'}$ and carry out the calculation as long as a desired convergence is reached between the input and output density.

We can now rewrite this equation, defining an effective hopping t'_{il}:

$$t'_{il} = \left[t_{il} + \sum_{j,k,\sigma'} \left(\langle ij|\, V \,|kl\rangle - \langle ij|\, V \,|lk\rangle \, \delta_{\sigma\sigma'} \right) \rho^0_{jk\sigma'} \right] \tag{2.70}$$

which gives us the Hamiltonian in the form:

$$H_{HF} = \sum_{i,l,\sigma} t'_{il} c^\dagger_{i\sigma} c_{l\sigma} \tag{2.71}$$

It is important to note that if the hopping parameters of the tight-binding Hamiltonian are fitted to the output of a Hartree-Fock-based mean-field calculation, the resulting hopping parameters t'_{ij} will already incorporate interaction effects. Consequently, care must be taken to avoid double-counting these interactions in subsequent calculations. The same consideration applies when using hopping parameters derived from DFT-based mean-field calculations. This effective hopping is analogous to the *ab initio* fitted hopping used in our tight-binding calculations for graphene nanostructures. As such, our tight-binding model already incorporates mean-field interactions. To perform a consistent Hartree-Fock calculation and avoid double counting, it is necessary to subtract this mean-field contribution. Let us now consider:

$$t'_{il} = t_{il} + \underbrace{\sum_{j,k,\sigma'} \left(\langle ij| V |kl\rangle - \langle ij| V |lk\rangle \delta_{\sigma\sigma'} \right) \langle c^{\dagger}_{j\sigma'} c_{k\sigma'} \rangle}_{\tau_{il}} \tag{2.72}$$

We have then:

$$t'_{il} = t_{il} + \tau_{il} \tag{2.73}$$

t'_{il} is the effective mean-field hopping, which we do have; t_{il} is a bare, single particle hopping, which is not directly known. τ_{il} can be calculated. We can therefore express:

$$t_{il} = t'_{il} - \tau_{il} \tag{2.74}$$

We can write the original, many-body Hamiltonian 2.64 as:

$$H = \sum_{\substack{i,j,\sigma \\ i\neq j}} \left(t'_{ij} - \tau_{ij} \right) c^{\dagger}_{i,\sigma} c_{j,\sigma} + \frac{1}{2} \sum_{\substack{ijkl \\ \sigma,\sigma'}} V_{ijkl} c^{\dagger}_{i,\sigma} c^{\dagger}_{j,\sigma'} c_{k,\sigma'} c_{l,\sigma} \tag{2.75}$$

Reorganizing the terms, we obtain:

$$H = \sum_{\substack{i,j,\sigma \\ i\neq j}} t'_{ij} c^{\dagger}_{i,\sigma} c_{j,\sigma} + \frac{1}{2} \sum_{\substack{ijkl \\ \sigma,\sigma'}} V_{ijkl} c^{\dagger}_{i,\sigma} c^{\dagger}_{j,\sigma'} c_{k,\sigma'} c_{l,\sigma} - \sum_{\substack{i,j,\sigma \\ i\neq j}} \tau_{ij} c^{\dagger}_{i,\sigma} c_{j,\sigma} \tag{2.76}$$

We can apply the Hartree-Fock approximation again to the interacting term, remembering that this time, the interaction refers to a modified system (multilayer graphene or a finite structure):

$$\frac{1}{2}\sum_{\substack{ijkl\\ \sigma,\sigma'}} V_{ijkl} c^{\dagger}_{i,\sigma} c^{\dagger}_{j,\sigma'} c_{k,\sigma'} c_{l,\sigma} \approx \sum_{il}\sum_{j,k,\sigma'} \left(\langle ij|\, V\, |kl\rangle - \langle ij|\, V\, |lk\rangle\, \delta_{\sigma\sigma'}\right) \underbrace{\langle c^{\dagger}_{j\sigma'} c_{k\sigma'}\rangle}_{\rho_{jk\sigma'}} c^{\dagger}_{i\sigma} c_{l\sigma} \tag{2.77}$$

Now, if we insert it back into Eq. 2.75

$$\begin{aligned} H =& \sum_{\substack{i,j,\sigma\\ i\neq j}} t'_{ij} c^{\dagger}_{i,\sigma} c_{j,\sigma} + \sum_{il}\sum_{j,k,\sigma'} \left(\langle ij|\, V\, |kl\rangle - \langle ij|\, V\, |lk\rangle\, \delta_{\sigma\sigma'}\right) \rho_{jk\sigma} c^{\dagger}_{i\sigma} c_{l\sigma} \\ &- \sum_{\substack{i,j,\sigma\\ i\neq j}}\sum_{j,k,\sigma'} \left(\langle ij|\, V\, |kl\rangle - \langle ij|\, V\, |lk\rangle\, \delta_{\sigma\sigma'}\right) \rho^{0}_{jk\sigma} c^{\dagger}_{i\sigma} c_{l\sigma} \end{aligned} \tag{2.78}$$

This can be simplified to:

$$H = \sum_{\substack{i,j,\sigma\\ i\neq j}} t'_{ij} c^{\dagger}_{i,\sigma} c_{j,\sigma} + \sum_{il}\sum_{j,k,\sigma'} \left(\langle ij|\, V\, |kl\rangle - \langle ij|\, V\, |lk\rangle\, \delta_{\sigma\sigma'}\right) \left(\rho_{jk\sigma} - \rho^{0}_{jk\sigma}\right) c^{\dagger}_{i\sigma} c_{l\sigma} \tag{2.79}$$

This is the final form of Hartree-Fock approximation, where ρ_0 refers to the density matrix from bulk graphene, and ρ is the density matrix to be determined self-consistently. If we applied this Hamiltonian to the case of bulk graphene, $\rho = \rho_0$, and we would recover the original bulk graphene solution.

Hartree approximation

We can now apply a classical Hartree approximation to our Hamiltonian. Then, only the electrostatic density-density interaction is present, which is equivalent to neglecting the scattering term, and considering only direct interaction for $j = k, i = l$:

$$H = \sum_{\substack{i,j,\sigma\\ i\neq j}} t'_{ij} c^{\dagger}_{i,\sigma} c_{j,\sigma} + \sum_{ij,\sigma} \left(\langle ij|\, V\, |ji\rangle\right) \left(\rho_{jj\sigma} - \rho^{0}_{jj\sigma}\right) c^{\dagger}_{i\sigma} c_{i\sigma} \tag{2.80}$$

Introducing the particle number operator $\hat{n}_{i\sigma} = c^{\dagger}_{i\sigma} c_{i\sigma}$, we have:

$$H = \sum_{\substack{i,j,\sigma \\ i \neq j}} t'_{ij} c^{\dagger}_{i,\sigma} c_{j,\sigma} + \sum_{i,\sigma} \hat{n}_{i\sigma} \sum_{j} \left(\langle ij | V | ji \rangle \right) \left(\langle \hat{n}_{j\sigma} \rangle - \langle \hat{n}^{0}_{j\sigma} \rangle \right) \tag{2.81}$$

Hubbard model

Let us now consider the original many-body Hamiltonian from Eq. 2.64, restricted to onsite interaction terms only, i.e., $i = j = k = l$. This leads to the Hubbard Hamiltonian:

$$H = \sum_{\substack{i,j,\sigma \\ i \neq j}} t_{ij} c^{\dagger}_{i,\sigma} c_{j,\sigma} + \frac{1}{2} \sum_{i,\sigma,\sigma'} V_{iiii} c^{\dagger}_{i,\sigma} c^{\dagger}_{i,\sigma'} c_{i,\sigma'} c_{i,\sigma} \tag{2.82}$$

From here on, we denote the Coulomb repulsion V_{iiii} as U. Expanding the spin indices explicitly and applying the Pauli exclusion principle, we obtain:

$$H = \sum_{\substack{i,j,\sigma \\ i \neq j}} t_{ij} c^{\dagger}_{i,\sigma} c_{j,\sigma} + \frac{1}{2} \sum_{i} U \left(c^{\dagger}_{i\uparrow} c^{\dagger}_{i\downarrow} c_{i\downarrow} c_{i\uparrow} + c^{\dagger}_{i\downarrow} c^{\dagger}_{i\uparrow} c_{i\uparrow} c_{i\downarrow} \right) \tag{2.83}$$

That simplifies to:

$$H = \sum_{\substack{i,j,\sigma \\ i \neq j}} t_{ij} c^{\dagger}_{i,\sigma} c_{j,\sigma} + \sum_{i} U \hat{n}_{i\uparrow} \hat{n}_{i\downarrow} \tag{2.84}$$

where $n_{i\sigma} = c^{\dagger}_{i\sigma} c_{i\sigma}$ is spin resolved particle operator. We can now apply the Hartree-Fock approximation. The mean-field Hamiltonian becomes:

$$H_{HF} = \sum_{\substack{i,j,\sigma \\ i \neq j}} t_{ij} c^{\dagger}_{i,\sigma} c_{j,\sigma} + U \sum_{i} \hat{n}_{i\uparrow} \langle \hat{n}_{i\downarrow} \rangle + \hat{n}_{i\downarrow} \langle \hat{n}_{i\uparrow} \rangle. \tag{2.85}$$

2.4.2 Density Functional Theory

DFT is a widely used method for calculating the properties of complex electronic systems such as molecules and solids. Its central idea is to describe the system in terms of its electronic density rather than the many-body wavefunction. This approach dramatically simplifies the many-body problem: while exact solutions scale exponentially with the number of electrons, DFT calculations scale polynomially, making them computationally feasible for large systems. DFT is built on the Hohenberg-Kohn (HK) theorem and the Kohn-Sham (KS) formalism. In the following, we'll briefly describe both of these concepts, relying on the derivation from Ref. [297].

Let us consider the many-body Hamiltonian for a system of N electrons:

$$\hat{H} = \hat{T} + \hat{V}_{ext} + \hat{V} \tag{2.86}$$

Here, $\hat{T}$ is the kinetic energy operator, $\hat{V}_{ext}$ is the external potential of ions and $\hat{V}$ denotes the electron-electron interaction. According to the HK theorem, the expectation value of the Hamiltonian is a unique functional of the ground-state electron density $n_0(\vec{r})$. Importantly, the operators $\hat{T}$ and $\hat{V}$ are universal—they are the same for all electronic systems interacting via the Coulomb potential, while the external potential V_{ext} uniquely defines the Hamiltonian and thus all ground-state properties [298]. This implies that the mapping from the external potential to the ground-state density is invertible. Therefore, knowledge of the ground-state density $n_0(\vec{r})$ is, in principle, sufficient to determine all properties of the interacting many-body system.

An important variational principle associated with the HK theorem [298] states that the ground state energy is a unique functional of the electron density $n_0(\vec{r})$:

$$\mathcal{E}[n] \equiv \langle \Psi_0[n] | \, \hat{T} + \hat{V}_{ext} + \hat{V} \, | \Psi_0[n] \rangle \tag{2.87}$$

When density n is equal to the ground state density n_0, the functional $\mathcal{E}$ yields the exact ground state energy $\mathcal{E}_0$. Therefore, by varying the density to minimize $\mathcal{E}[n]$ one can, determine the ground-state energy—provided the exact form of the functional is known or can be accurately approximated.

We now turn to the KS formalism [299], which offers a practical computational framework for determining the ground-state electron density $n_0(\vec{r})$. The central idea is to map the original interacting many-body problem onto an auxiliary non-interacting system, such that both systems share the same ground-state density. This is achieved by introducing an effective external potential V_s, chosen so that the non-interacting system reproduces the exact density of the interacting one, which can be used to calculate $\mathcal{E}[n]$. This scheme provides us with a self-consistent way of computing the ground state density - we start with a trial $n(\vec{r})$, use it to calculate V_s and obtain a new density, which serves as an input for the next iteration until desired convergence is reached. Note that we're solving for a non-interacting ground state, which is much more computationally tractable than the interacting problem. The Hamiltonian we're diagonalizing has then the form:

$$H_s = T_s + V_s. \tag{2.88}$$

Applying the HK theorem to this system, we can write the energy functional as:

$$\mathcal{E}_s[n] = T_s[n] + \int V_s(\vec{r})n(\vec{r})dr. \tag{2.89}$$

T_s refers here to the kinetic energy of non-interacting particles, it is thus a different functional from previously considered $T[n]$. The ground state density can be calculated using:

$$n_s(\vec{r}) = \sum_{i=1}^{N} |\phi_i(\vec{r})|^2, \tag{2.90}$$

where ϕ_i are wavefunctions satisfying the KS equation:

$$\left[T_s + V_s\right] \phi_i(\vec{r}) = \mathcal{E}_i \phi_i(\vec{r}) \tag{2.91}$$

However, since our original problem involves interacting electrons, we must determine a form of the effective potential V_s such that the ground-state density of the non-interacting system matches that of the interacting system under the external potential V_{ext}. The strategy is to solve for the electron density within the non-interacting system and then use this density in an approximate functional for the total energy of the interacting system.

First we rewrite the energy functional $\mathcal{E}[n]$ in the following form

$$\begin{aligned}
\mathcal{E}[n] &= T_s[n] + \left\{ T[n] - T_s[n] + V[n] - \frac{e^2}{2}\int\int \frac{n(\vec{r})n(\vec{r}')}{|\vec{r}-\vec{r}'|}drdr' \right\} \\
&+ \frac{e^2}{2}\int\int \frac{n(\vec{r})n(\vec{r}')}{|\vec{r}-\vec{r}'|}drdr' + \int n(\vec{r})V_{ext}(\vec{r})dr \\
&\equiv T_s + \frac{e^2}{2}\int\int \frac{n(\vec{r})n(\vec{r}')}{|\vec{r}-\vec{r}'|}drdr' + \int n(\vec{r})V_{ext}(\vec{r})dr + \int n(\vec{r})V_{ext}(\vec{r})dr + \mathcal{E}_{xc}[n].
\end{aligned} \tag{2.92}$$

Here we have added and subtracted the kinetic $T_s[n]$ and Hartree terms. Consequently, we defined the terms in braces as an exchange-correlation energy functional $\mathcal{E}_{xc}[n]$. This term includes all the information about electron-electron interactions. This way, we can focus on developing reasonable approximations for $\mathcal{E}_{xc}[n]$.

Using the variational principle, it can be shown that:

$$V_s(\vec{r}) = V_{ext}(\vec{r}) + \frac{e^2}{2}\int \frac{n(\vec{r})}{|\vec{r}-\vec{r}'|}dr' + V_{xc}[n(\vec{r})]. \tag{2.93}$$

The first term represents the external potential, the second is the (electrostatic) Hartree potential, and the last, which is the core approximation in the DFT scheme, is the exchange-correlation potential. This way, we have the needed components to perform the KS self-consistent scheme.

There are many elaborate ways of approximating the exchange-correlation potential. In our calculation, we will use the simplest one, the Local Density Approximation (LDA).

2.5 Beyond the mean field description

While mean-field methods like Hartree–Fock and DFT provide valuable insights into electronic structure, they often rely on approximations that limit their accuracy, especially in strongly correlated systems. To overcome these limitations, methods like Configuration Interaction, which builds the many-body wavefunction from a linear combination of

Slater determinants, and the Tensor Networks (TN), which, depending on the Hamiltonian connectivity, reduce the size of the relevant Hilbert space, have been developed. In this chapter, we provide an overview of these methods, highlighting their principles, strengths, and computational challenges.

2.5.1 Configuration Interaction

The CI method treats the full Hamiltonian given in Eq. 2.64. It seeks to access a given number of states written as a linear combination of configurations of electrons distributed on single-particle energy levels. The derivation below follows the approach outlined in Ref. [300].

Most quantum many-body problems result in a sparse matrix representation of the Hamiltonian, with only a small number of elements being non-zero. However, before diagonalizing such a matrix, we must first express the many-body Hamiltonian—formulated in the language of second quantization—as a sparse Hermitian matrix. We will show the appropriate procedure on an example of a Hubbard Hamiltonian, similar to the one we have already introduced for twisted multilayers:

$$H = t \sum_{i,j,\sigma} c^{\dagger}_{i\sigma} c_{j\sigma} + U \sum_{i} n_{i\uparrow} n_{i\downarrow} \tag{2.94}$$

where U is the on-site Coulomb repulsion parameter. Hubbard Hamiltonian is a minimal Hamiltonian containing electron-electron interaction, which however is able to capture the essential physics of a variety of systems. We now define the configurations in which we will expand the solution of the Schrödinger equation $H\phi = E\phi$. We focus on a specific site i, in which case there are four possible states:

- $|0\rangle$ = no electron at site i
- $c^{\dagger}_{i\downarrow} |0\rangle$ = one spin-down electron at site i
- $c^{\dagger}_{i\uparrow} |0\rangle$ = one spin-up electron at site i

- $c^\dagger_{i\downarrow} c^\dagger_{i\uparrow} |0\rangle$ = one spin-down and one spin-up electron at site i.

Considering all L sites of our system we get 4^L configurations which number represents the dimension of the full Hilbert space. Since we are considering one orbital per site, so these two terms can be used interchangeably. Since the dimension grows exponentially with system size, the problem quickly becomes intractable, even for modern supercomputers. To address this challenge, one can exploit the symmetries of the system to block-diagonalize the Hamiltonian, thereby reducing its complexity. Alternatively, the size of the active Hilbert space can be reduced by considering special kinds of configurations, e.g. excitons, biexcitons, etc. [301], or restricting the set of active orbitals—both of which are implemented in the Section 2.5.2. When the entire Hilbert space is considered, the method is known as Full Configuration Interaction (FCI) or Exact Diagonalization.

We now demonstrate how to construct a basis for a system with L sites and N electrons, where $N_\uparrow$ have spin up and $N_\downarrow$ have spin down. The Hamiltonian conserves the number of electrons and the spin polarization S_z, therefore we can split the task into subspaces with fixed number of $N_\uparrow$ and $N_\downarrow$. First, we must establish a consistent convention for numbering the sites, which will be used throughout the calculation. In the case of the Hubbard model, it can be convenient to order the electron states first by spin (spin-up followed by spin-down), and then by site index. That is:

$$c^\dagger_{3\uparrow} c^\dagger_{2\uparrow} c^\dagger_{1\uparrow} c^\dagger_{3\downarrow} c^\dagger_{0\downarrow} |0\rangle \, . \tag{2.95}$$

This ordering has the advantage that nearest-neighbour hopping terms in the Hamiltonian do not introduce complicated phase factors when acting on the basis states. To determine the number of basis states, we must solve a combinatorial problem: distributing $N_\downarrow$ and $N_\uparrow$ electrons over L sites. The total number of basis states for fixed $N_\uparrow$ and $N_\downarrow$ is given by $\begin{pmatrix} L \\ N_\uparrow \end{pmatrix} \begin{pmatrix} L \\ N_\downarrow \end{pmatrix}$. If we sum over all possible configurations, we recover the full Fock space dimension:

$$\sum_{N_\uparrow=0}^{L} \sum_{N_\downarrow=0}^{L} \begin{pmatrix} L \\ N_\uparrow \end{pmatrix} \begin{pmatrix} L \\ N_\downarrow \end{pmatrix} = 2^L 2^L = 4^L \tag{2.96}$$

which matches the expected result.

We now illustrate how this basis can be implemented on a computer using an example with $L = 4$ sites, $N_\uparrow = 3$ and $N_\downarrow = 2$. The state in Eq. 2.95 can be represented as a pair of bit patterns:

$$c^\dagger_{3\uparrow} c^\dagger_{2\uparrow} c^\dagger_{1\uparrow} c^\dagger_{3\downarrow} c^\dagger_{0\downarrow} |0\rangle \rightarrow (\uparrow, \uparrow, \uparrow, 0) \times (\downarrow, 0, 0, \downarrow) \rightarrow 1110 \times 1001. \tag{2.97}$$

Here we denote an occupied state with "1" and an empty state with "0". The number of states for a complete basis set in the subspace $L = 4$, $N_\uparrow = 3$, and $N_\downarrow = 2$, can be computed using the formula:

$$\binom{L}{N_\uparrow} \binom{L}{N_\downarrow} = \binom{4}{3} \binom{4}{2} = 4 \cdot 6 = 24. \tag{2.98}$$

The four configurations for spin-up electrons are:

- $n = 0 \quad 0111 = 7$
- $n = 1 \quad 1011 = 11$
- $n = 2 \quad 1101 = 13$
- $n = 3 \quad 1110 = 14$

The six configurations for spin-down electrons are:

- $m = 0 \quad 0011 = 3$
- $m = 1 \quad 0101 = 5$
- $m = 2 \quad 0110 = 6$
- $m = 3 \quad 1001 = 9$
- $m = 4 \quad 1010 = 10$

- $m = 5 \quad 1100 = 12$

In the above, we have ordered the configurations by the integer number the binary representation corresponds to. We have also labelled each configuration by integers n for spin up and m for spin down, and can now create a composite index $l = m \cdot 6 + n$. The example state corresponds to $n = 3$ and $m = 3$, which gives us $l = 18$.

Now that we have constructed the basis set, we can apply the Hamiltonian (2.94) to each of them to obtain the matrix elements. Assuming periodic boundary conditions, we get e.g.:

- $\uparrow$-hopping $(|1110\rangle \times |1001\rangle) \to t(-|0111\rangle + |1101\rangle) \times |1001\rangle$
- $\downarrow$-hopping $(|1110\rangle \times |1001\rangle) \to t\,|1110\rangle \times (|1010\rangle + |0101\rangle)$
- U-term $(|1110\rangle \times |1001\rangle) \to U\,|1110\rangle \times |1001\rangle$

We can now use our list of configurations and find the new indices of our resulting states to create a Hamiltonian matrix. Since our example is very small, we can do it directly. In practice, one has to use hashing or fast search algorithms to perform this operation in finite time and using reasonable memory resources. Built-in dictionary or map data structures available in programming languages like C++ and Python typically provide good performance for this purpose. In our case, we get:

- $\uparrow$-hopping $|18\rangle \to t(-|3\rangle + |15\rangle)$
- $\downarrow$-hopping $|18\rangle \to t(|22\rangle + |23\rangle)$
- U-term $|18\rangle \to U\,|18\rangle$.

To get the full Hamiltonian matrix, we would have to repeat this operation for each of the 24 basis states.

This example illustrates how to construct a basis of electron configurations for a given system and apply the Hamiltonian to compute its matrix elements. While we demonstrated the procedure using the Hubbard Hamiltonian, the same approach can be applied to other Hamiltonians as well. Once the matrix is constructed, it can be diagonalized to obtain the energy spectrum. For large systems, iterative algorithms such as the Lanczos method are commonly used to extract the low-energy states efficiently.

2.5.2 Density Functional Theory + Configuration Interaction

In this section, we show how one can combine DFT and CI methods. We start off once again, considering the many-body Hamiltonian 2.7:

$$H = \sum_{i}^{N} \left[\frac{p_i^2}{2m} + V_{ext}(\vec{r}_i) \right] + \sum_{i<j} \frac{e^2}{|\vec{r}_i - \vec{r}_j|}, \tag{2.99}$$

In the DFT formalism, the KS orbitals satisfy:

$$\left[-\nabla_{\vec{r}}^2 + V_{KS}(\vec{r}) \right] \phi_\alpha(\vec{r}) = \epsilon_\alpha \phi_\alpha(\vec{r}), \tag{2.100}$$

where $V_{KS}(\vec{r}) = V_{ext}(\vec{r}) + V_H(\vec{r}) + V_{XC}(\vec{r})$. $V_{KS}(\vec{r})$ is the KS potential, $V_{ext}(\vec{r})$ is the external potential of ions, $V_H(\vec{r})$ is the Hartree potential and $V_{XC}(\vec{r})$ is the exchange-correlation potential. ϵ_α are the KS energy levels and ϕ_α are the KS orbitals. We will use the KS orbitals to expand our many-body Hamiltonian:

$$H = \sum_{\substack{\alpha\beta,\sigma \\ i\neq j}} t_{\alpha\beta} c^\dagger_{\alpha,\sigma} c_{\beta,\sigma} + \frac{1}{2} \sum_{\substack{\alpha\beta\gamma\delta \\ \sigma,\sigma'}} V_{\alpha\beta\gamma\delta} c^\dagger_{\alpha,\sigma} c^\dagger_{\beta,\sigma'} c_{\gamma,\sigma'} c_{\delta,\sigma}. \tag{2.101}$$

Here $t_{\alpha\beta}$ are hopping terms between two KS orbitals, and $V_{\alpha\beta\gamma\delta}$ are Coulomb matrix elements between different KS levels. We now aim to compute the energy spectrum of the system described by this Hamiltonian using the CI method. However, performing a full CI calculation is computationally demanding, as the Hilbert space grows exponentially with system size. A common strategy to address this challenge involves reducing the number of configurations and/or restricting the set of active orbitals included in the calculation, therefore the basis choice can play an important role in optimizing the number of "relevant" orbitals. In our approach, we employ both techniques to accelerate the computation while retaining the essential physics.

To reduce the number of active orbitals, we develop a projected CI procedure. We can divide the original orbital basis into two sets: frozen (F) and active (A). We can define them using a critical energy ϵ_{RB} (where RB denotes remote bands):

$$\begin{aligned} \epsilon_\alpha \leq \epsilon_{RB}, \alpha \in F \\ \epsilon_\alpha > \epsilon_{RB}, \alpha \in A. \end{aligned} \tag{2.102}$$

The value of ϵ_{RB} is determined through a convergency study. The number of necessary active states is not known apriori, and will depend on the specific system. However, we always want to limit our calculations to the smallest possible number of active states, to make the computation time shorter. We restrict our Hilbert space in such a way, that all configurations, the orbitals with energy smaller or equal to ϵ_{RB} are occupied. To derive an expression for the projected Hamiltonian, we will also rename the creation and annihilation operators in the following way:

$$c^\dagger_\alpha = \begin{cases} b^\dagger_\alpha, \alpha \in F \\ a^\dagger_\alpha, \alpha \in A \end{cases} \tag{2.103}$$

After some transformations, considering different possibilities, and removing constant terms, we can write the Hamiltonian of the active part as:

$$H_A = \sum_{\alpha\beta \in A} \left(t_{\alpha\beta} + \Sigma_{\alpha\beta}\right) a^\dagger_\alpha a_\beta + \frac{1}{2} \sum_{\alpha\beta\gamma\delta \in A} V_{\alpha\beta\gamma\delta} a^\dagger_\alpha a^\dagger_\beta a_\gamma a_\delta, \tag{2.104}$$

where $\Sigma_{\alpha\beta} = \sum_{\kappa \in F} (v_{\alpha\kappa\kappa\beta} - v_{\alpha\kappa\beta\kappa})$ is the mean field contribution from the frozen, filled states. This contribution effectively renormalizes the bare hopping terms in a manner analogous to the Hartree-Fock approach. This method allows us to choose a configuration space that is adequate to the problem considered and within the capabilities of modern computer memory.

2.5.3 Tensor Networks

TN methods, such as Matrix Product States (MPS) and Projected Entangled Pair States (PEPS), offer a powerful alternative for studying strongly correlated systems, especially when the Hilbert space becomes too large for CI methods to be practical. TN techniques offer a compact and efficient framework for representing quantum many-body states, based on the entanglement structure of the wavefunction rather than the full Hilbert space. They allow accurate approximations of ground states and low-energy excitations while dramatically reducing computational cost.

TN methods use interconnected tensors to represent quantum states, which capture the information about the entanglement in the system. This approach dramatically differs from the conventional way, where we focus on the configuration coefficients. Let us consider an example of a spin $\frac{1}{2}$ chain. A general state on the chain of length L can be written as:

$$|\psi\rangle = \sum_{\sigma_1,\sigma_2...\sigma_L} C_{\sigma_1,\sigma_2...\sigma_L} |\sigma_1, \sigma_2...\sigma_L\rangle . \tag{2.105}$$

where $C_{\vec{\sigma}_i}$ are coefficients and $\sigma_i = \uparrow$ or $\sigma_i = \downarrow$. To know this state exactly, we would need to know 2^L coefficients. Since the Hilbert space grows exponentially with the system size, storing these coefficients would soon become an impossible task, even for a modest $L = 50$, for which we would need approximately $9,000,000$ terabytes of RAM.

However, we can represent our state as an MPS instead:

$$C_{\sigma_1,\sigma_2...\sigma_L} = M^{\sigma_1} \cdot M^{\sigma_2} ... \cdot M^{\sigma_L}. \tag{2.106}$$

Here, M denotes matrices. If we restrict the maximum size of each matrix to χ, then the number of parameters required to describe a state scales approximately as $2\chi^2 L$. This represents a shift from exponential to linear growth in memory requirements—one of the key advantages of the MPS representation. The parameter χ is referred to as the bond dimension [302]. In principle, any state can be represented as an MPS, although sometimes such representation is numerically inefficient, e.g. when long-range interaction is present in the system.

The MPS representation is ideal for systems with low entanglement between subsystems A and B. To determine it, we may use the entanglement area law, which states that the entanglement entropy between A and B scales like the size of the boundary ∂A between the two regions. Low-energy states of realistic Hamiltonians are not just "any" states in the Hilbert space: they are heavily constrained by locality so that they must obey the entanglement area-law [303]. This makes it very convenient for a 1D system where the boundary between two subsystems is constant.

In practice, you can reshape the tensor $C_{\sigma_1,\sigma_2 \ldots \sigma_L}$ in Eq. 2.106 into an MPS topology using singular value decomposition and iterating over all the system sites [302]. Here we show an example of how to write the MPS for 2 electrons in 3 orbitals. A general states in this space can be written as:

$$|\psi\rangle = \psi^{011} |011\rangle + \psi^{101} |101\rangle + \psi^{110} |110\rangle . \tag{2.107}$$

Let us compare it with an equation in the form:

$$a_1 b_1 c_1 + a_2 b_2 c_2 + a_3 b_3 c_3 = \begin{pmatrix} a_1 & a_2 & a_3 \end{pmatrix} \begin{pmatrix} b_1 & & \\ & b_2 & \\ & & b_3 \end{pmatrix} \begin{pmatrix} c_1 \\ c_2 \\ c_3 \end{pmatrix} \tag{2.108}$$

Analogously, our state $|\psi\rangle$ from Eq. 2.107 can be written as:

$$|\psi\rangle = \begin{pmatrix} |0\rangle & |1\rangle & |1\rangle \end{pmatrix} \begin{pmatrix} \psi^{011} |1\rangle & & \\ & \psi^{101} |0\rangle & \\ & & \psi^{110} |1\rangle \end{pmatrix} \begin{pmatrix} |1\rangle \\ |1\rangle \\ |0\rangle \end{pmatrix} . \tag{2.109}$$

Rewriting the matrices at both edges:

$$\begin{pmatrix} |0\rangle & |1\rangle & |1\rangle \end{pmatrix} = \begin{pmatrix} |0\rangle & |1\rangle \end{pmatrix} \begin{pmatrix} 1 & 0 & 0 \\ 0 & 1 & 1 \end{pmatrix} \tag{2.110}$$

and:

$$\begin{pmatrix} |1\rangle \\ |1\rangle \\ |0\rangle \end{pmatrix} = \begin{pmatrix} 0 & 1 \\ 0 & 1 \\ 1 & 0 \end{pmatrix} \begin{pmatrix} |0\rangle \\ |1\rangle \end{pmatrix} \tag{2.111}$$

Inserting these into Eq. 2.109 we get:

$$|\psi\rangle = \begin{pmatrix} |0\rangle & |1\rangle \end{pmatrix} \begin{pmatrix} 1 & 0 & 0 \\ 0 & 1 & 1 \end{pmatrix} \begin{pmatrix} \psi^{011}|1\rangle & & \\ & \psi^{101}|0\rangle & \\ & & \psi^{110}|1\rangle \end{pmatrix} \begin{pmatrix} 0 & 1 \\ 0 & 1 \\ 1 & 0 \end{pmatrix} \begin{pmatrix} |0\rangle \\ |1\rangle \end{pmatrix}. \tag{2.112}$$

Merging the central matrices, this can be simplified to:

$$|\psi\rangle = \begin{pmatrix} |0\rangle & |1\rangle \end{pmatrix} \begin{pmatrix} 0 & \psi^{011}|1\rangle \\ \psi^{110}|1\rangle & \psi^{101}|0\rangle \end{pmatrix} \begin{pmatrix} |0\rangle \\ |1\rangle \end{pmatrix}. \tag{2.113}$$

Finally, we get:

$$|\psi\rangle = \left\{ \begin{pmatrix} 1 & 0 \end{pmatrix} |0\rangle + \begin{pmatrix} 0 & 1 \end{pmatrix} |1\rangle \right\} \left\{ \begin{pmatrix} 0 & 0 \\ 0 & \psi^{101} \end{pmatrix} |0\rangle + \begin{pmatrix} 0 & \psi^{011} \\ \psi^{110} & 0 \end{pmatrix} |1\rangle \right\} \left\{ \begin{pmatrix} 1 \\ 0 \end{pmatrix} |0\rangle + \begin{pmatrix} 0 \\ 1 \end{pmatrix} |1\rangle \right\}. \tag{2.114}$$

Here:

$$\begin{aligned} A^{\sigma_1} &= \{(1 \quad 0), (0 \quad 1)\} \\ A^{\sigma_2} &= \left\{ \begin{pmatrix} 0 & 0 \\ 0 & \psi^{101} \end{pmatrix}, \begin{pmatrix} 0 & \psi^{011} \\ \psi^{110} & 0 \end{pmatrix} \right\} \\ A^{\sigma_3} &= \left\{ \begin{pmatrix} 1 \\ 0 \end{pmatrix}, \begin{pmatrix} 0 \\ 1 \end{pmatrix} \right\}. \end{aligned} \tag{2.115}$$

We can write our initial state $|\psi\rangle$ as an MPS:

$$|\psi\rangle = \sum_{\sigma_1,\sigma_2,\sigma_3} A^{\sigma_1} A^{\sigma_2} A^{\sigma_3} |\sigma_1\sigma_2\sigma_3\rangle. \tag{2.116}$$

The MPS representation can be used in conjunction with the Density Matrix Renormalization Group (DMRG) technique to variationally find the ground state and low-lying excitations of the system. By optimizing the MPS tensors locally and sweeping back and forth along the chain, DMRG iteratively minimizes the system's energy.

Chapter 3

Magic angle twisted bilayer graphene

This chapter presents results for twisted bilayer graphene obtained using various computational methods. We start by analyzing the Hofstadter butterfly spectrum of magic-angle twisted bilayer graphene using an *ab initio*-based, multi-million-atom tight-binding model. Magnetic field effects are incorporated through Peierls substitution and Zeeman splitting. Using a nanoribbon geometry, we explore quantum size effects up to widths of 1μm, focusing both on a wide energy range and the flat band near the Fermi level. We extract the Hofstadter spectrum for sufficiently wide ribbons and identify in-gap Chern numbers by counting chiral edge states. Subsequently, we examine the Wannier diagrams to identify the insulating states at charge neutrality. We establish the presence of three types of electronic states: moiré, mixed, and conventional—each corresponding to distinct bulk and edge-state behaviours. We also examine the magnetic-field-driven evolution of moiré flatband wavefunctions, showing that electronic density decays from moiré centers with increasing flux.

Next, we study bulk MATBG, where the inclusion of the electrostatic correction induces charge redistribution at the center of the BZ and the renormalization of the band structure. We consider different possible filling factors of the flat band, starting with charge neutrality.

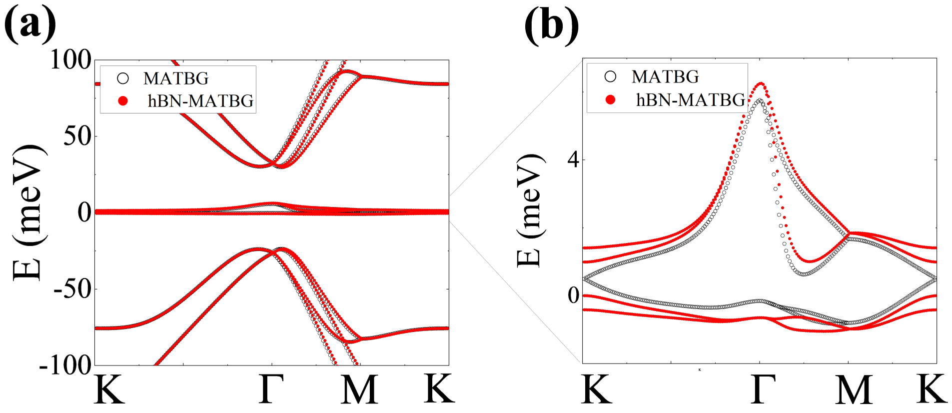

Figure 3.1: Electronic properties of moiré lattice. (a) MATBG band structure within a 200 meV energy window along the $K-\Gamma-M-K$ path. MATBG is represented by black circles, while the dispersion for MATBG on an hBN substrate is illustrated by red dots. (b) A corresponding zoom-in on the flat band.

3.1 Electronic structure of twisted bilayer graphene

We begin by analyzing bulk MATBG. Fig. 3.1 (a–b) show the band structure along the high-symmetry K–Γ–M–K path. In Fig. 3.1 (a), we focus on the energy window containing the flat band and the remote valence and conduction bands. We have obtained this band structure using the periodicity of the moiré UC - each moiré UC consists of N_{at}, and each atom repeats in the UC creating N_{at} simple Bravais sublattices. We apply periodic boundary conditions to obtain allowed wavevectors, associate a Bloch wavefunction for a given wavevector $\vec{k}$ with each atom in a moiré cell, and diagonalize the resulting Hamiltonian matrix to obtain energy bands.

In our model, we find the flat band that is 7 meV wide and separated by a 25 meV gap from the remote bands. These values are in good agreement with other tight-binding models [304] as well as with the DFT calculation [197,294,304,305]. These results are only achieved upon incorporating out-of-plane relaxation effects, which increase the band gaps and decrease the flat-band width compared to idealized, unrelaxed MATBG, see Fig. 3.2.

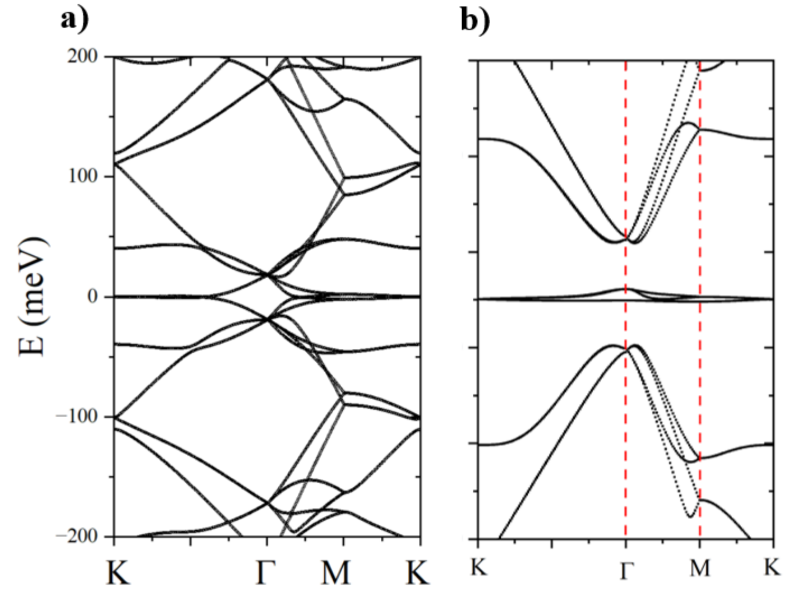

Figure 3.2: (a) Unrelaxed (b) relaxed band structure of MATBG in the vicinity of Fermi energy along the path $K - \Gamma - M - K$

Importantly, our model naturally breaks electron–hole symmetry—unlike the continuum Bistritzer–MacDonald model, where such asymmetry must be introduced manually through momentum-dependent interlayer scattering terms [306].

Fig. 3.1 also highlights the influence of an hBN substrate on the MATBG band structure, which is used to encapsulate the samples in experiments. In Fig. 3.1 (a), the black circles represent a pristine MATBG sample, while the red dots denote the system on the substrate. At higher energies, the spectrum remains largely unchanged, with the gaps between the flat and remote bands unaffected. However, the impact of the substrate becomes evident in the flat band, shown in Fig.3.1(b), where hBN induces a gap at the K-points that scales linearly with the strength of applied hBN potential. Additionally, degeneracies around K points are lifted.

3.2 Quantum size effects in the electronic structure of twisted bilayer graphene

Now we move on to the nanoribbon structure, periodic in the y-direction and finite in the x. That geometry leads to a one-dimensional BZ, and a one-dimensional momentum k_{1D}. The nanoribbon is built by stacking moiré UCs in the y-direction. The width of the nanoribbon is defined by the number of UCs stacked. We extend our analysis to widths of up to 85 UCs, which corresponds to $\sim 1\mu m$ sample sizes, that are already considered experimentally. The advantage of studying the nanoribbon geometry is that it gives us simultaneous access to realistic bulk and edge states, and the calculation is not as demanding as it would be for a finite structure of analogous dimensions. Fig. 3.3 presents the electronic structure of the MATBG nanoribbons on an hBN substrate, for different system widths. We plot here the energy sub-bands as a function of the one dimensional momentum k_{1D}. In Fig. 3.3 (a-c) bands in a 200 meV energy window are shown, while Figs. 3.3(d–f) provides a close-up view of the flat band region. The colour scale reflects the spatial localization of the wavefunctions: states localized near the ribbon edges appear in red, while bulk states near the center of the system are shown in blue. Since the spectrum is symmetric with respect to $k_{\mathrm{1D}} = 0$, we depict only half of it. Dashed lines denote the band edges inferred from the band structure of the 2D infinite system.

For the narrowest system, consisting of 5 moiré unit cells (Figs. 3.3(a), (d)), the spectrum is dominated by bulk states, and edge states are not visible due to strong hybridization with the bulk. As the system size increases, edge states become more evident, clearly visible as red lines in Fig. 3.3 (b), (e). This behaviour becomes even more evident in the widest ribbons, shown in Figs. 3.3(c), (f), where edge and bulk states are clearly distinguishable. Notably, the wave function localization for the system with 20 moiré unit cells is in good agreement with the results for 85 moiré unit cells. Given the stability of the edge state count, bulk band edges, and gap widths for systems beyond 20 unit cells, we adopt this system size for the remainder of our calculations.

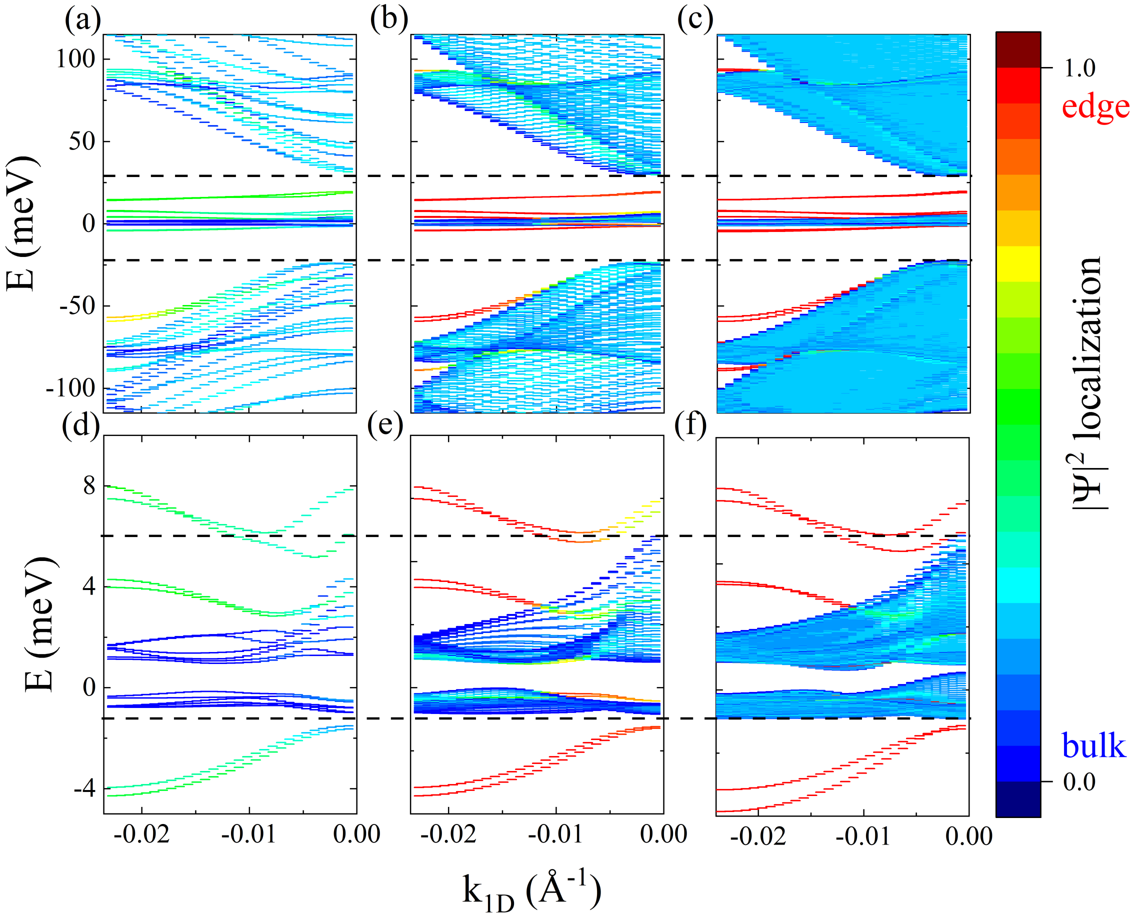

Figure 3.3: The electronic structure of the MATBG ribbon on an hBN substrate revealing quantization effects for the flat and remote bands. The figures (a-c) in the top panels show bands within a 200 meV energy window for different ribbon widths: (a) 5, (b) 20 and (c) 85 moiré unit cells. (d-f) The lower panels zoom into the flat band for analogous nanoribbon widths. Colour coding signifies the localization of states in real space. The dashed lines represent band edges deduced from the infinite system calculations.

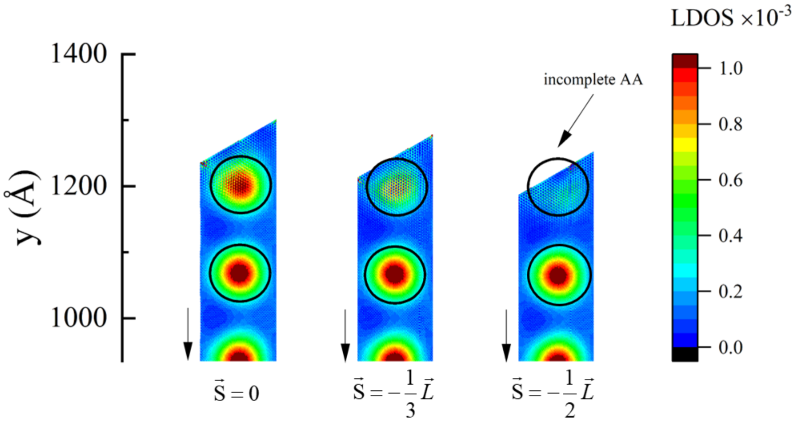

Figure 3.4: LDOS near the top edge of 20 moiré unit cell ribbons for different choices of boundary termination. Different cuts are parametrized by the shift vector S. Black circles denote the AA regions.

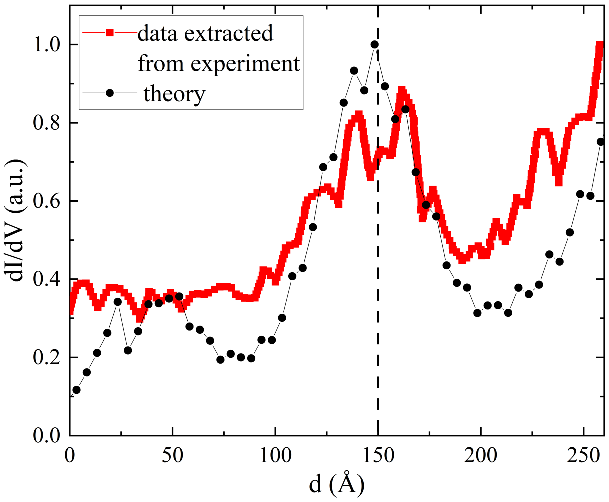

Figure 3.5: Comparison of dI/dV spectrum near the edge of the MATBG sample extracted from Ref. [1] with our spatially integrated LDOS calculation shows the effect of flat-band breakdown. Distance d is measured from the edge of the sample. The dashed line indicates the center of one of the AA regions.

We also highlight two interesting features apparent at this stage of analysis. First, a distinct band gap around $E = 0$ meV is observed in all three cases, induced by the presence of the hBN substrate. Within this gap, no edge states connect the bulk bands above and below, indicating a topologically trivial gap characterized by a Chern number $C = 0$ [307]. Second, we examine the degeneracy of the flat sub-band, which remains constant across all wave vectors k within the energy window between the remote bands. The total number of states is consistently equal to the product of the number of moiré unit cells in the nanoribbon and 8 (accounting for 2 bands, 2 valleys, and 2 spin degrees of freedom). Consequently, for each k and each spin, there are 20 states in Fig. 3.3(a), 80 in Fig. 3.3(e), and 340 in Fig. 3.3(f). This total includes both edge and bulk states, but importantly, the number of edge states remains unchanged with increasing ribbon width. This consistency suggests that the two trivial edge states located below and the four edge states above the flat band must originate from the flat band itself.

A recent experiment [1] has shown that the characteristic flat band LDOS localization around the moiré centers of the superlattice remains intact even close to the edge, as long as the sample contains a complete moiré spot. However, if the edge of the sample cuts through the AA region, the flat band LDOS will no longer be localized in that area. Our model correctly captures these features. In Fig. 3.4, we present three different ways of terminating our nanoribbon. In the first case, we preserve the whole moiré center at the edge ($\vec{S} = 0$), while in the second and third, we shift our original unit cell by a vector $\vec{S} = -1/3\vec{L}$ and $\vec{S} = -1/2\vec{L}$, respectively ($\vec{L} = \vec{L}_1 + \vec{L}_2$, see Eq. 1). One can notice that in the first case, there is a complete moiré center localized close to the edge, but for the other two choices of the edge, the LDOS fades away in that region. We have compared our results with the experimental data extracted from Ref. [1] in Fig. 3.5. Both in the experimental result and our spatially integrated LDOS result, there is a clear change in the electron density when the edge cuts through the AA moiré region. This confirms that our model is capable of capturing local physics near the edges of the MATBG system under study.

Conducting these calculations has been computationally intensive. Each nanoribbon Hamiltonian has the dimension of 11908 atoms × nanoribbon width. That means that in the largest case of 85 UC, we had to diagonalize a matrix of ~ 1 million atoms, which is not a trivial task. To manage the computational demands of diagonalizing matrices of this size, we optimized the diagonalization procedure by implementing the high-performance FEAST algorithm [308], which enhances the efficiency of eigenvalue computations within a specified energy interval. We used OpenMP parallelization within the FEAST algorithm and performed our calculations on a cluster, distributing the diagonalization across multiple cores to significantly reduce computation time. With an optimal set of parameters, we were able to reach systems consisting of approximately 1 million atoms. These calculations were performed using the resources of the Digital Alliance of Canada [309].

3.3 Moiré-Hofstadter spectrum

We now move on to including the magnetic field. To do so, we use the Peierls substitution described below.

3.3.1 Peierls substitution

For MATBG, in a nanoribbon structure, we incorporate the periodicity solely in the x-direction, modifying our Hamiltonian to have the form:

$$\hat{H}_{k_{1\mathrm{D}}} = \sum_{n,m}^{N_{\mathrm{at}}} \sum_{\sigma} c^{\dagger}_{k_{1\mathrm{D}},n,\sigma} c_{k_{1\mathrm{D}},m,\sigma} H^{nm}_{k_{1\mathrm{D}}} \tag{3.1}$$

where $k_{1\mathrm{D}} \in (-\pi/|\vec{L}_2|, \pi/|\vec{L}_2|)$ denotes the wave vector in the one dimensional BZ of the ribbon.

Thanks to the nanoribbon geometry perpendicular magnetic field can be introduced using Peierls substitution in the Landau gauge $\vec{B} = \vec{\nabla} \times \vec{A}$, with vector potential $\vec{A} = (-B_z y, 0, 0)$:

$$\tilde{t}(\vec{r}_i, \vec{r}_j) = t(\vec{r}_i, \vec{r}_j)^{B_z=0} \exp\left\{ \left(-i\pi \frac{2eB_z}{hc} \frac{(x_j - x_i)}{2} (y_i + y_j) \right) \right\}. \tag{3.2}$$

Here $hc/2e$ is the magnetic flux quantum φ_0. The Zeeman splitting is included by adding a diagonal part to our Hamiltonian in the form:

$$H_{\mathrm{Z}} = \frac{1}{2} g \mu_B B_{\mathrm{z}} \sum_n \left(c^{\dagger}_{k_{1D},n,\uparrow} c_{k_{1D},n,\uparrow} - c^{\dagger}_{k_{1D},n,\downarrow} c_{k_{1D},n,\downarrow} \right), \tag{3.3}$$

where μ_B is the Bohr magneton and g is the Landé factor. In order to use the Landau gauge, we perform a global rotation of the coordinate system, ensuring strict x-axis periodicity. Due to such periodicity, we are able to include a magnetic field in our nanoribbons without the restriction to specific magnetic flux values.

We analyze the impact of the perpendicular magnetic field on MATBG on top of hBN, focusing on various aspects of the resulting fractal spectrum. We consider magnetic fields in the range $\varphi/\varphi_0 = [0, 1]$, corresponding to approximately $B_{\mathrm{z}} \approx [0, 27]$ T. The size-dependence study under a finite magnetic field has been carried out for nanoribbons containing up to 85 moiré unit cells. As in the zero-field case ($B_z = 0$T), we find that a nanoribbon comprising 20 moiré unit cells provides a representative description of the larger structures. The computed Hofstadter spectrum is shown in Fig. 3.6, exhibiting a clear self-similar pattern of energy gaps appearing at multiple energy scales.

Since our calculations are performed for a nanoribbon geometry, the resulting spectrum includes both bulk and edge states. In Fig. 3.6, the grayscale indicates the projected density of the bulk states, while the colour scale highlights the degree of localization of the edge states. In Fig. 3.6(b), we show the fractal spectrum without the effect of the Zeeman splitting. First, we confirm that the width of the overall flat band remains constant and the flat bands do not mix with the remote bands up to one flux. From the remote bands, well-defined Landau levels (LLs) emerge for magnetic fields $B_{\mathrm{z}} < 5$ T, and their evolution as a function of B_{z} is clearly visible. Flat energy band along M-K path around 80 meV and -80 meV without a magnetic field translates into the van Hove singularities that seem to be unaffected by small magnetic fields $B_{\mathrm{z}} < 5$ T.

Importantly, we observe no edge-state crossings between the flat and remote bands, indicating that both corresponding gaps are topologically trivial with in-gap Chern numbers

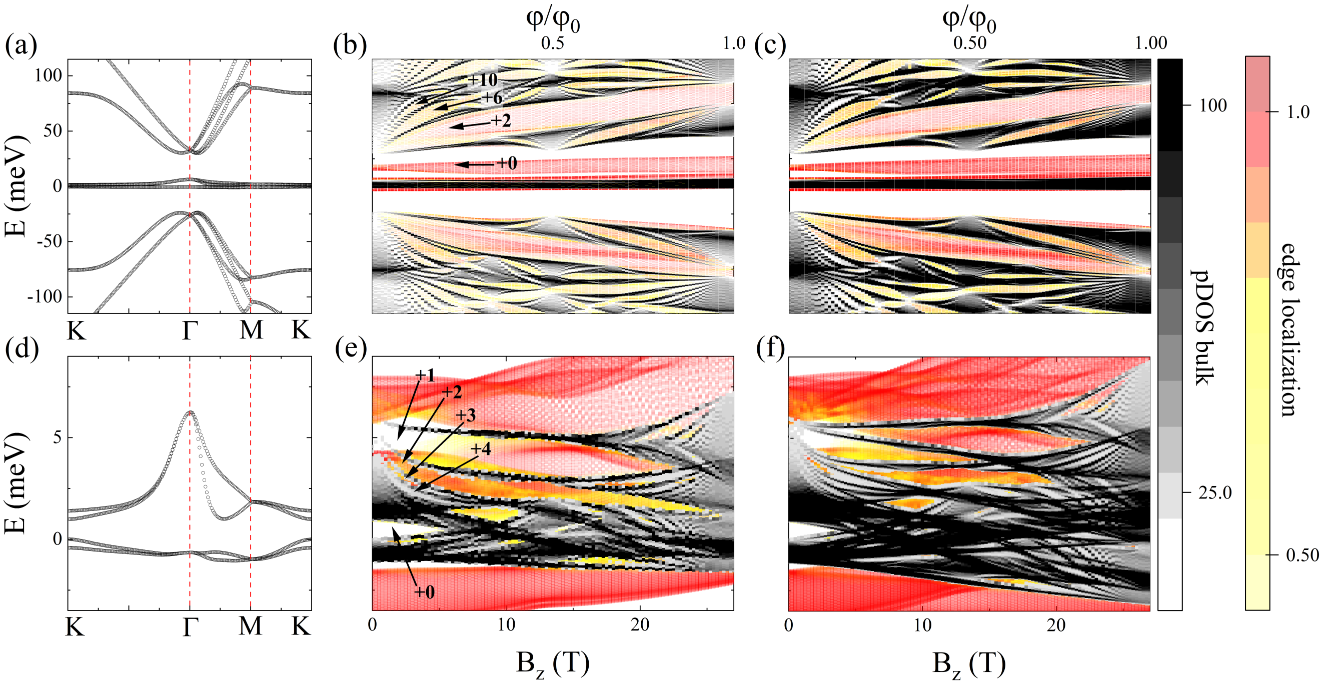

Figure 3.6: The band structure and Hofstadter spectrum of a MATBG ribbon on an hBN substrate. (a) Flat and remote bands within an approximately 200 meV energy window around the Fermi level along the $K-\Gamma-M-K$ line on the moiré Brillouin zone. (b) The Hofstadter spectrum for magnetic flux $\varphi/\varphi_0 = [0,1]$, corresponding to magnetic field $B_z \approx [0,27]$ T. This data is obtained from the nanoribbon density of states. The data points shown in greyscale represent projected density of states of the bulk, while the edge states are visualized in colour. (c) Similar Hofstadter spectrum with Zeeman splitting included. The zoom-in to the energy window $E = [-5,10]$ meV of the flat band is shown in (d-f). Arrows highlight the gaps that we characterize by the in-gap Chern numbers.

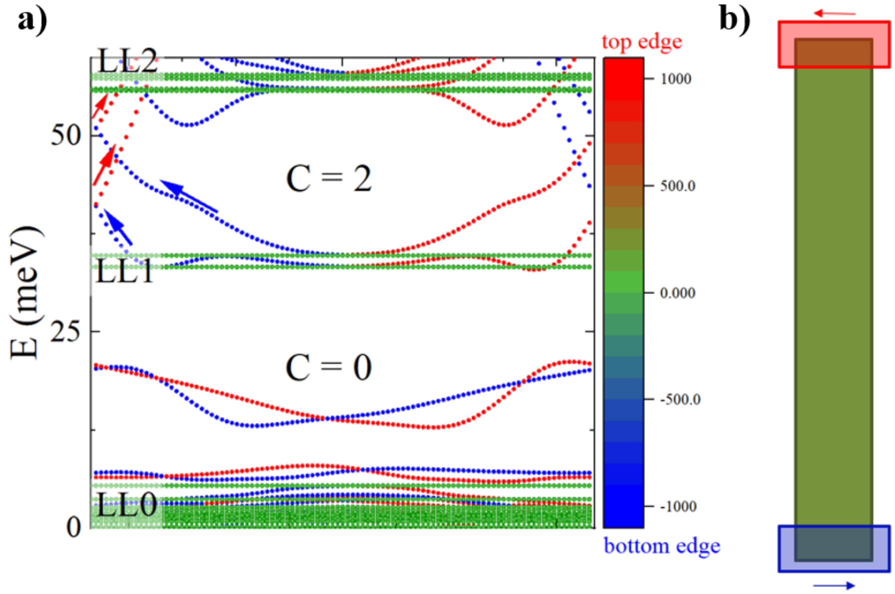

Figure 3.7: Schematic depiction of the counting the edge states procedure. (a) Zoom in on a band structure of a nanoribbon for $B_z = 4$ T. The bulk states are marked in green, and the edge states are blue and red for states running at the bottom and top of the sample, respectively. The arrows mark the evolution of a given edge state. (b) Schematic depiction of the nanoribbon with bulk and edge states marked.

$C = 0$. By analyzing the edge-state crossings between the remaining LLs, we determine the in-gap Chern numbers for these cases. The procedure is schematically shown in Fig. 3.7. The results of this edge-state counting are indicated with arrows pointing to the corresponding gaps in the spectrum.

In Fig. 3.6(c) we present an analogous spectrum including the effect of the Zeeman term

$$E = \pm\frac{1}{2} g\mu_B B_z. \tag{3.4}$$

At the energy scale considered, the only visible effect is a small broadening of the LLs, since the Zeeman splitting energy is of the order $\sim 10^{-2}$ meV/T.

In Fig. 3.6(e) and (f), we present close-up views of the Hofstadter spectra around the Fermi level, focusing on a flat band region, once again with and without the Zeeman splitting, respectively. By analyzing the edge states crossing the energy gaps, we determine the corresponding in-gap Chern numbers. The gap induced by the hBN substrate shows no edge-state crossings, confirming that it is topologically trivial with $C = 0$. In contrast, the band gaps within the split conduction band display a clear sequence of nontrivial Chern numbers: $C = 1$, followed by $C = 2$, $C = 3$, and $C = 4$.

Notably, the top of the conduction band near the Γ point has a negative effective mass. As a result, the highest Landau level originating from the flat band decreases in energy with increasing magnetic field. This tendency deepens when we incorporate the Zeeman splitting, as seen in Fig. 3.6(f). In the flat band region, the Zeeman term introduces additional energy-level splitting, leading to a noticeable broadening of the Hofstadter spectrum.

3.4 Analysis of Wannier diagrams

Through the analysis of the Hofstadter spectrum, one can extract a Wannier diagram, as described below.

Wannier diagrams provide a valuable tool to connect the Hofstadter spectrum with experimental observations [310]. These diagrams are constructed by plotting the integrated charge carrier density, up to a given energy level, as a function of the magnetic field B. This representation highlights the linear trends in energy gaps, offering an intuitive representation of electronic gap evolution in the Hofstadter-like spectrum. Importantly, this method captures both single-particle gaps and interaction-induced features such as Mott-like states.

In addition, linear fitting of the data in the Wannier diagrams helps identify "unconventional" states that cannot be explained by a simple Landau level (LL) picture or by single-particle Chern insulators. Such unconventional ground state sequences have been recently observed experimentally [2, 184] and interpreted in terms of the sequential flavour filling mechanism. Wannier plots obtained by mapping these gaps as functions of filling

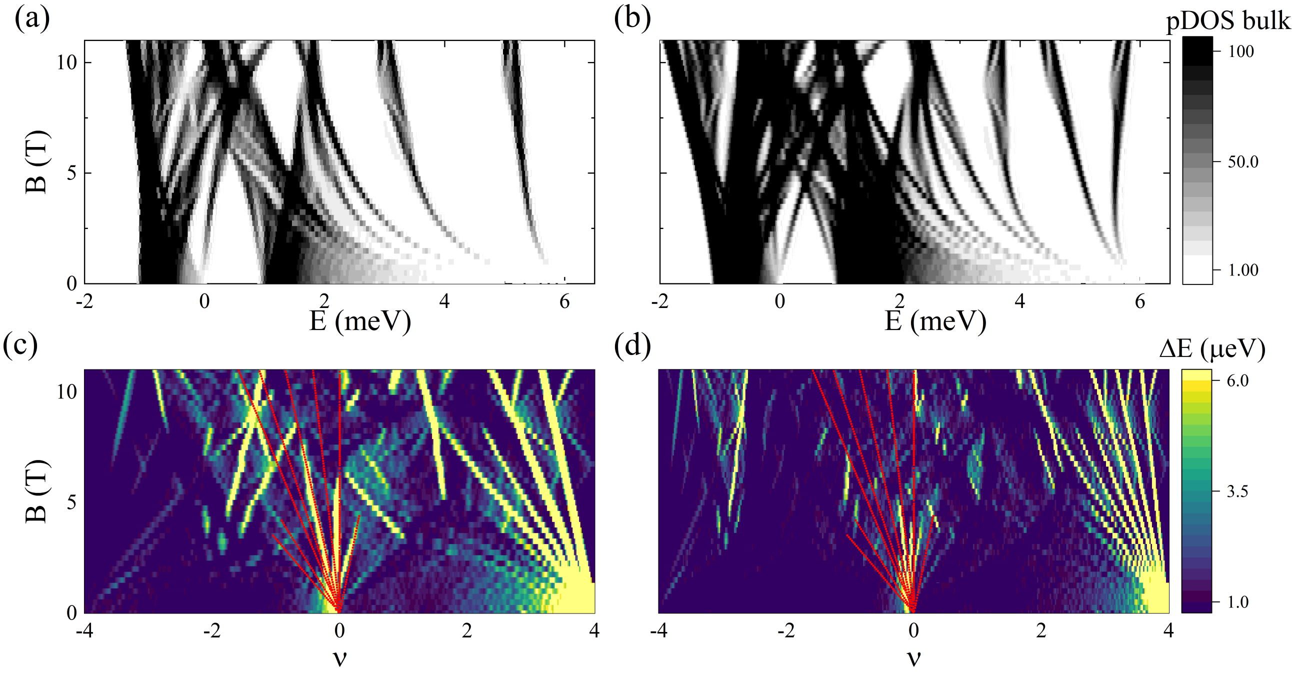

Figure 3.8: Wannier diagram of the hBN-MATBG ribbon flat band in the presence of a magnetic field. (a) Hofstadter spectrum for the bulk states of the flat band, extracted from data presented in Fig. 1 (d). (b) Hofstadter spectrum including Zeeman splitting. (c) Wannier diagram corresponding to the spectrum in panel (a). The x-axis measures the filling ν relative to the Fermi level. Filling -4 (4) indicates a completely empty (filled) flat band. The color scale is used to denote the energetic width of the band gaps ΔE. Note that all gaps larger than 6 μeV are denoted by the same colour. (d) Like (c), but this Wannier diagram is derived from the Hofstadter spectrum with Zeeman splitting included. The red dotted lines on (c) and (d) mark some of the gaps starting at $\nu = 0$ extracted from the experimental data [2]. All panels (a)-(d) have the same y-axis denoting the magnetic field $B_{\text{z}} = [0, 11]$ T.

and magnetic field provide a direct comparison with the compressibility and transport experiments [2, 86, 88, 181, 184, 206, 210, 211] and can serve as a tool for identifying (non) interacting insulating states. The incompressible states satisfy the Diophantine equation $\nu = t(\phi/\phi_0) + s$, where t is the sum of the Chern numbers of all filled bands, ϕ/ϕ_0 is the magnetic flux quanta, and s is the band filling index [184].

For clarity, we first repeat our Hofstadter spectra, choosing a smaller magnetic field range in Fig. 3.8(a-b). Note that now the magnetic field B_z is plotted on the y-axis. We focus on the flat band and extract only the bulk projected density of states. In Fig. 3.8(a) and (b), we show the Hofstadter spectra without and with the Zeeman term, respectively.

The width of the energy gaps within the flat band is depicted in color in Fig. 3.8(c-d) as a function of the filling ν and the magnetic field B_z. The red dotted lines mark some of the gaps that can be observed in the compressibility experiments ([2]). Comparing this single-particle result with the experimental data provides a direct means of identifying non-interacting, insulating states. We have achieved a good agreement with the experiment for fillings around $\nu = 0$ and low magnetic fields. This suggests a qualitatively correct mean-field, *ab initio* based tight-binding picture around charge neutrality; correlations do not play an important role here.

On the other hand, the vertical line at $\nu = 0$, corresponding to the largest electronic gap in the flat band spectrum, disappears around $B_\mathrm{z} = 5$ T in our calculations. This contrasts with experimental observations, where the gap remains open across the entire 0–11 T magnetic field range (see Fig. 2 in Ref. [2]). When the Zeeman splitting is included, as shown in Fig. 3.8(d), some of the gaps shift to odd integer fillings, resulting in better agreement with the experimental results. For instance, the gaps visible in Fig. 3.8(c) around $\nu = -2$ for $B_\mathrm{z} > 3$ T have shifted to $\nu = -3$ also for $B_\mathrm{z} > 3$ T.

However, the inclusion of Zeeman splitting also leads to a doubling of the number of gaps and a reduction in their widths, making some of the previously prominent features less distinct. For example, the rightmost gap beginning at $\nu = 0$ and closing around $B_\mathrm{z} = 5$ T is well visible in Fig. 3.8(c) in agreement with the experimental data, but becomes much less clear after including the Zeeman splitting, see Fig. 3.8(d). Hence, studying both scenarios

- with and without the Zeeman splitting - can provide valuable insights and enable us to better determine which gaps are not related to the effects of interaction.

Although a detailed treatment of electrostatic and many-body interactions is left for future work, we expect such effects to enhance the gap widths around integer fillings. Additionally, there is a very strong feature below $\nu = 4$ stemming from the well-separated top flat band LL, which is not observed in the experiments. This discrepancy suggests a strong renormalization of the band structure near the Γ point in the presence of interactions or magnetic field effects that go beyond the current single-particle picture.

3.5 Conventional, mixed and moiré state properties

Two types of bulk magnetic bands with strongly suppressed kinetic energy emerge around charge neutrality, within an energy window of approximately 100 meV. The first are the moiré flat bands, which in real space, correspond to states mostly localized in the AA stacked regions [7] of the twisted bilayers. The second are more conventional LLs, which generally extend over the entire moiré unit cell and are not confined to the 'moiré centers'. It is still unclear how these two types can be captured simultaneously in low-energy theories and how they influence each other.

Several works show different behaviours of the Hofstadter butterflies and related different Chern numbers of the gaps [27,224,241,242]. Even less is known about the microscopic structure of corresponding wavefunctions, particularly about chiral states connecting bulk bands, localized on the edges of TBG samples. A detailed understanding of these states is crucial for unravelling the topological nature of MATBG, including the role of interactions, the emergence of Chern insulating phases, possible re-entrant superconductivity, and quantum geometric effects [234,235,239,240,242,311]. In this section, we provide general microscopic features of both bulk and edge states of MATBG in a magnetic field.

It is important to experimentally probe the edge state physics, e.g. extend scanning tunneling spectroscopy studies of the breakdown of the moiré flat bands [1] to the identification of the Chern-moiré edge states, and extend transport studies of possible zero field Chern phase [73] to non-local Hall measurements and to a finite magnetic field. The local probing of competing ground-state wave functions is still in its early stages for both experimental [312] and theoretical investigations [154, 155].

Other exciting avenues for probing edge currents are superconducting quantum interferometry [313] and electron spin resonance edge probes [159, 314–316]. Although some works have discussed the moiré edge states [201, 241, 307, 317, 318], they primarily centred on the effective models or angles greater than the magic angle. Studies using large-scale atomistic tight-binding models [163, 164, 198, 319–326] have predominantly focused on the electronic structures, relaxation effects and interactions, serving as a basis for the construction of low-energy models.

Here, we investigate the microscopic properties of the MATBG wavefunctions in a magnetic field for the 20 moiré unit cells nanoribbon and a representative magnetic field $B_\mathrm{z} = 4$ T. The 1D band structure is shown in Fig. 3.9 (a-b). We consider two energy windows, with $\Delta E \approx 150$ meV in Fig. 3.9 (a), followed by a zoomed-in view of the flat band region ($\Delta E \approx 10$ meV) in Fig. 3.9 (b). In both cases, we classify the ribbon states according to their localization. States colored in green represent the ones localized within the center of the sample, while states colored in red and blue correspond to those localized on the top or bottom edges, respectively. The bulk states form flat bands, i.e. the ribbon LLs, between some of which the edge-localized states cross the gaps. This is a characteristic signature of a non-zero Chern number. We note that not all gaps are crossed by the states connecting bulk bands, suggesting the existence of trivial edge states.

Before we delve into the details of the real-space properties of the ribbon states, let us precisely define the meanings of conventional-, moiré-, and mixed-type states, classifications we use in the subsequent paragraphs. We label states as 'conventional' if the LDOS is uniformly spread over the sample and resembles a typical LL distribution. 'Moiré' states are characterized by the LDOS primarily concentrated around the moiré centers. For 'mixed' states, LDOS is neither concentrated only around the moiré centers nor uniformly spread across the sample.

To analyze the real space properties of the ribbon states, we have chosen three bulk LLs

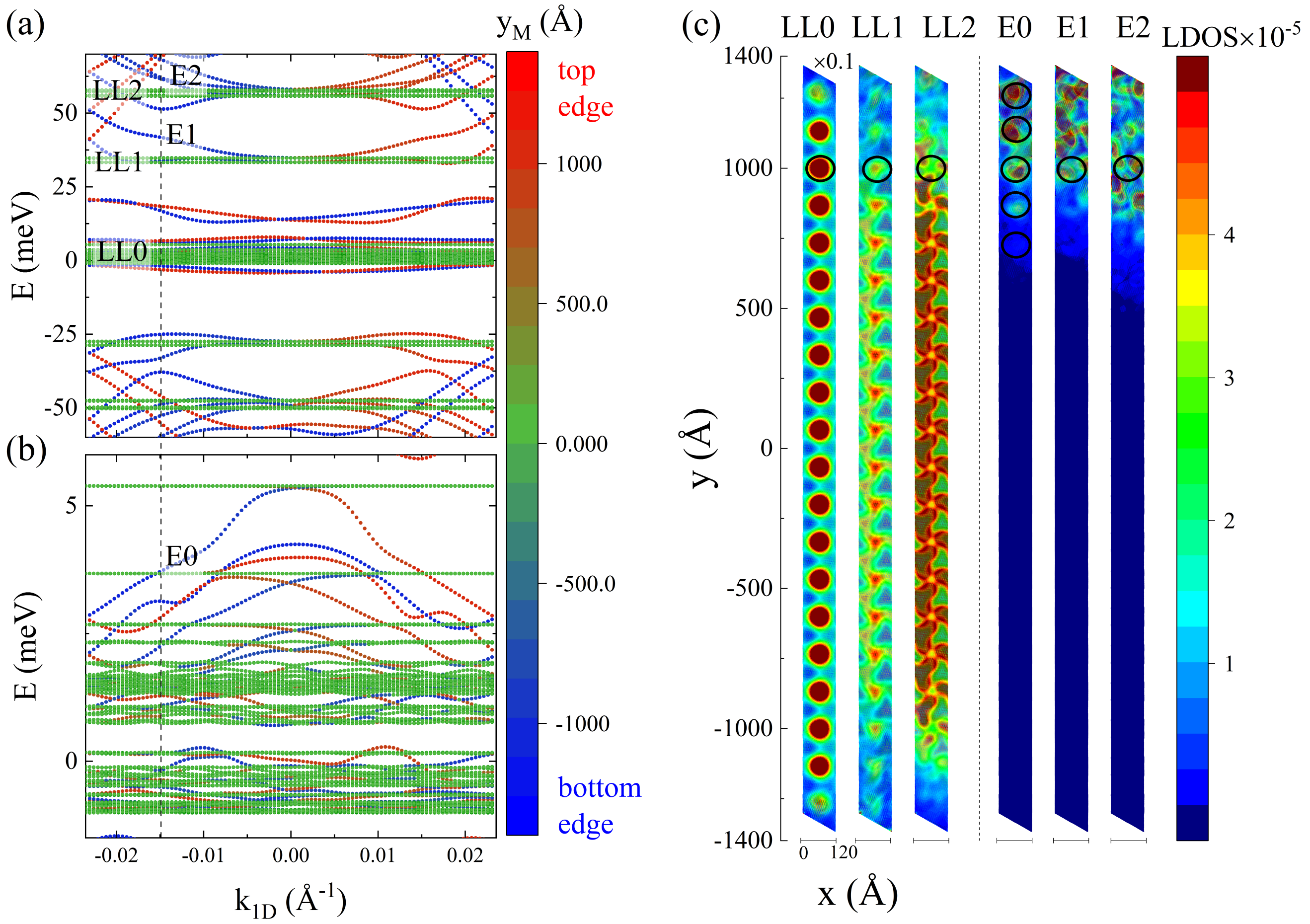

Figure 3.9: Electronic structure and wave functions of the hBN-MATBG ribbon in the magnetic field. (a) Band structure of the 20 moiré unit cells wide hBN-MATBG nanoribbon in perpendicular magnetic field $B_z = 4$ T without Zeeman splitting. Both LLs (LL0, LL1, LL2) and edge states (E1, E2) are shown. The colour scale denotes the wave function localization, with top (bottom) edge states marked by red (blue) dots. Green dots mark bulk states predominantly localized in the center of the sample. (b) Zoom in on the flat band, revealing its substructure in the magnetic field, again with the moiré edge states (E0) crossing between the moiré LLs. (c) LDOS for the bulk and edge states, which are marked on (a) and (b). The specific values of k_{1D} for which they were calculated are indicated with a black dashed line. The left side of the plot (c) shows selected bulk states – the flat band (LL0), the first LL (LL1) and the second LL (LL2). On the right, the edge states are shown - E0, which is localized within the flat band, E1, which connects LL1 and LL2, and E2, which connects LL2 with LL3 (the 3rd LL). The black circles correspond to the moiré centers, which are fixed around the AA stacked atoms in the unit cell. Note that the colour scale for LL0 is scaled by 0.1 compared to the rest of the LDOS plots in (c).

- the flat band (LL0) around $E = 0$ meV, the first LL (LL1) around $E = 30$ meV, and the second LL (LL2) around $E = 60$ meV. Our investigation of the microscopic properties of the electronic charge densities is summarized in Fig. 3.9(c), which shows the LDOS calculation and its spatial distribution. Within this analysis, we focus on three consecutive LLs, which represent three different types of bulk states. The first stripe shows the flat band, LL0, which, as expected, is a "moiré" type state - the LDOS is concentrated predominantly around the region of the AA stacking in the real space.

The second type, LL1, which is separated by a $\sim$ 30 meV gap from the flat band, still strongly feels the LL0 influence, and also exhibits LDOS concentration around the moiré centers. This result is surprising, since LL1 is a regular LL and, in principle, should present a uniform spread of the wave function. The fact that it doesn't suggests a stronger influence from the flat band than anticipated, potentially observable in a broader energy range. This is an example of a "mixed" state. Moving to LL2, the "conventional" bulk state, we observe a more uniform LDOS spread, as one would expect. However, there is also an opposite trend present - LDOS avoids the moiré centers, notice yellow dots in the center of moiré unit cells for LL2 in Fig. 3.9(c). For higher LLs, the pattern is similar to that of LL2, with an even more evenly distributed wave function.

A similar analysis can be conducted for the edge states. Once again, we identify three distinct types of edge states. Those states are indicated in Fig. 3.9(a) and 3.9(b) by: E0, which resides within the flat band; E1 connecting LL1 with LL2; and E2 linking LL2 with higher-lying LL3. The right side of Fig. 3.9(c) shows the localization of the wave function for these three cases, and in particular, its relation to the moiré centers marked with black circles. E0 is predominantly localized within the moiré centers close to the edge of the sample, and the trivial edge states in the energy gap between LL0 and LL1 around $E = 25$ meV behave in a similar manner. In the case of E1, the AA stacking localization can still be spotted, although the effect is less prominent. As for E2, there is no correspondence between the wave function localization and the moiré centers position. This is to be expected, since this state is separated by over 50 meV from the flat band, and moiré potential does not play a role here.

3.6 Evolution of the microscopic wave function's properties

We now turn to the analysis of how the LDOS changes in response to the magnetic field. For concreteness, we define a moiré center as the region within the dashed circle marked in Fig. 3.10(a). This figure shows that there are strong differences between LL0, LL1, and LL2, and those three states should be easily distinguished in scanning tunnelling spectroscopy type experiments. We investigate how much of the wave function is localized within the moiré center, and how this distribution evolves with an increasing magnetic field. The outcomes of this calculation are presented in Fig. 3.10(b), where we quantitatively compare the wave function localization for LL0, LL1, and LL2. We also show that in the flat band case, as the magnetic field increases, the wave function flows out of the moiré center and distributes more evenly over the sample, as the effect of the magnetic field becomes dominant over the effect of the moiré potential. Therefore, one can observe the decreasing character of the red line in Fig. 3.10(b). In the case of LL1 and LL2, denoted by green and blue lines respectively, there is a similar trend present, however, it cannot be observed for a larger range of B_{z}, since with the increase of the magnetic field these LLs are not unequivocally defined.

We have also focused on the moiré center nearest to the edge of the sample, as depicted in Fig. 3.10(c). Here, we investigate how much of the wave function localizes in the immediate vicinity of this center as a function of the wave vector k_{1D}. These findings are summarized in Fig. 3.10(d), where a clear distinction between E0, E1 and E2 is shown. This observation reinforces our classification of the three types of edge states. The evolution of these edge states as a function of k_{1D} looks nontrivial and warrants a more extensive study in the future. Their behaviour as a function of k_{1D} is characterized by qualitative differences, with E0 exhibiting a local minimum, E1 decaying exponentially, while E2 remaining mostly flat. These features could potentially be verified by experiments.

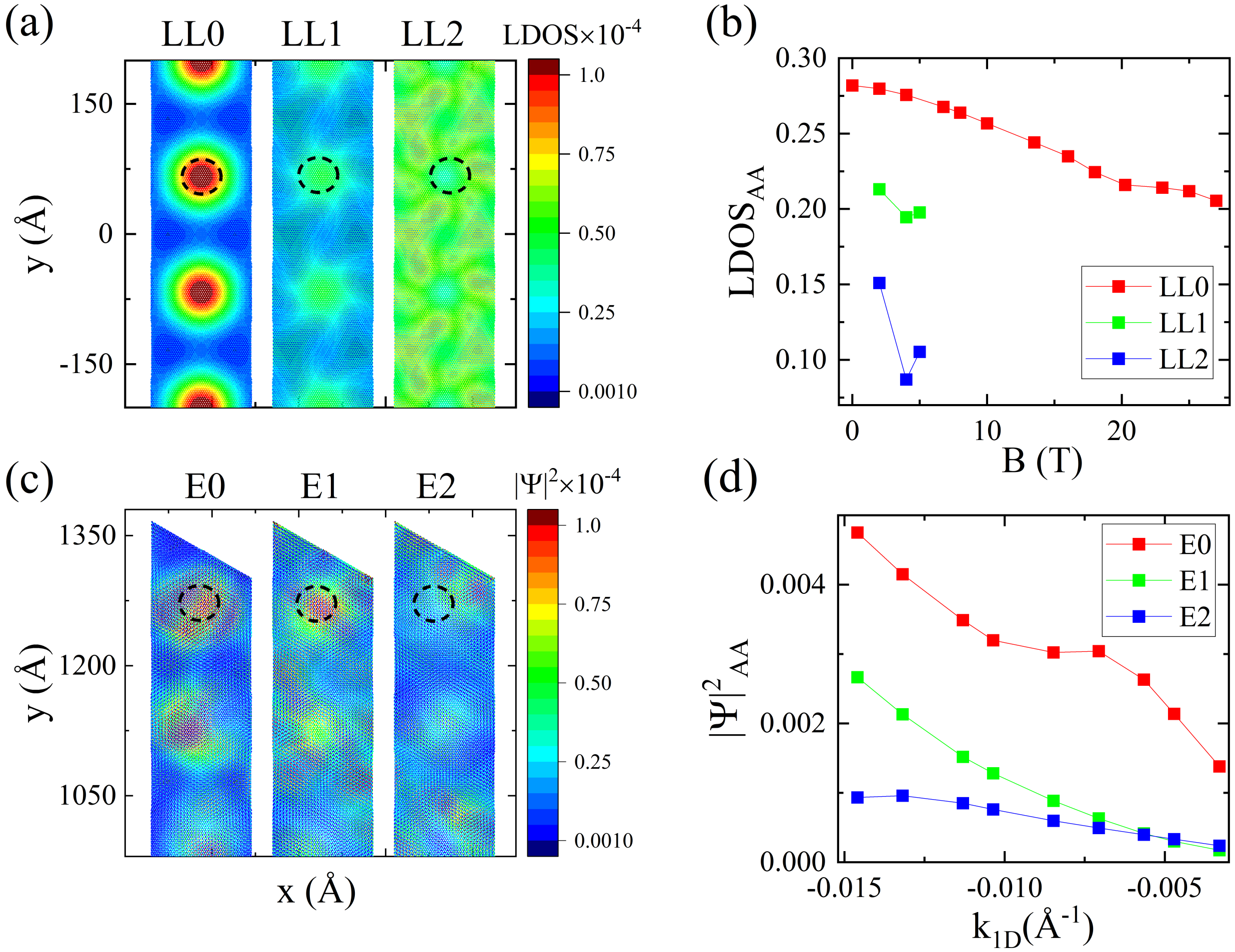

Figure 3.10: LDOS within moiré AA centers for bulk and edge states in a magnetic field for an hBN-MATBG ribbon. (a) Real-space distribution of LDOS for selected bulk LLs (LL0-LL2) shown around the center of the sample for $B_z = 4$T. (b) Corresponding integrated LDOS calculated for the moiré center defined as the region within a black circle centred around AA stacked atoms with the radius $r = 25$ Å. (c) Wave function density $|\Psi|^2$ plot of selected edge states, from left: E0, which lies within the flat band, E1 connecting LL1 and LL2, and E2, linking LL2 with LL3. (d) Similar to (b), $|\Psi|^2$ analysis, with integrated density calculated for the moiré center closest to the edge of the ribbon.

3.7 Interactions in twisted bilayer graphene

In the next step of our analysis of MATBG, we consider how the electrostatic Hartree correction renormalizes the band structure of a bulk system. We carry out the calculation for the Hamiltonian 2.81:

$$H = \sum_{\substack{i,j,\sigma \\ i \neq j}} t'_{ij} c^{\dagger}_{i,\sigma} c_{j,\sigma} + \sum_{i} \hat{n}_i \sum_{j} \left(\langle ij | V | ji \rangle \right) \left(\langle \hat{n}_j \rangle - \langle \hat{n}^0_j \rangle \right) \tag{3.5}$$

Here, $\langle \hat{n}^0_j \rangle$ is a reference density, obtained from monolayer graphene and equal to 1. It is the mean-field correction that ensures we are not double-counting interactions. $\langle \hat{n}_j \rangle$ is the electron density we are looking for, for which we solve this equation self-consistently. In order to obtain the band structure of this system, we perform a similar transformation as described in Sec. 2.3.1 and conduct our calculations in the reciprocal space.

To obtain converged results, we used a Monkhorst-Pack grid in k-space with a minimum of 64 k-points, diagonalizing the Hamiltonian H at each point. The resulting eigenvectors were then used to compute the system's probability density, which served as the input for the next iteration of the Hartree-Fock procedure. This iterative process continued until the desired tolerance between the input and output densities was achieved.

At each iteration, we had to diagonalize 64 matrices of size 12000×12000, with convergence typically requiring between 50 to 200 iterations. To optimize the computational efficiency, we implemented a hybrid parallelization scheme combining MPI (for distributed memory) and OpenMP (for shared memory). Specifically, MPI was used to simultaneously diagonalize H at each k-point across separate cluster nodes, while OpenMP allowed for the use of all available cores within each node during the diagonalization.

Following Ref. [322], we take the screened Coulomb interaction to be:

$$V_{ij} = \langle ij | V | ji \rangle = \frac{1.438}{0.116 + |\vec{r}_i - \vec{r}_j|} eV \tag{3.6}$$

where the distance between two carbon atoms $|\vec{r}_i - \vec{r}_j|$ should be given in nm. This form is

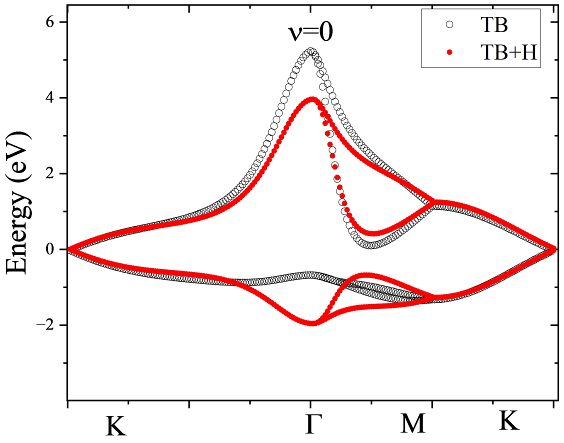

Figure 3.11: MATBG band structure obtained using a tight-binding model (black circles) compared with a model including Hartree correction (red dots) on a path $K - \Gamma - M - K$ in the moiré BZ.

an interpolated solution between unscreened Coulomb repulsion at large distances $\frac{e^2}{|\vec{r}|}$ and on-site repulsion at $V(0) = 12.4$ eV for monolayer graphene. After conducting convergence studies, we have determined that taking 24 neighbouring moiré UCs is sufficient to capture the converged result. Including more neighbours has a negligible effect on the resulting density.

We first focus on how the Hartree correction affects a charge-neutral system. Fig. 3.11 shows the renormalization of the flat bands induced by introducing the Hartree correction. While the band structure near the K points remains largely unchanged, significant renormalization is observed around the Γ point. In this region, the bands recover a greater degree of particle-hole symmetry, although the overall width of the flat band remains unchanged.

Fig. 3.12 shows the deviation of the electron charge distribution from the average $\delta n_i = n_i - \bar{n}$ as a function of the distance to the AA center of the unit cell. $\bar{n}$ here is the average electron density. One can notice that even for the non-interacting case, there is a strong charge inhomogeneity throughout the unit cell. The charge accumulates largely

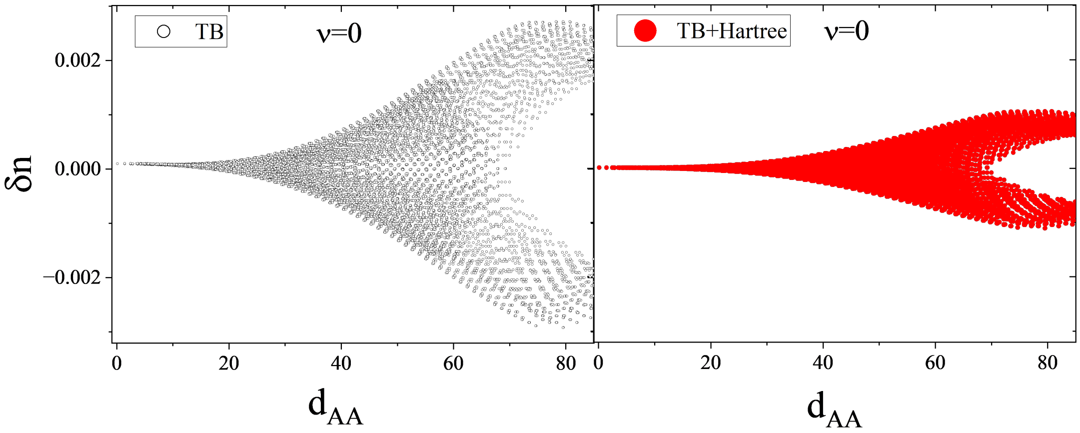

Figure 3.12: The relative electron charge distribution δ_n as a function of the distance from the moiré UC center - the AA stacked atoms for a tight-binding model (black circles) and a tight-binding model with a Hartree correction (red dots).

away from the unit cell center, around the AB/BA stacked regions. This trend prevails after including the Hartree correction, but the charge is smoothed out throughout the unit cell. The charge redistribution influences the shapes of the bands, as we have already seen in Fig. 3.11. We now turn to the analysis of the band structure at various filling factors ν, ranging from the $\nu = -3$ to $\nu = 3$ flat band. ν is here the filling factor of the flat band - we have two bands per spin, per valley, therefore a fully filled band can host 8 electrons and is denoted by $\nu = 4$. The charge neutral case, with 4 electrons is denoted by $\nu = 0$, while an empty band with no electrons by $\nu = -4$. The results of our self-consistent calculations are presented in Fig. 3.13, with the top panel showing electron doping and the bottom panel showing hole doping. Notably, the two cases exhibit a high degree of symmetry: under electron doping, the bands bend downward, while under hole doping, they arch in the opposite direction. As the magnitude of doping increases, the curvature becomes more pronounced and the flat band broadens—from approximately 8 meV at charge neutrality to around 20 meV at $\nu = \pm 3$.

Interestingly, in all cases, no band gap opens. In MATBG, two well-known mechanisms

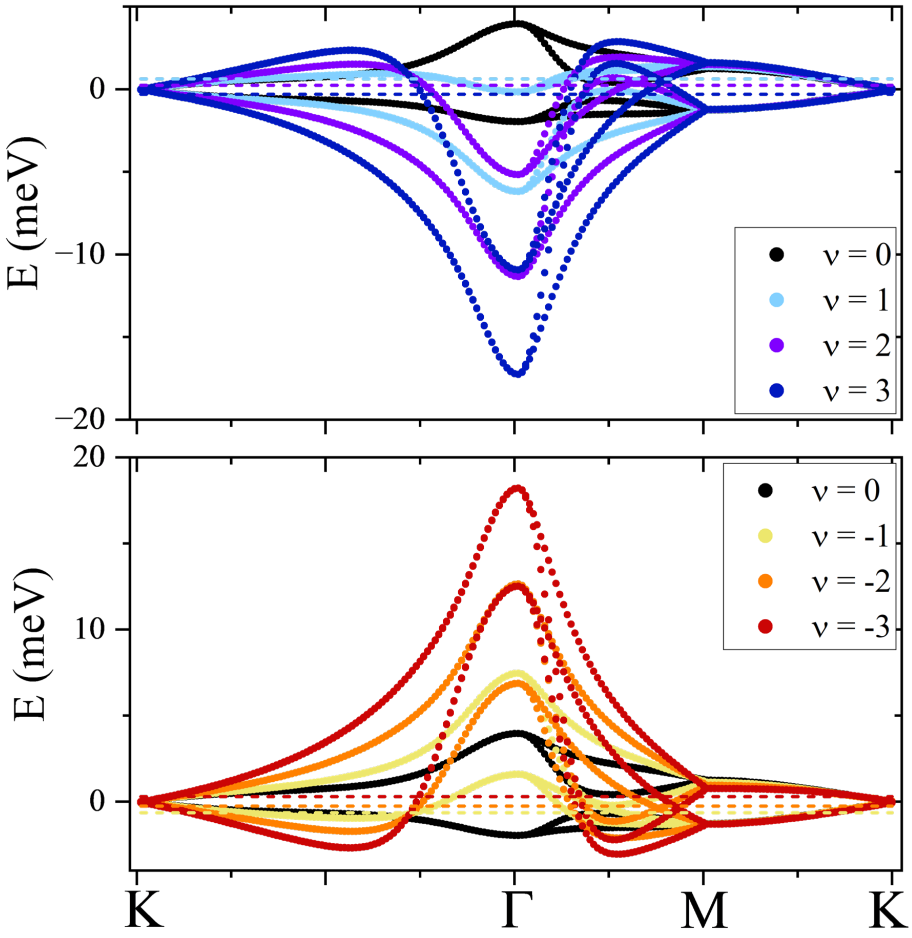

Figure 3.13: Band structure renormalization for different filling factors ν after including the Hartree correction. The top panel shows positive doping, the bottom shows negative.

can lead to band gap opening: electron-electron interactions and a staggered sublattice potential, such as that induced by a hBN substrate. The electrostatic Hartree correction alone is insufficient to open a gap. Therefore, in the following chapter, we investigate the role of on-site Hubbard interactions and the influence of an hBN substrate.

3.8 Conclusions

In this part of the thesis, we have analyzed the microscopic properties of magic-angle twisted bilayer graphene in nanoribbon geometry on top of a hexagonal boron nitride substrate with an applied magnetic field. We have studied realistic sample sizes consisting of up to 1 million atoms (85 moiré unit cells) and have established that much smaller systems (20 moiré unit cells) correctly capture the electronic properties of these structures, especially the lack of hybridization between the edge and bulk wavefunctions. For these ribbons, we have obtained the Hofstadter spectrum and determined the in-gap Chern numbers through edge states counting. We also obtained a corresponding Wannier diagram for low magnetic fields and used it to identify noninteracting, insulating states, finding a qualitative agreement with the experiments. We also determined the existence of three types of bulk and edge states, namely moiré, mixed and conventional. We have examined their evolution as a function of the magnetic field and the wave vector.

In the second part of this chapter, we have considered how including the electrostatic, Hartree correction changes the band structure of the magic angle twisted bilayer graphene system. We have observed a significant renormalization of the band structure and smoothening of the electron charge throughout the moiré unit cell. We studied different possible filling factors of the flat band and observed a high degree of symmetry between the electron and hole doping. However, the Hartree correction alone is insufficient to open a gap in the spectrum, which is why in the next step of the analysis, we include the Hubbard term and consider the presence of hexagonal boron nitride.

Chapter 4

Mirror-symmetric twisted trilayer graphene

In this chapter, we investigate mirror-symmetric magic-angle twisted trilayer graphene using a Hubbard model with long-range hopping. Solving the mean-field equations yields a band structure with flat bands and a Dirac cone. At charge neutrality, electron-electron interactions drive a metal-to-antiferromagnetic transition at relatively low interaction strength. We assess the stability of the antiferromagnetic phase against symmetry breaking due to hexagonal boron nitride encapsulation and perpendicular electric fields. Additionally, we uncover topological features in the system's multiband Berry curvature, despite the flat bands having zero Chern number. We propose a method to tune this underlying quantum geometry, offering a route to control the system's topological properties.

Figures 4.1(a–c) illustrate the geometry of our setup: the structure consists of top and bottom layers in AA stacking, with the middle layer in AB stacking and twisted by an angle $\theta = 1.55^\circ$. The TTG is encapsulated in aligned hBN, and a vertical electric field is applied. Further details are provided in the Section 2.1. Since we consider a commensurate twist angle—resulting in a periodic crystal structure—we can define a finite moiré UC as depicted in Fig. 4.1(b) and a corresponding moiré BZ, see Fig. 4.1(d).

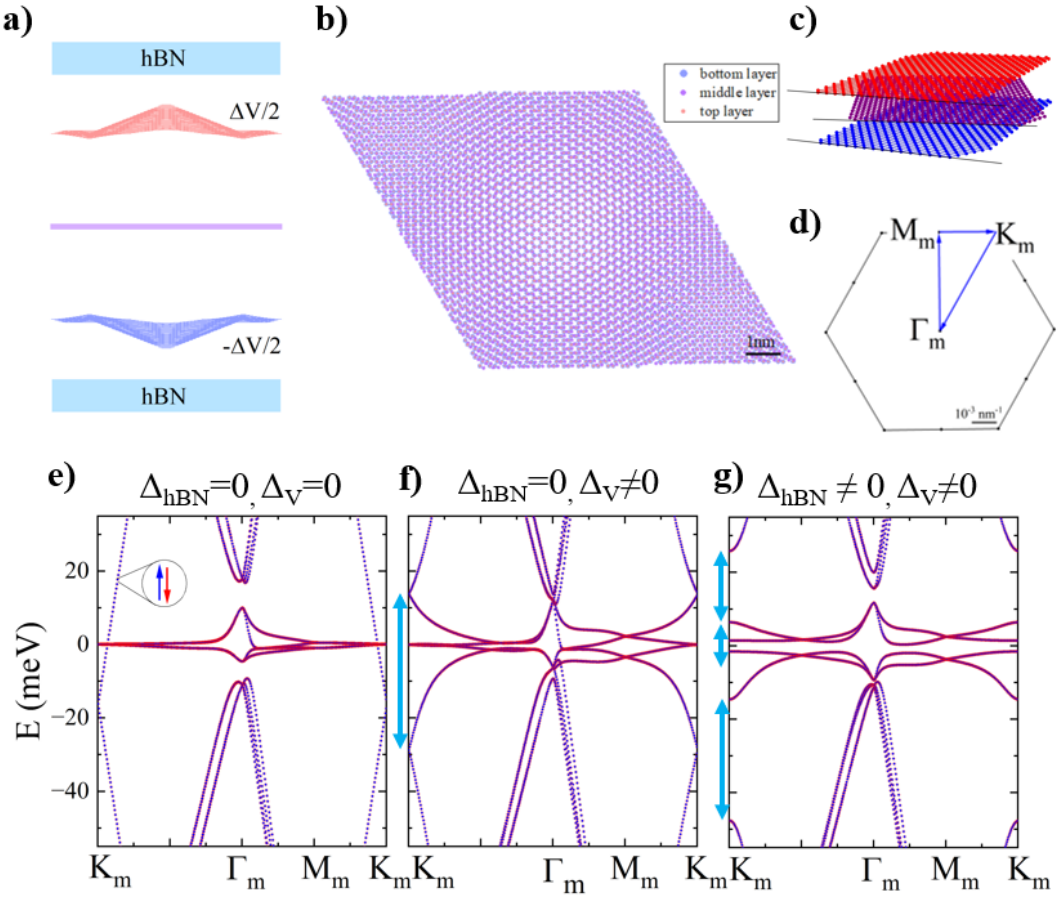

Figure 4.1: Structural and electronic properties of TTG. (a) Side, (b) top, and (c) 3D view of geometry. TTG consists of three layers of graphene, with the middle one twisted by θ, with respect to the aligned top and bottom layers, which are relaxed out-of-plane. The system is encapsulated in aligned hBN, and a vertical electric field is applied. (d) mBZ with high symmetry points. (e) Band structure of pristine TTG. (f) Effect of non-zero electric field ($\Delta_V = 120$ meV) hybridizing Dirac cones with the flat band. (g) The combined effect of electric field and hBN encapsulation ($\Delta_V = 120\text{meV}, \Delta_{\text{hBN}} = 25\text{meV}$), opening extra gaps near the Fermi level. The gaps opened by applying an electric field and hBN are marked with blue arrows.

4.1 Paramagnetic ground state, electric field- and hBN-induced gaps

The single-particle Hamiltonian for twisted graphene multilayers is given by Eq. 2.22, where hopping between p_z orbitals in three layers can be modelled as Eq. 2.23. We account for the electron-electron interactions through the Hubbard term, and our Hamiltonian becomes Eq. 2.84. We obtain the ground state of this system in the Hartree-Fock mean-field approximation as shown in Eq. 2.85:

$$H_{HF} = \sum_{\substack{i,j,\sigma \\ i \neq j}} t_{ij} c^{\dagger}_{i,\sigma} c_{j,\sigma} + U \sum_{i} \hat{n}_{i\uparrow} \langle \hat{n}_{i\downarrow} \rangle + \hat{n}_{i\downarrow} \langle \hat{n}_{i\uparrow} \rangle . \tag{4.1}$$

To study the magnetic properties of this ground state, we define the total, absolute magnetization in the units of Bohr magneton μ_B as:

$$M = \sum_{i}^{N_{\text{at}}} |m_{z,i}| = \sum_{i}^{N_{\text{at}}} \frac{|\langle \hat{n}_{i\uparrow} \rangle - \langle \hat{n}_{i\downarrow} \rangle|}{2} \tag{4.2}$$

where $m_{z,i}$ is the site magnetization. Again, we transform our Hamiltonian as outlined in Sec. 2.3.1, so that the following calculation is conducted in reciprocal space.

We proceed with a numerical analysis using a self-consistent Hartree-Fock method. The calculation is performed over an 8×8 grid in momentum space, iterating until the difference between the input and output densities falls below 10^{-8}. We test multiple initial guesses, some of which exploit the system's symmetry, while some are generated randomly. In all cases, the algorithm converges to qualitatively the same density profile, independent of the initial condition. The number of iterations required for convergence ranges from 50 to 200, depending on the interaction strength.

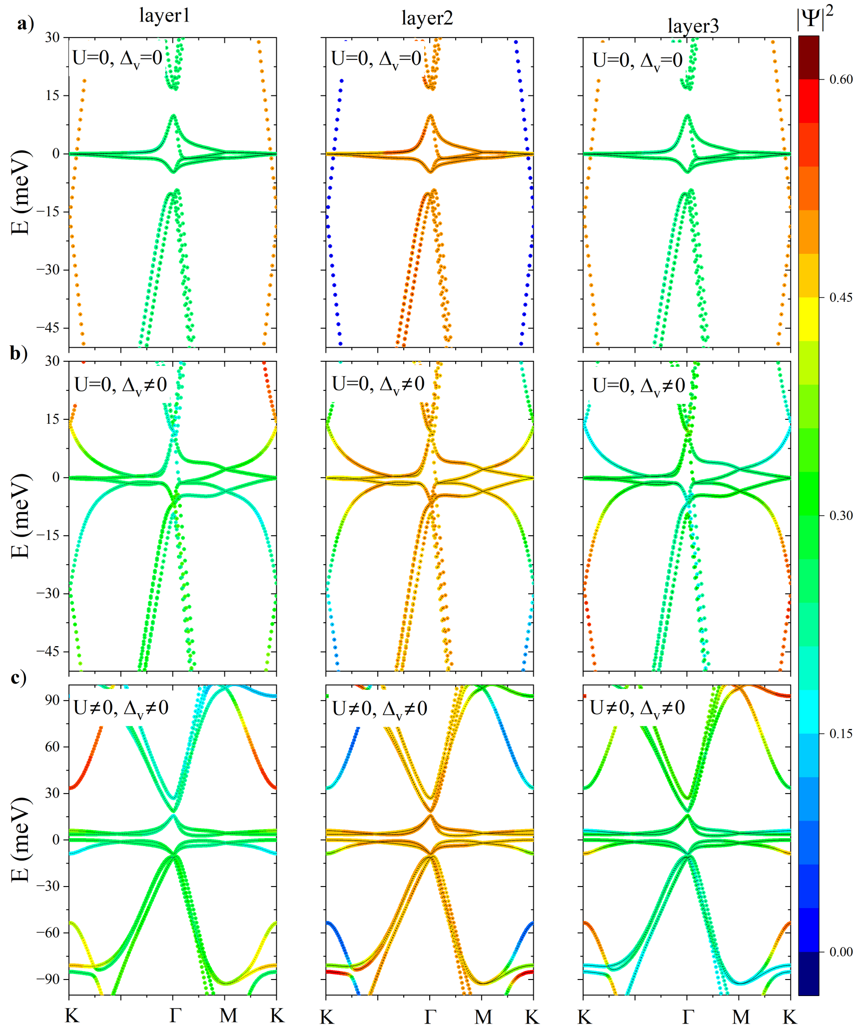

Figure 4.2: Layer-resolved wave function localization of Bloch states: a) Non-interacting TTG, (b) non-interacting TTG with applied electric field, (c) interacting TTG with applied electric field. The colour scale shows the localization of the wave function $|\Psi|^2$ in layer 1 (left panels), layer 2 (middle panels) and layer 3 (right panels). In the case of (a) mirror symmetry is preserved and the wave function is equally distributed between the top and bottom layer. The wave functions of the Dirac cones are localized solely on the top and bottom layers, while the flat band's wave functions are localized 50% on the middle layer and 25% on the top and bottom. (b) Applying an electric field breaks the mirror symmetry, and the wave function distribution is no longer equal between the top and bottom layers. (c) Including interactions further renormalizes this distribution; however, one can still notice the clear trend of the majority of the Dirac cone's wave function being localized in the top and bottom layers, and the flat band wave function being localized predominantly in the middle layer.

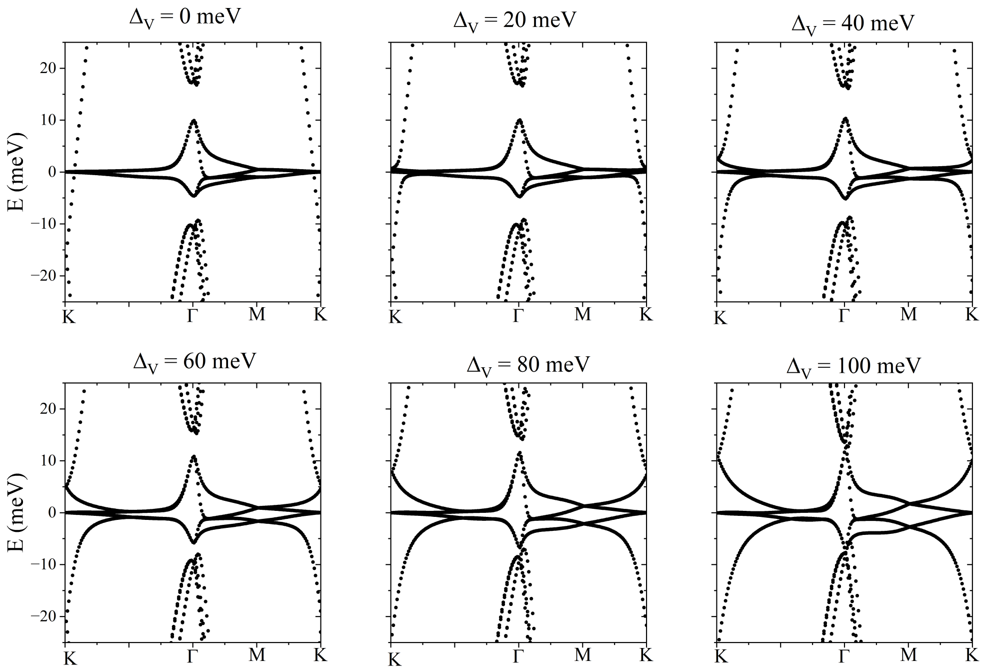

Figure 4.3: Effect of electric field: Renormalization of the non-interacting bandstructure as a function of the applied electric field Δ_V. We show here an evolution of the band gaps opening within the flat band and splitting off the Dirac cones. For Δ_V that's large enough ($\geq$ 100 meV), the gap between the flat band and the remote bands closes at the Γ point.

To begin with, we consider interaction strength $U = 0$. Fig. 4.1(e) shows the band structure for this case. The resulting ground state is paramagnetic, meaning that each atom has an equal spin up and down population (with precision of 10^{-6}). We obtain the characteristic flat band at the Fermi level with two valence and two conduction bands for each spin component. In our calculation, we also reproduce the high velocity Dirac cones at moiré K points, with Dirac points approximately 15 meV below the Fermi level. We confirm that the wave functions of these Dirac cones are localized solely on the top and bottom layers, while the flat band's wave functions are localized 50% on the middle layer and 25% on the top and bottom, see Fig. 4.2. Such localization can be explained in terms of a TTG system comprising of a monolayer graphene and TBG [245].

We now study the effect of vertical electric field and hBN encapsulation. We first

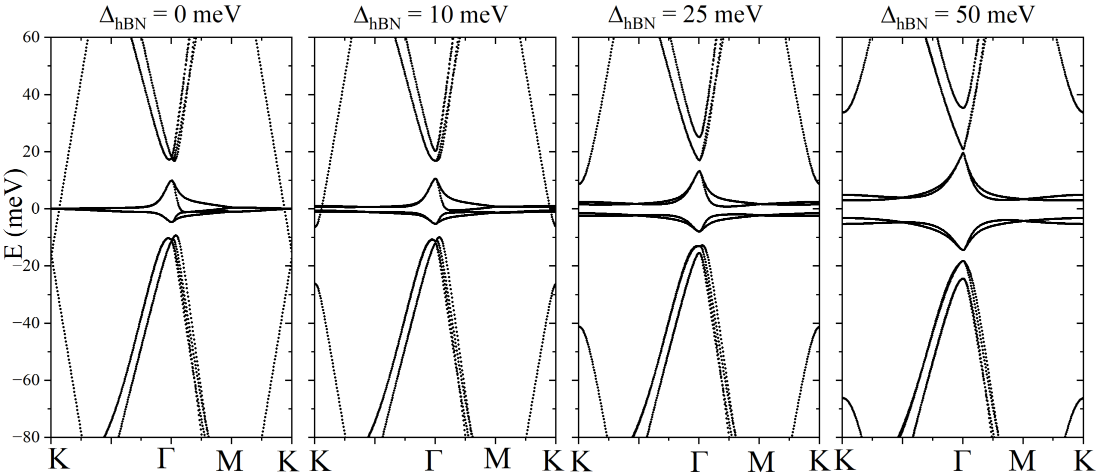

Figure 4.4: Effect of hBN: Analogous to Fig. 4.3 evolution of band structure as a function of the strength of the staggered potential Δ_{hBN} induced by an hBN substrate. Increase of Δ_{hBN} leads to a gap opening within the flat band and between the Dirac cones at K-points.

introduce a non-zero electric field ($\Delta_V = 120$ meV). Such mirror-symmetry-breaking perturbation hybridizes the Dirac cones with the flat bands [247]. This hybridization leads to splitting between the valence and conduction bands in the flat band, opening a gap at K points, shown in Fig. 4.1(f) by a blue arrow. However, the gap at the Fermi level remains closed, and, in addition, the gap between the flat band and the remote bands closes at the Γ point. The evolution of the bands as a function of the applied electric field is shown in Fig. 4.3.

In the next step, we turn on the interaction with encapsulating hBN in the form of a top and bottom layer staggered sublattice potential Fig. 4.1(g) ($\Delta_{\mathrm{hBN}} = 25$meV). This leads to the opening of the gap within the flat band. Additionally, similar to the gapped monolayer graphene case [327], a gap between the Dirac cones opens, and their dispersion becomes parabolic. The remote bands peel off from the flat band at the Γ point so that our system consists of a well-defined flat band and a gap around the Fermi energy. We note that TTG with an applied electric field and hBN is strikingly similar to the TBG/hBN structure, with an extra set of remote bands at K points originating from the gapped

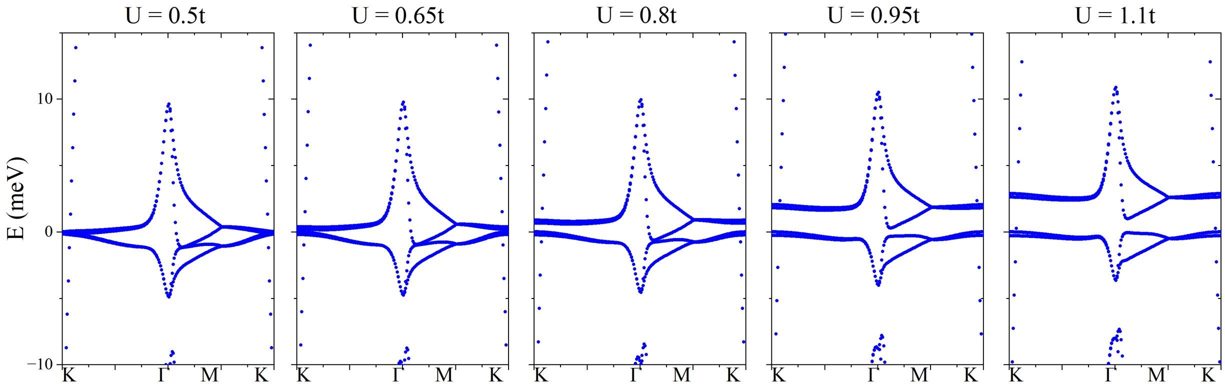

Figure 4.5: Effect of interactions: Renormalization of the mean-field band structure as a function of the interaction strength U, with $\Delta_V = 0$ and $\Delta_{\mathrm{hBN}} = 0$. As U increases, the Mott-like gap within the flat band opens, and the bands along $K - \Gamma$ and $M - K$ flatten. We observe no gap opening within high-velocity Dirac cones, therefore, no global gap is generated.

Dirac cones. We consider different strengths of hBN and present the results in Fig. 4.4. Changing the strength of hBN in an experimental setting can be achieved by applying pressure to the sample or misaligning the substrate.

4.2 Mott gap and anti-ferromagnetic transition

In the context of moiré materials, electron-electron interactions play an essential role due to the reduced bandwidth. To understand their influence, we consider different strengths of the interaction, modifying the Hubbard parameter U, see Fig. 4.5 We have tested several choices of initial input density and concluded that there is a phase transition between the non-magnetic and the AF state for the critical value of $U_c \approx 0.6t$, where $t = |\gamma_0| = 2.835$ eV is the nearest neighbor hopping. To determine the system's ground state, we analyze the total absolute magnetization, Eq. 4.2, whose value is close to zero for a paramagnetic case, and significantly larger in the AF phase.

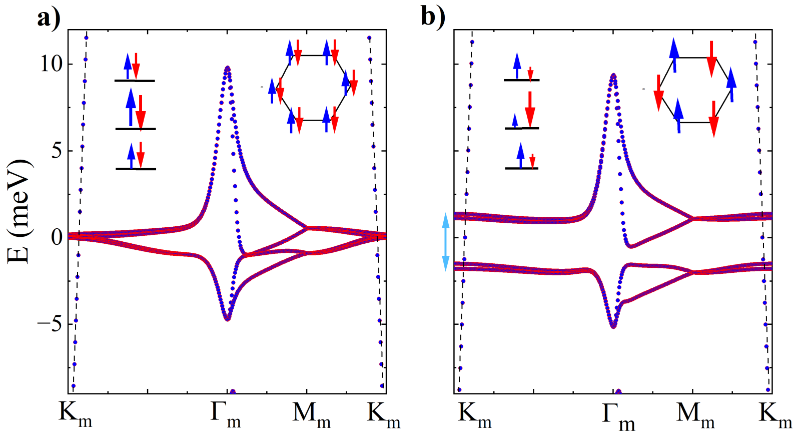

Figure 4.6: Hartree-Fock quasiparticle band structures of TTG with $\Delta_V = \Delta_{\mathrm{hBN}} = 0$. (a) Band structure in the paramagnetic state with $U = 0.5t$. The insets show a schematic depiction of the spin configuration in the three layers (left) and on the honeycomb lattice of a single layer (right). Black dashed lines were added alongside the Dirac cone dispersion to improve readability. (b) Band structure of the flat band in the anti-ferromagnetic state with $U = 1.1t$. Red and blue colours encode up and down spins, respectively.

We now show the Hartree-Fock quasiparticle bands for spin up and down obtained by self-consistently diagonalizing the Hubbard Hamiltonian, Eq. 2.85. For sufficiently small $U < U_c$, we do not observe any strong renormalization of the bands close to the Fermi level, as shown in Fig. 4.6(a). The state is paramagnetic, meaning each atom has an equal spin up and down population. On the other hand, when $U > U_c$, a transition to an AF ground state occurs. A clear Mott gap is opened in the flat band after the phase transition in Fig. 4.6(b) for $U > 1.1t$. There is no gap opening for the Dirac cones, therefore, no gap is generated at the Fermi level. The AF state has the most significant spin polarization in the middle layer, which is the layer with the highest contribution to the flat band. Bilayer graphene has smaller U_c than a monolayer, therefore the effect of U is stronger in the middle of TTG. The total spin density on A and B sublattices of graphene layer building TTG is imbalanced, producing a microscopic AF state. Such AF state is analogous to an AF state in other n-layer graphene systems [140, 328].

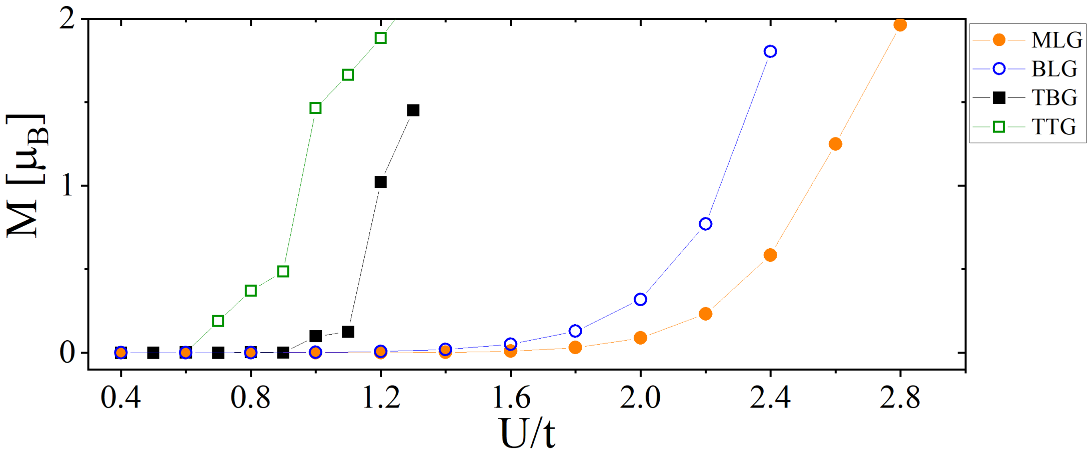

Figure 4.7: AF transition in various graphene-based systems. Total absolute magnetization of different graphene systems (MLG, BLG, TBG, TTG) in the units of Bohr magneton as a function of the interaction U scaled by the nearest-neighbour hopping t.

The Hubbard parameter U for which the para- to anti-ferro- magnetic transition occurs is lower than in the mono- and bi-layer graphene systems (Fig. 4.7). For example, it has been shown that in the monolayer graphene (MLG) in the Hartree-Fock approximation $U_c \approx 2t$ [140]. We reproduced this result in our model, with small differences caused by the long-range TB hopping necessary to model TTG correctly. Equivalent calculations for bilayer graphene (BLG) yield $U_c^{\mathrm{BLG}} < U_c^{\mathrm{MLG}}$. This stems from the fact that since the dispersion in BLG is parabolic, the density of states is increased, and the ratio of interactions to kinetic energy increases as well. It is unsurprising that TBG has a smaller critical transition parameter ($U = 1.1t$), as shown in Fig. 4.7.

Naively, one could argue that since TTG has an additional Dirac cone and a similar bandwidth of the flat bands, critical U should be larger than in TBG. Our results point out that there is actually an opposite trend with $U_c^{\mathrm{TTG}} < U_c^{\mathrm{TBG}}$. This effect is a consequence of the TTG flat band being flatter than the TBG one. Here, we refer to its pieces being effectively flatter since, at the Γ point, the flat band in TTG is actually wider (15 meV) than in TBG (8 meV). The flatter band enhances electron correlations, reducing screening

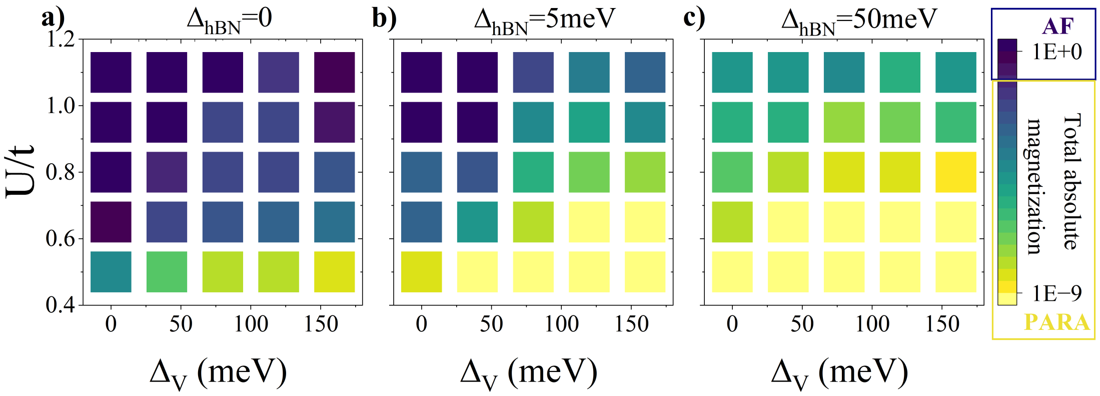

Figure 4.8: Magnetic phase diagram of TTG. (a) TTG without a substrate. AF order parameter is studied in function of interaction strength (U/t) and applied electric potential (Δ_V) (b-c) Similar phase diagram for staggered potential strengths (b) $\Delta_{hBN} = 5$ meV and (c) $\Delta_{hBN} = 50$ meV. The colour scale denotes the total absolute magnetization on a logarithmic scale.

effects and further decreasing the critical Hubbard parameters.

4.3 Magnetic phase diagram stability

We now study the combined effects of the applied electric field, hBN encapsulation, and the presence of electron-electron interactions on the ground state of charge-neutral TTG. We study the magnetic phase diagram as a function of the interaction strength and electric field for three values of the staggered potential from hBN encapsulation. Our results are summarized in Fig. 4.8. Without the A/B sublattice symmetry breaking, we observe in Fig. 4.8(a) that the critical value of U increases with increasing electric field. This follows from the fact that the applied electric field breaks the mirror symmetry of TTG and causes the system to bear more resemblance to three monolayers, for which the critical value of U/t is higher. Since in the actual device U/t is fixed, the electric field allows thus to switch the magnetic state from AF to paramagnetic for sufficiently large U/t.

When a small sublattice-breaking perturbation is included in the top and bottom layers, even though most of the electron density is in the middle layer, a strong renormalization of the phase diagram is observed. The imbalance introduced by the hBN layer directly counteracts the effects of the Hubbard term. While the Hubbard interaction penalizes the occupation of different-spin electrons on the same atom, the hBN-induced potential favours relocating electrons to sublattice B. Consequently, a larger value of U is required to overcome this preference, transfer charge from sublattice B to sublattice A, and create a polarized state. The region of stable AF state is reduced to larger values of U/t and smaller electric field; see top left of Fig. 4.8(b). Further increase of the staggered potential parameter, as in Fig. 4.8(c) to $\Delta_{\mathrm{hBN}} = 50$ meV, completely destroys the AF region in the studied range of U/t. We confirm that the AF state is susceptible to mirror and sublattice symmetry-breaking perturbations.

4.4 Multiband Berry's curvature tuning

Flat bands of twisted materials are known to realize a variety of topological phases. For example, at $\nu = -3$ filling in TBG interaction-induced Chern insulator is predicted [74]. The topological phases catalogue is still to be established in the TTG studied here. For a charge-neutral system for all studied electric fields, hBN strengths and Hubbard parameters U, flat bands near the Fermi level are always intertwined. Therefore, single-band Berry's curvature and Chern numbers are not well defined. However, multiband analogs can be defined, in our case of 2+2 bands separated from other bands by well-defined energy gaps, valid for an ample region in the parameter space of $\Delta_{\mathrm{hBN}}, \Delta_V$ and U. In Figs. 4.9 (a) and (b), we show the corresponding Hartree-Fock band structures for two representative choices of parameters.

First, we establish that the multiband Chern number $C_{1+2+3+4}$ corresponding to all four bands is 0. This is also the case for the two flat valence (VBs) and conduction bands (CBs) separately ($C_{1+2} = C_{3+4} = 0$). However, we observe a non-zero peak of mBC around K

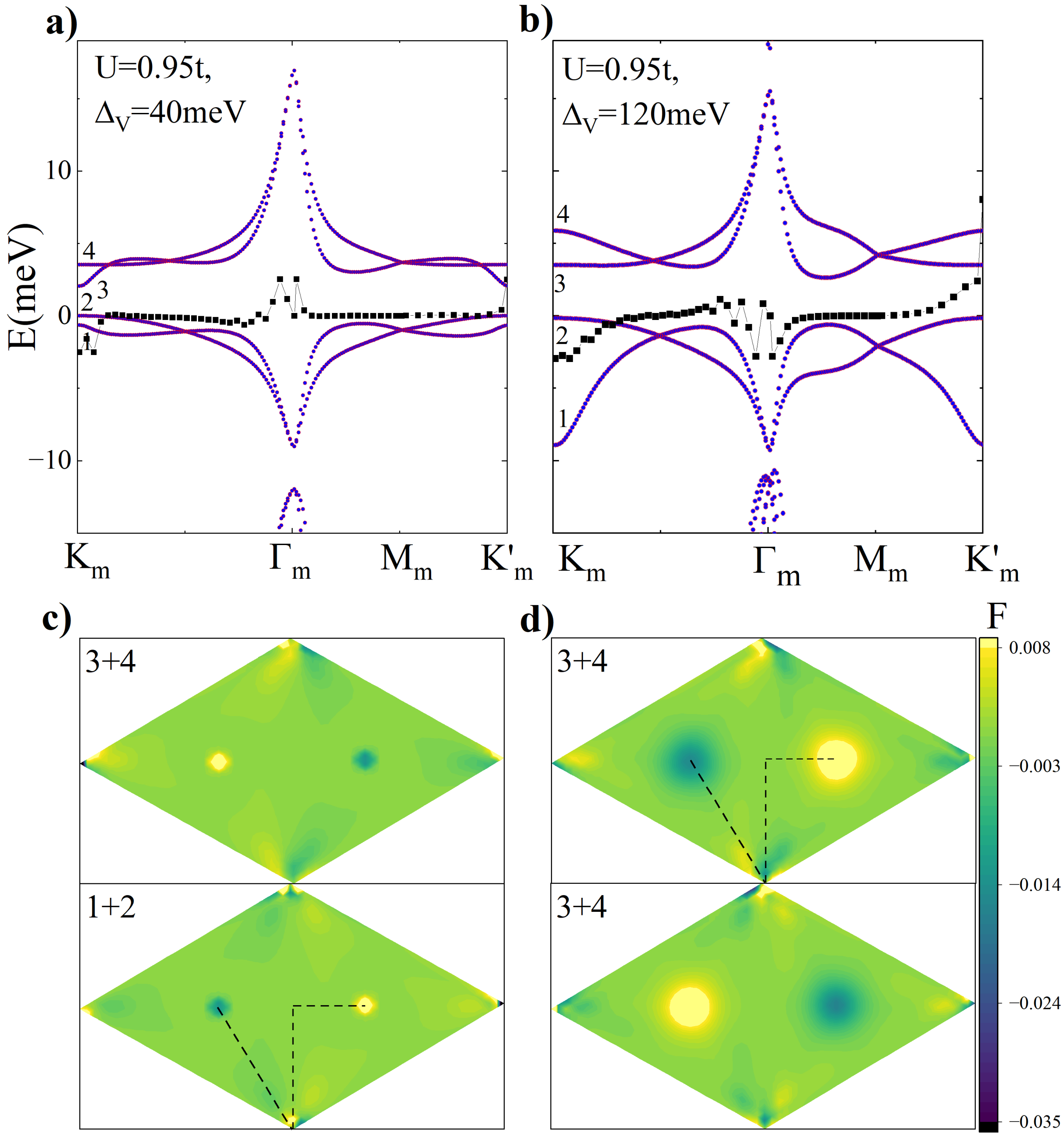

Figure 4.9: Multiband Berry's curvature in TTG. Band structure and mBC profiles along the mBZ path for both two VBs (1+2) and two CBs (3+4) for a) $\Delta_V = 40$ meV and b) $\Delta_V = 120$ meV. Distribution of mBC on whole mBZ, c) corresponding to a) and d) corresponding to b). Colour scale encodes the strength of mBC. The dashed line shows the mBZ path of a) and b).

and K' points, see e.g., Fig 4.9(c), which cancel each other out. We establish that non-zero peaks are also present around the Γ point, in Fig. 4.9(c) in the corners of rhomboidal moiré mBZ. In that sense, the geometry of wavefunctions is hidden since it produces $C = 0$ despite having a rich profile in the mBZ.

We also show that the k-space profiles of mBC can be tuned using an electric field. In Figs. 4.9(c) and (d), we compare the distribution of BC across mBZ for two values of Δ_V, keeping fixed Δ_{hBN} and U for clarity. We observe that the spread of mBC increases for larger Δ_V around K points. A less pronounced effect is observed around the Γ point. Such curvature strength tuning, combined with the selective valley population for doped systems, might be interesting from the perspective of engineering interacting states.

4.5 Conclusions

In this chapter, we study the mirror-symmetric twisted trilayer graphene, which is a highly tunable moiré system. Our calculations show that the critical value of the Hubbard parameter U necessary to observe magnetic phase transition between para- and anti-ferromagnetic states is smaller than in other graphene-based systems. However, the anti-ferromagnetic state is destabilized by mirror and sublattice symmetry-breaking perturbations induced by the applied vertical electric field and the presence of an hexagonal boron nitride substrate. Our findings highlight the intricate interplay of electric field, sublattice symmetry breaking, and electron-electron interactions in determining the magnetic and electronic properties of twisted trilayer graphene.

We note that the unrestricted Hartree-Fock method used in this work has been shown sufficient to capture the ground state properties of twisted bilayer graphene [102,104,329], with general qualitative picture unchanged when more precise treatments of correlations, i.e. exact diagonalization, density matrix renormalization group or dynamical mean-field theory, are used. Inclusion of correlations are subject of our future work.

We also establish the presence of 'hidden' quantum geometry—even though the system exhibits zero Chern numbers at charge neutrality, the profile of Berry's curvature is non-trivial. We show that it can be tuned using electric fields. This can be useful in understanding low electron/hole-doped phases, especially those in which carriers unequally populate valleys, i.e., valley-polarized states.

Chapter 5

Triangular graphene quantum dots

In this chapter, we focus on the triangular graphene quantum dots with zig-zag edges. We discuss an exact analytical solution to the zero-energy shell and show how the nitrogen impurity allows us to probe its wavefunctions. The theoretical predictions are compared with *ab-initio* calculations and with scanning tunnelling microscopy experiments. We then study triangular graphene quantum dots with armchair edges using a density functional theory + configuration interactions method. We analyze the role of the impurity on the energy spectrum and how the inclusion of excitations renormalizes the ground state energy. Finally, we focus on twisted bilayer triangular graphene quantum dots with zig-zag edges and study the behaviour of the zero energy shell as a function of size and the twist angle. In this approach we combine two mechanisms shown to lead to the formation of a zero energy shell - the sublattice imbalance arising from the triangular geometry and a zig-zag edge, and the formation of a moiré pattern.

5.1 Probing the zero energy shell wave functions of triangular graphene quantum dots using a localized impurity

Following Ref. [39], we derive here analytical expressions for wavefunctions of the degenerate zero energy shell of TGQD with zig-zag edges. We consider a TGQD of an arbitrary size, consisting of two inequivalent sublattices - A and B, depicted by red and blue dots respectively in Fig. 5.1(a) for a case of TGQD with five benzene rings on the edge, later referred to as 5-TGQD. We model this structure using the single p_z, nearest-neighbour tight-binding model. The Hamiltonian has the form 2.22, but we assume a constant t, which is a hopping integral to the nearest neighbour. The zero-energy shell consists of states with zero energy,y i.e. all states which satisfy the singular eigenvalue problem:

$$H\Psi = 0. \tag{5.1}$$

Here Ψ is the wave function of the whole system and can be written as a sum of contributions coming from both sublattices:

$$\Psi^{\alpha} = \sum_i b_i^{A,\alpha} \phi_i^{\mathrm{A}} + \sum_i b_i^{B,\alpha} \phi_i^{\mathrm{B}}. \tag{5.2}$$

Here $\phi_i^{\mathrm{A(B)}}$ refer to p_z orbitals localized on the i$^{\mathrm{th}}$ A (B) atom and coefficients b_i^{α}, to be determined, specify the eigenstate α. Let's consider an i$^{\mathrm{th}}$ B-atom and its three nearest neighbours (Fig. 5.1(b)). Using Eq. 5.1 and projecting on ϕ_i^B, we obtain:

$$\begin{aligned} b_i \left\langle \phi_i^B \right| H \left| \phi_i^B \right\rangle + b_j \left\langle \phi_i^B \right| H \left| \phi_j^A \right\rangle + b_k \left\langle \phi_i^B \right| H \left| \phi_k^A \right\rangle + \\ b_l \left\langle \phi_i^B \right| H \left| \phi_l^A \right\rangle = 0. \end{aligned} \tag{5.3}$$

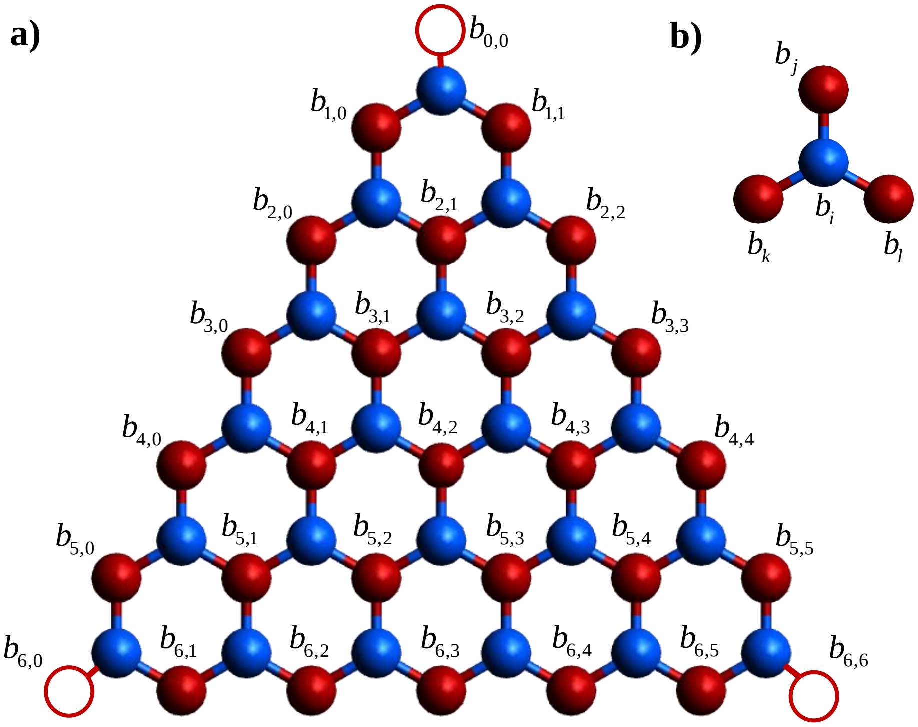

Figure 5.1: (a) Geometry of 5-TQGD structure. A-atoms are plotted as red dots, B-atoms as blue dots. Empty circles in the corners of the triangle are fictitious atoms added to ensure proper boundary conditions. All A-atoms are labelled with $b_{n,m}$ coefficients. (b) B-atom with its three nearest neighbours. All atoms are labelled with their b_i coefficients.

Using the expressions $\left\langle \phi_i^B \right| H \left| \phi_j^A \right\rangle = \left\langle \phi_i^B \right| H \left| \phi_k^A \right\rangle = \left\langle \phi_i^B \right| H \left| \phi_l^A \right\rangle = t$ and $\left\langle \phi_i^B \right| H \left| \phi_i^B \right\rangle = 0$, we can write Eq. 5.3 as condition:

$$b_j + b_k + b_l = 0. \tag{5.4}$$

This means that in the nearest neighbour approximation, the sum of coefficients of the zero-energy states around each site must vanish. We will now focus our analysis on the majority sublattice - A, depicted by red dots in Fig. 5.1.

Each atom is labelled by two integer numbers n and m, which correspond to the row and column index, respectively, following the convention of Pascal's triangle. We ensure proper

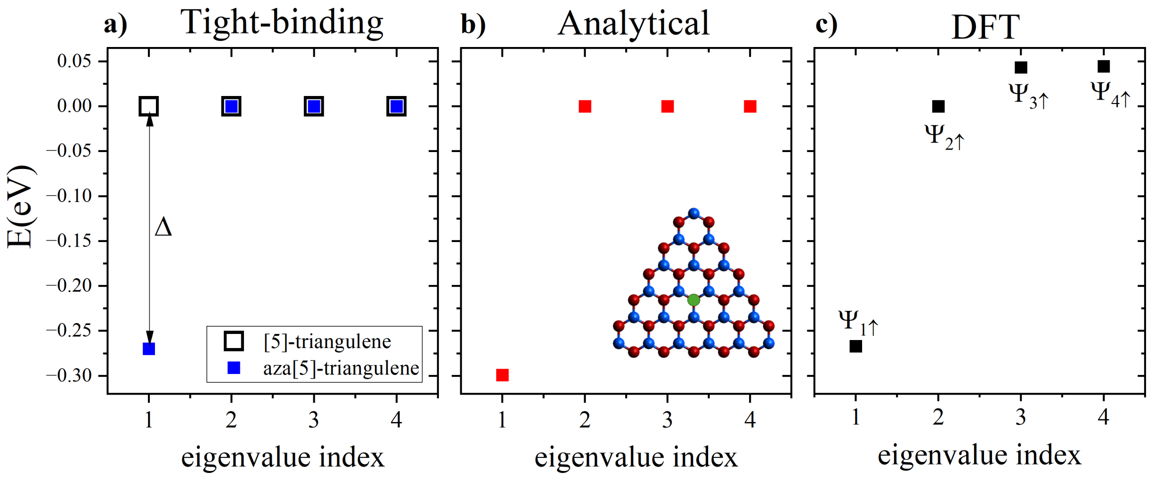

Figure 5.2: Degenerate shell of 5-TGQD with and without the nitrogen impurity. (a) Tight-binding calculation - black empty squares refer to 5-TGQD, while the blue squares correspond to 5-TGQD with nitrogen impurity. (b) Analytical result for 5-TGQD with nitrogen impurity, inset shows the location of the nitrogen defect in the 5-TGQD - note the green dot in the center of the triangle. For both the tight-binding and analytical calculations, the on-site energy of nitrogen δ was set to $5t$. (c) DFT calculation for 5-TGQD. In all three cases of 5-TGQD, the impurity is localized as shown in the inset of (b).

boundary conditions by adding auxiliary atoms in the corners of our triangle, depicted by empty red circles in Fig. 5.1(a). We now can use Eq. 5.4 to express all coefficients $b_{n,m}$ as linear combinations of the coefficients on the left edge, i.e. $b_{n,0}$. Starting from the top of our triangle, we can obtain $b_{0,1} = -(b_{0,0} + b_{1,1})$ and $b_{2,1} = -(b_{1,0} + b_{2,0})$. Using these expressions, and Eq. 5.4 again, we can apply the procedure to the coefficients in the second row. Repeating these steps for each row, we obtain all the needed coefficients. We note that this procedure can be carried out for all triangles, irrespective of their size. A general expression for any $b_{n,m}$ coefficient can be written as:

$$b_{n,m} = -(b_{n,m-1} + b_{n-1,m-1}). \tag{5.5}$$

This recurrence relation connects the coefficient of each atom to the two neighbouring atoms on its left.

We will now focus on an arbitrary atom labelled by $(k, 0)$, lying on the left edge, and another atom labelled by (n, m). Applying Eq. 5.5 to all coefficients on the left of atom $b_{n,m}$ leading up to the $b_{k,0}$ atom, one can notice that the sign of the calculated coefficients alternates with each progression. Specifically, when we reach atom $b_{k,0}$ on the left edge, the sign in front of the final expression becomes $(-1)^m$, where m represents the number of steps needed to arrive at the edge. Additionally, the number of paths connecting these two atoms corresponds to the binomial coefficient $\begin{pmatrix} m \\ n-k \end{pmatrix}$. These two observations allow us to formulate the following expression for the coefficient $b_{n,m}$:

$$b_{n,m} = (-1)^m \sum_{k \geq n-m}^{n} \begin{pmatrix} m \\ n-k \end{pmatrix} b_{k,0}. \tag{5.6}$$

We can now use our boundary conditions, i.e., impose vanishing of all the corner coefficients: $b_{0,0} = b_{N+1,0} = b_{N+1,N+1} = 0$. This reduces the number of independent coefficients to $N-1$, where N is the number of A-atoms on a given edge.

A similar analysis can be conducted for the B-sublattice. Again, we have to ensure proper boundary conditions, so additional atoms are added in such a way that all A-atoms have three nearest neighbours. We can now repeat the steps described above, using Eq. 5.4 to reduce the number of independent coefficients. However, in this case, after imposing the vanishing of coefficients on the auxiliary atoms, we end up with only one independent coefficient, which results in a trivial solution. This leads to the conclusion that the zero-energy states can only consist of coefficients from the majority sublattice, which builds up the zig-zag edge. Now, using Eq. 5.2 and Eq. 5.6, a general form of the states for the zero-energy shell can be written as:

$$\Psi^{\alpha} = \sum_{n=0}^{N+1} \sum_{m=0}^{N} \left[(-1)^m \sum_{k \geq n-m}^{n} \begin{pmatrix} m \\ n-k \end{pmatrix} b_{k,0}^{\alpha} \right] \phi_{n,m}^{A} \tag{5.7}$$

where $\phi_{n,m}^{A}$ is the p_z orbital on the A-type site (n, m).

In this expression, only the $N-1$ coefficients corresponding to atoms from the left edge are independent. Thus, we can construct $N-1$ linearly independent eigenvectors which span the subspace with zero-energy states. Our $N-1$ linearly independent eigenvectors are, in general, non-orthogonal. We therefore use the Gram-Schmidt algorithm to orthogonalize them. This way an orthonormal basis can be constructed, in which the zero-energy states can be written. We note that all the above calculations have been carried out for an all-carbon TGQD. This analysis will now be extended to a TGQD with nitrogen impurity.

To incorporate the effect of a nitrogen impurity into our tight-binding model, we have altered the on-site energy corresponding to the nitrogen site. The analytical calculation is conducted as follows. A new Hamiltonian, in which the nitrogen impurity is treated as a small perturbation, can be constructed:

$$H^{\text{aza}} = H + V_{\text{imp}}. \tag{5.8}$$

Here H is the original, all-carbon Hamiltonian, and $V_{\text{imp}} = \delta c^{\dagger}_{\text{imp}} c_{\text{imp}}$. δ is a parameter which corresponds to the on-site energy of nitrogen. The analytical solution for the degenerate shell of H has already been obtained:

$$H\left|A\right\rangle = \varepsilon_0 \left|A\right\rangle, \tag{5.9}$$

where $\left|A\right\rangle$ are the analytical vectors obtained above, and ε_0 is the energy of the degenerate shell. We will now use the set $\{\left|A\right\rangle\}$ as a basis to express the states of the degenerate shell of a TGQD with a nitrogen impurity $H^{\text{aza},0}$:

$$H^{\text{aza},0}_{\alpha\beta} = \left\langle A_\alpha\right| H^{\text{aza}} \left|A_\beta\right\rangle = \left\langle A_\alpha\right| H \left|A_\beta\right\rangle + \left\langle A_\alpha\right| V_{\text{imp}} \left|A_\beta\right\rangle. \tag{5.10}$$

Since the energy of the zero-energy states is zero, the first term disappears, and we are left with:

$$H^{\text{aza},0}_{\alpha\beta} = \left\langle A_\alpha\right| V_{\text{imp}} \left|A_\beta\right\rangle = \delta b^{\alpha}_{\text{imp}} b^{\beta}_{\text{imp}}. \tag{5.11}$$

The resulting Hamiltonian is, in general, a dense matrix of dimension $N-1$, which corresponds to the number of zero-energy states of the original system. To obtain the new energy values for a TGQD with a nitrogen impurity, we would have to diagonalize an arbitrarily large matrix. Since the original states were degenerate, any combination of them is also an eigenstate of the system. As such, we can use the first step of the Gauss elimination algorithm to rotate our analytical vectors $|A\rangle$ to a basis, where only one b_{imp} remains non-zero. This allows us to write $H^{\text{aza},0}$ in a diagonal form straight away, with only one non-zero eigenvalue. As a result, only one state from the zero-energy shell is shifted by $\delta|b'_{\text{imp}}|^2$, where b'_{imp} refers to the coefficient in the rotated basis.

5.1.1 Degenerate shell of a TGQD with a nitrogen impurity

We can now apply the above procedure to a specific case of 5-TGQD with a nitrogen impurity localized at the center of the system (see inset of Fig. 5.2(b)). We start by performing the tight-binding calculations. The resulting energy spectrum in the vicinity of the Fermi level has been shown in Fig. 5.2(a) (blue squares) and has been compared to the degenerate shell of an all-carbon 5-TGQD (black, empty squares). One can see that the degenerate shell, which previously consisted of 4 zero-energy states, is preserved, with only one state now having a lower energy. The other three states remain degenerate and at zero energy. The magnitude of this split, denoted as Δ, is indicated by the black arrow in Fig. 5.2(a). We compare this calculation with the analytical solution obtained through the procedure described above and presented in Fig. 5.2(b). Both of these results are in qualitative agreement.

Discrepancies in the magnitude of the split Δ between the tight-binding and analytical solutions can be attributed to the size of the basis used. In the analytical calculation, we only considered 4 eigenvectors to span our basis. However, increasing their number narrows the difference between the analytical and tight-binding solutions. Both results fully converge when all 46 eigenvectors are used to construct the basis. Additionally, we validated these findings through the *ab-initio* DFT calculations. The resulting energy spectrum of Kohn-Sham orbitals is depicted in Fig. 5.2(c). DFT calculations were conducted within the local density approximation using the Octopus software [330].

Having analyzed the energy spectrum, we now move on to examine the wave function probability densities of the zero-energy shell. In this step, we have compared the analytical,

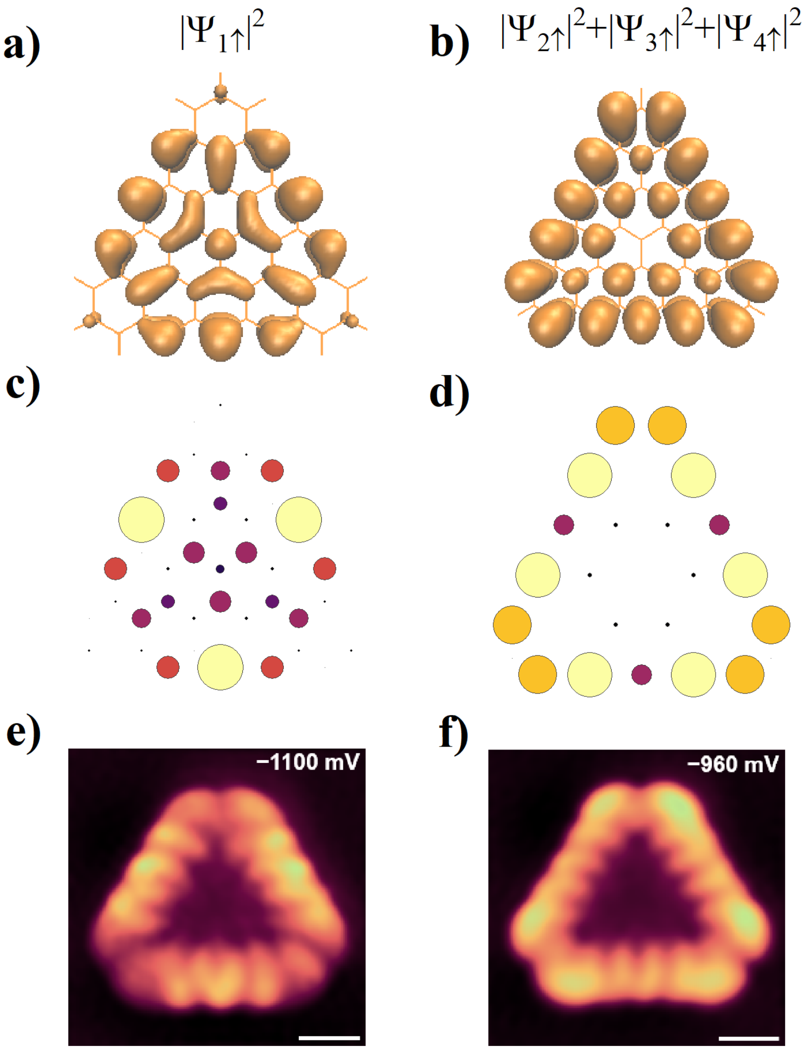

Figure 5.3: Degenerate shell wave function densities. The first column corresponds to the wave function density of the $\Psi_{1\uparrow}$ state marked in Fig 5.2 (c), while the second column corresponds to the sum of the $\Psi_{2\uparrow}$, $\Psi_{3\uparrow}$, $\Psi_{4\uparrow}$ states, shown in Fig 5.2 (c). (a) and (b) show the results of DFT calculation, and (c) and (d) show the results of analytical calculation. (e) and (f) present experimental constant current dI/dV images of 5-TGQD with a nitrogen impurity on Au(111) [3]. Imaging parameters: T = 4.3 K. I_T = 2 nA, lock-in bias voltage oscillation amplitude = 30 mV. Scale bars = 0.5 nm. Images have been FFT-filtered to remove higher frequency electronic noise. All of these results refer to the case of 5-TGQD with an impurity localized at the center of the structure.

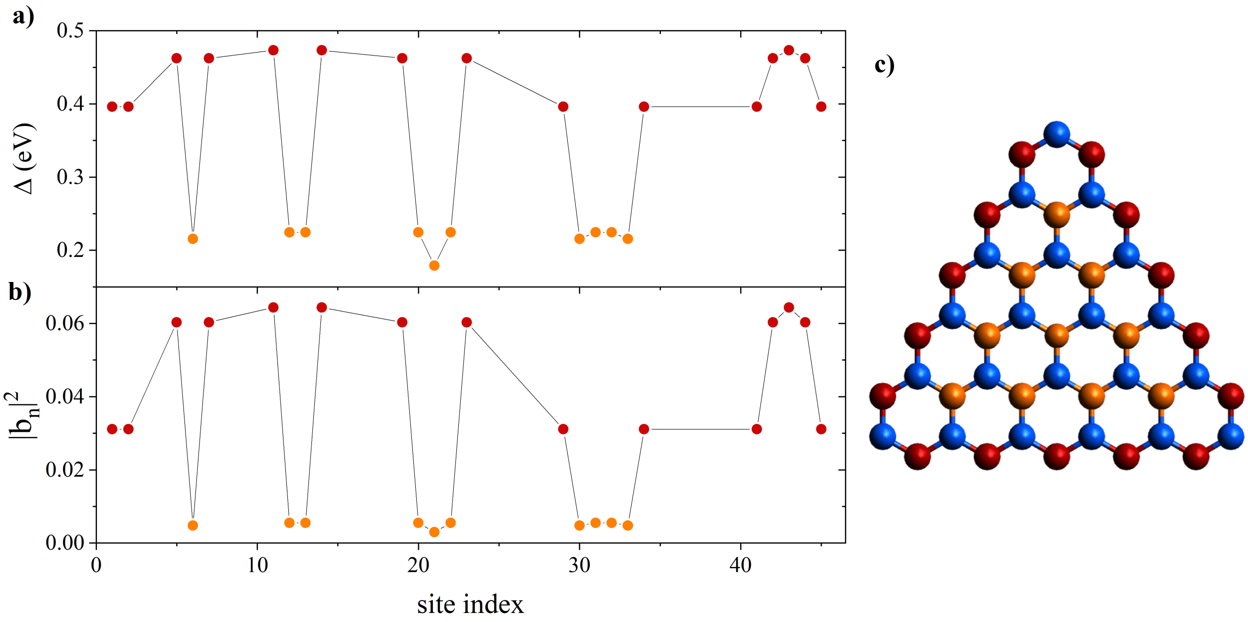

Figure 5.4: (a) Magnitude of the split of the degenerate shell for a 5-TGQD with a nitrogen impurity with impurity localized on different sites. Red data points correspond to the impurity position on red atoms shown in (c), while orange data points refer to the orange atoms in (c). (b) Magnitude of the wavefunction coefficient corresponding to the site with impurity. Red and orange data points are assigned analogously as (a). (c) Geometrical structure of a 5-TGQD with a nitrogen impurity. Edge A-atoms are marked in red, bulk A-atoms are marked in orange, while all B-atoms are marked in blue. The site index 0-45 has been allocated to each atom row by row from left to right e.g. the top blue atom has index zero, while in the second row the left red atom has index 1, and the right red one has index 2.

DFT and experimental results, all of which are presented in Fig. 5.3. All of these results refer to the case of 5-TGQD with an impurity localized at the center of the structure. The experiment considered here was conducted by the on-surface synthesis of 5-TGQD with a nitrogen impurity, via a one-step annealing process on Au(111). Then, scanning probe microscopy measurements were performed [3]. The dI/dV images presented in Fig. 5.3 (e) and (f) were obtained in the constant current mode with a CO tip.

In all three cases, we present the probability density of the lower lying state (denoted as $\Psi_{1\uparrow}$ in Fig. 5.2(c)) separately from the rest of the degenerate band (denoted as $\Psi_{2\uparrow}$, $\Psi_{3\uparrow}$, $\Psi_{4\uparrow}$ in Fig. 5.2(c)). One can note that all three methods yield similar results - the lower lying state is localized predominantly at the centers of the edges, with some non-zero contribution at the center of the quantum dot, while the other three states are localized entirely on the edges.

We can now generalize our problem to a TGQD with an impurity localized on an arbitrary atom. Fig. 5.4(a) shows an analysis of the energy Δ of the split-off level for all possible positions of the nitrogen atom on the majority sublattice. The red data points refer to the impurity localized on the edge of the quantum dot (red atoms in Fig. 5.4(c)), while the orange data points correspond to the bulk atoms, depicted also in orange in Fig. 5.4 (c). Panel (b) shows the magnitude of the wave function coefficient $|b_n|^2$ corresponding to the site with impurity. The colours of the data points have been assigned analogously as in (a). One can notice that there is a clear correlation between the magnitude of the energy split and the wave function coefficient on a given atom. This leads us to the conclusion that positioning the impurity at a given site and measuring the split between the first state and the rest of the degenerate shell allows us to effectively probe the wave function localized on that site. One can notice that both the split and the coefficient b_n are larger for the atoms corresponding to the edges of the sample (red data points). This observation is in agreement with the wave function densities presented in Fig. 5.3, where we saw that most of the wave function density is indeed localized at the edges of the quantum dot.

We note that moving the nitrogen impurity over the minority sublattice doesn't affect the structure of the degenerate shell, since the B-atom coefficients have no contribution to the zero-energy wave functions.

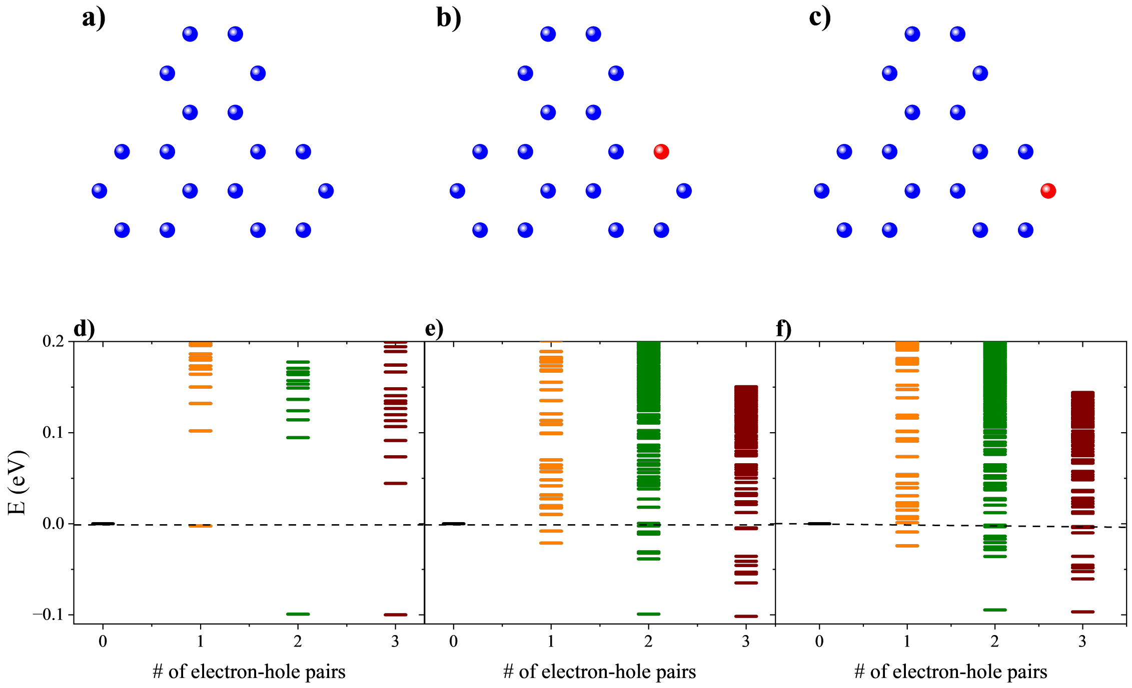

Figure 5.5: Geometry and energy spectra of TGQDs without and with the nitrogen impurity (a-c) geometry of the TGQDs. Blue dots denote carbon atoms, red dots refer to a nitrogen impurity. (d-f) Energy spectra as a function of the number of electron-hole pairs. The dashed line marks the ground state energy.

5.2 Absorption spectra of triangular graphene quantum dots with armchair edges and a nitrogen impurity.

We focus here on TGQDs with armchair edges. Specifically, we consider three structures: one composed entirely of carbon atoms, and two containing nitrogen impurities at different lattice sites, as illustrated in Fig. 5.5 (a-c), following the experiment from Ref. [53]. Our goal is to analyze the energy and absorption spectra and to investigate the influence of nitrogen impurities on these properties.

To perform this analysis, we employ the DFT+CI method described in Section 2.5.2. First, we carry out the DFT calculations within the local density approximation (LDA) using the Octopus software package [330] for all three geometries. These calculations yield KS energy levels and Coulomb matrix elements, which serve as input for computing the self-energies and subsequent CI calculations. We select a finite set of single-particle states and perform CI to obtain the many-body energy spectrum. The Hilbert space is restricted to a limited number of excitations, allowing us to study how the energy spectrum evolves with the inclusion of additional excited configurations. In general, adding a single excitation correction has the form:

$$|GS\rangle_1 = A_0 |GS\rangle_0 + \sum_{\alpha_1,\alpha_2} A_{\alpha_1,\alpha_2} b^{\dagger}_{\alpha_1} b_{\alpha_2} |GS\rangle_0 \tag{5.12}$$

where the operators $b^{\dagger}_{\alpha_i}(b_{\alpha_i})$ create (annihilate) a particle on KS orbital α_i. The index α_1 runs over the empty states, and the index α_2 over occupied states. Adding a bi-exciton correction would analogously look:

$$|GS\rangle_2 = A_0 |GS\rangle_0 + \sum_{\alpha_1,\alpha_2} A_{\alpha_1,\alpha_2} b^{\dagger}_{\alpha_1} b_{\alpha_2} |GS\rangle_0 + \sum_{\alpha_1,\alpha_2,\alpha_3,\alpha_4} A_{\alpha_1,\alpha_2,\alpha_3,\alpha_4} b^{\dagger}_{\alpha_1} b^{\dagger}_{\alpha_2} b_{\alpha_3} b_{\alpha_4} |GS\rangle_0 \tag{5.13}$$

and so on, for the higher corrections. The resulting spectra are shown in Fig. 5.5(a–c). In all cases, including higher-order excitations leads to a lowering of the ground state energy, consistent with previous findings in the literature (see, e.g., Ref. [52]). Notably, for the pristine all-carbon triangle, including the first excitation has only a minor effect on the energy. In contrast, for the nitrogen-doped structures, the inclusion of the same excitation results in a significant reduction of the ground state energy, highlighting the stronger correlation effects introduced by the impurity.

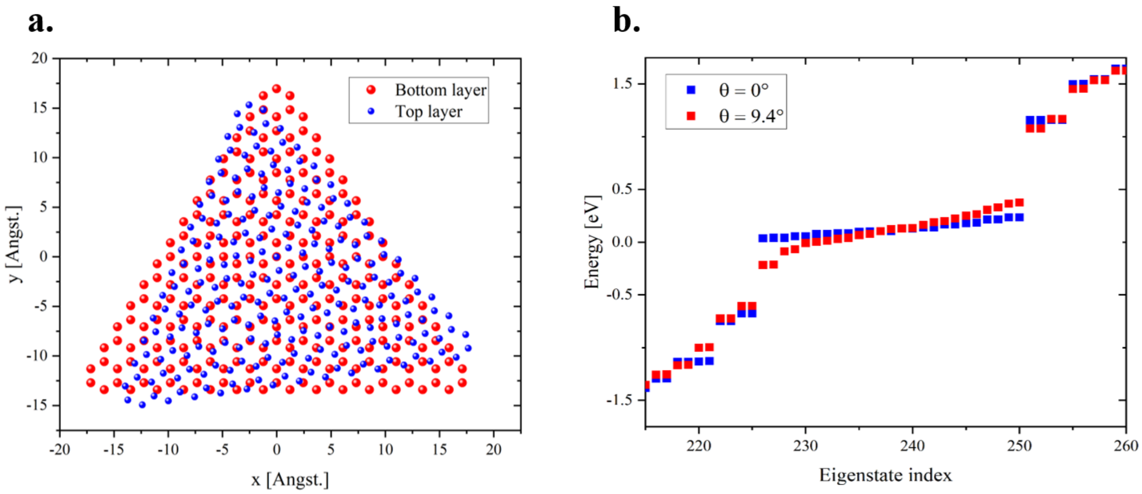

Figure 5.6: Twisted bilayer TGQD: (a) geometry of the quantum dot consisting of 475 atoms and twist angle $\theta = 9.4°$. Red dots refer to the atoms of the bottom layer, while blue dots refer to the top. (b) Energy spectrum close to the Fermi level for a un-twisted (blue squares) and twisted (red squares) structures

5.3 Twisted triangular graphene quantum dots with zig-zag edges

In this section, we combine two approaches to build a synthetic correlated electron system by combining two triangular graphene quantum dots with zigzag edges into a bilayer TGQD [42] and twisting them. The two degenerate electronic shells of each quantum dot combine into a single shell. We further twist the two triangles with respect to one another to engineer the degenerate shell at the Fermi level as a function of twist angle. We use the *ab initio* fitted tight-binding model Eq. 2.22:

$$H = \sum_{i,j}^{N_{UC}} \sum_{\alpha\beta}^{N_{at}} t_{ij}^{\alpha\beta} c^{\dagger}_{i\alpha} c_{j\beta}. \tag{5.14}$$

to study the evolution of the flat band a s function of the size of the quantum dot and the twist angle.

We consider two TGQDs with zig-zag edges in Bernal stacking. We twist them against a centrally located AB stacked atoms. Figure 5.6(a) illustrates the system under consideration, with twist angle $\theta = 9.4°$. One can already notice the beginning of moiré pattern formation, which in this case has a period equal to 0.65 nm. Panel (b) compares the energy spectra near the Fermi level for two configurations—the untwisted and the twisted TGQD shown in panel (a). The zero energy shell is not perfectly flat even in the case of $\theta = 0$, because we include long-distance hoppings that lead to breaking of the degeneracy of the zero energy states. Introducing a twist modifies the degenerate shell, leading to a noticeable broadening of its energy levels and reduction of the band gap between the top (bottom) of the valence (conduction) band and the zero-energy shell.

We then study the interplay of the size quantization and the twist angle. We consider two systems - one consisting of ~ 170 atoms, and the other one of ~ 1500 atoms (see Fig. 5.7(a–b)). We consider three twist angles - $\theta = 0°, 1.1°, 3.1°$. The non-zero twist angles are commensurate and lead to the formation of a moiré pattern. The larger the twist angle, the larger the spread of the degenerate shell denoted by a blue arrow in Fig. 5.7 (a-b). The spread of the shell also grows with the size of the system. That result is surprising, since the formation of the moiré pattern for the magic angle should lead to the flattening of the shell. We conclude that the considered triangles are too small for the moiré pattern to have a significant influence. Fig. 5.7(c–d) shows numerical values of the energy spread for a wider range of the twist angles. One can see that for a smaller system, the spread grows together with the system size, until it plateaus for $\theta > 8°$. For the larger system, the spread reaches a maximum for $\theta = 3°$ and then decreases. However, the shell is never flatter than for the untwisted case.

5.4 Conclusions

In the first section, we demonstrated how a localized impurity can be used to probe the wave functions of a degenerate shell in a triangular graphene quantum dot with broken sublattice symmetry. We demonstrated its applicability on the example of triangular graphene

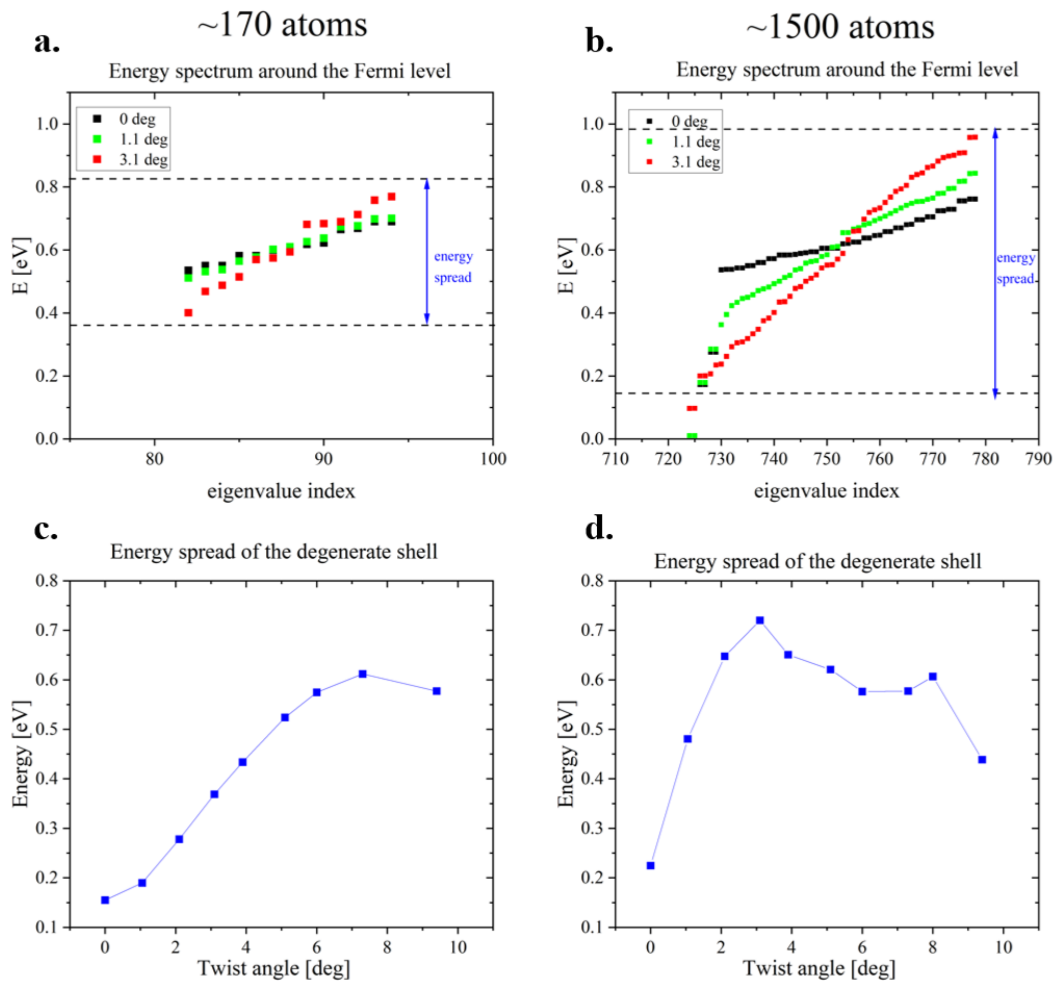

Figure 5.7: Electronic properties of twisted bilayer TGQD: (a) Energy spectra around the fermi level for dots consisting of ∼ 170 atoms, non-twisted (black squares), twisted by $\theta = 1.1^\circ$ (green squares) and $\theta = 3.1^\circ$ (red squares). The blue arrow shows the energy spread of the flat band. (b) Analogous plot for a larger system, containing ∼ 1500 atoms. (c) Energy spread of the degenerate shell of the system from (a) as a function of the twist angle. (d) Analogous plot for the (b) system.

quantum dots with a nitrogen impurity. Starting from the analytical solutions of the singular eigenvalue problem for an all-carbon triangular graphene quantum dot, we constructed a framework to describe the system with a nitrogen impurity. We predicted that the presence of the impurity leads to a characteristic "peeling off" of one energy level from the zero-energy band. This effect directly probes the degenerate shell's wave functions at the impurity site. Our theoretical predictions were validated by tight-binding and *ab initio* calculations and by comparison with experimental results.

We then studied armchair triangular graphene quantum dots with a nitrogen impurity using a density functional theory + configuration interactions framework. We find that the presence of the nitrogen impurity dramatically changes the system's energy spectrum. We also note that including excitations lowers the ground state energy in both cases, but the effect is more pronounced for quantum dots with nitrogen impurity.

In the final section, we study twisted bilayer triangular graphene quantum dots. These structures twisted by a commensurate angle create a unique platform for studies of electronic correlation. In this work, we show that introducing the twist allows for manipulation of the degenerate shell in triangular graphene quantum dots, leading to broadening and reducing the energy gap. These results are a promising start in an analysis of the influence of the moiré period on such structures.

Chapter 6

Conclusions and perspectives

In this thesis, we have explored several graphene-based nanostructures, focusing on their electronic structure, correlation effects, and response to external perturbations such as magnetic and electric fields, substrates, and impurities. Our results provide valuable microscopic insights relevant to both fundamental understanding and future experimental realizations.

We first investigated magic-angle twisted bilayer graphene in nanoribbon geometry, supported by a hexagonal boron nitride substrate and subjected to an external magnetic field. By simulating systems as large as one million atoms, we showed that smaller systems with as few as 20 moiré unit cells can effectively capture essential electronic features, including the decoupling of edge and bulk states. We computed the Hofstadter spectrum, extracted in-gap Chern numbers via edge state counting, and identified insulating phases at low magnetic fields using Wannier diagrams. Our analysis revealed three distinct types of bulk and edge states—moiré, mixed, and conventional—and tracked their evolution with magnetic field and momentum. While our analysis was primarily restricted to single-particle physics without electrostatic corrections for doping away from $\nu = 0$, we anticipate that our findings can provide valuable guidance for future scanning tunnelling microscopy measurements and help to experimentally establish properties of microscopic wave functions in twisted bilayer graphene.

We further examined the impact of electronic interactions on the magic angle twisted bilayer graphene by including the electrostatic Hartree correction. This led to a substantial renormalization of the band structure and smoothing of the charge distribution across the moiré unit cell. While we observed a high degree of particle-hole symmetry across all flat-band fillings, the Hartree term alone failed to induce an energy gap. This necessitated the inclusion of additional interaction effects, such as the Hubbard term, to capture correlation-driven phenomena.

Next, we turned to mirror-symmetric twisted trilayer graphene, a highly tunable moiré system. Our calculations revealed that the critical Hubbard interaction strength required to drive a magnetic phase transition from paramagnetic to antiferromagnetic states is lower than in other graphene-based materials. However, this antiferromagnetic phase is sensitive to symmetry-breaking perturbations, such as vertical electric fields and the presence of a hexagonal boron nitride substrate. In addition, we identified a form of "hidden" quantum geometry in the form of a nontrivial Berry curvature distribution, despite the absence of Chern numbers at charge neutrality. We demonstrated that this Berry curvature can be tuned with electric fields, which is particularly relevant for understanding valley-polarized states at low doping. Our findings highlight the intricate interplay of electric field, sublattice symmetry breaking, and electron-electron interactions in determining the magnetic and electronic properties of twisted trilayer graphene. The tunability of these parameters provides a promising pathway to designing devices with controllable correlated and topological phases. This study underscores twisted trilayer graphene as a versatile platform to probe and manipulate quantum materials' magnetic and electronic properties.

We also investigated triangular graphene quantum dots, focusing on how impurities and moiré engineering affect their electronic structure. Using an analytical approach grounded in the singular eigenvalue problem, we showed that introducing a localized impurity, such as nitrogen, leads to a characteristic "peeling off" of a single energy level from the degenerate zero-energy band. This allowed us to directly probe the wave functions of the degenerate shell at the impurity site, with results confirmed by tight-binding, *ab initio* methods, and experimental data. Extending this study to armchair-edged triangular graphene quantum dots with a nitrogen impurity, we used a density functional theory + configuration interactions framework to show that the impurity significantly modifies the energy spectrum, with excitations further lowering the ground state energy—an effect more pronounced in doped systems. Finally, we considered twisted bilayer triangular graphene quantum dots, where commensurate twisting offers a new degree of tunability. We demonstrated that twisting broadens the degenerate shell and reduces the energy gap, pointing to the promise of moiré patterning as a tool for controlling electronic correlations in graphene quantum dots.

In our future work, we aim to extend our analysis to the extended Hubbard model, and to employ the projected Hartree-Fock method to study moiré systems away from charge neutrality, where topological properties may become non-trivial. We also plan to broaden our focus beyond graphene-based systems to include transition metal dichalcogenides. Building on our recent work on quantum dots in monolayer WSe_2 [301], we intend to develop models for twisted homo- and hetero-bilayer structures using a variety of theoretical and computational tools.

Bibliography

[1] Long-Jing Yin, Ling-Hui Tong, Yue-Ying Zhou, Yang Zhang, Yuan Tian, Li Zhang, Lijie Zhang, and Zhihui Qin. Direct observation of moiré flat-band breakdown at the edge of magic-angle twisted bilayer graphene. *Phys. Rev. B*, 105:L201405, 2022.

[2] Andrew T. Pierce, Yonglong Xie, Jeong Min Park, Eslam Khalaf, Seung Hwan Lee, Yuan Cao, Daniel E. Parker, Patrick R. Forrester, Shaowen Chen, Kenji Watanabe, Takashi Taniguchi, Ashvin Vishwanath, Pablo Jarillo-Herrero, and Amir Yacoby. Unconventional sequence of correlated chern insulators in magic-angle twisted bilayer graphene. *Nature Physics*, 17(11):1210–1215, 2021.

[3] James Lawrence, Yuanyuan He, Haipeng Wei, Jie Su, Shaotang Song, Alina Wania Rodrigues, Daniel Miravet, Pawel Hawrylak, Jianwei Zhao, Jishan Wu, and Jiong Lu. Topological design and synthesis of high-spin aza-triangulenes without jahn–teller distortions. *ACS Nano*, 17(20):20237–20245, 2023.

[4] K. S. Novoselov, A. K. Geim, S. V. Morozov, D. Jiang, Y. Zhang, S. V. Dubonos, I. V. Grigorieva, and A. A. Firsov. Electric field effect in atomically thin carbon films. *Science*, 306(5696):666–669, 2004.

[5] K. S. Novoselov, D. Jiang, F. Schedin, T. J. Booth, V. V. Khotkevich, S. V. Morozov, and A. K. Geim. Two-dimensional atomic crystals. *Proceedings of the National Academy of Sciences*, 102(30):10451–10453, 2005.

[6] Wencai Ren, Peter Bøggild, Joan Redwing, Kostya Novoselov, Luzhao Sun, Yue Qi, Kaicheng Jia, Zhongfan Liu, Oliver Burton, Jack Alexander-Webber, Stephan Hof-

mann, Yang Cao, Yu Long, Quan-Hong Yang, Dan Li, Soo Ho Choi, Ki Kang Kim, Young Hee Lee, Mian Li, Qing Huang, Yury Gogotsi, Nicholas Clark, Amy Carl, Roman Gorbachev, Thomas Olsen, Johanna Rosen, Kristian Sommer Thygesen, Dmitri K. Efetov, Bjarke S. Jessen, Matthew Yankowitz, Julien Barrier, Roshan Krishna Kumar, Frank H. L. Koppens, Hui Deng, Xiaoqin Li, Siyuan Dai, D. N. Basov, Xinran Wang, Saptarshi Das, Xiangfeng Duan, Zhihao Yu, Markus Borsch, Andrea C. Ferrari, Rupert Huber, Mackillo Kira, Fengnian Xia, Xiao Wang, Zhong-Shuai Wu, Xinliang Feng, Patrice Simon, Hui-Ming Cheng, Bilu Liu, Yi Xie, Wanqin Jin, Rahul Raveendran Nair, Yan Xu, Qing Zhang, Ajit K. Katiyar, Jong-Hyun Ahn, Igor Aharonovich, Mark C. Hersam, Stephan Roche, Qilin Hua, Guozhen Shen, Tianling Ren, Hao-Bin Zhang, Chong Min Koo, Nikhil Koratkar, Vittorio Pellegrini, Robert J. Young, Bill Qu, Max Lemme, and Andrew J. Pollard. The 2d materials roadmap. *arXiv preprint*, arXiv:2503.22476, 2025.

[7] Rafi Bistritzer and Allan H. MacDonald. Moiré bands in twisted double-layer graphene. *Proceedings of the National Academy of Sciences*, 108(30):12233–12237, 2011.

[8] Yuan Cao, Valla Fatemi, Ahmet Demir, Shiang Fang, Spencer L. Tomarken, Jason Y. Luo, Javier D. Sanchez-Yamagishi, Kenji Watanabe, Takashi Taniguchi, Efthimios Kaxiras, Ray C. Ashoori, and Pablo Jarillo-Herrero. Correlated insulator behaviour at half-filling in magic-angle graphene superlattices. *Nature*, 556(7699):80–84, 2018.

[9] Yuan Cao, Valla Fatemi, Shiang Fang, Kenji Watanabe, Takashi Taniguchi, Efthimios Kaxiras, and Pablo Jarillo-Herrero. Unconventional superconductivity in magic-angle graphene superlattices. *Nature*, 556(7699):43–50, 2018.

[10] P. R. Wallace. The band theory of graphite. *Phys. Rev.*, 71:622–634, 1947.

[11] J. W. McClure. Band structure of graphite and de haas-van alphen effect. *Phys. Rev.*, 108:612–618, 1957.

[12] J. C. Slonczewski and P. R. Weiss. Band structure of graphite. *Phys. Rev.*, 109:272–279, 1958.

[13] G. Dresselhaus and M. S. Dresselhaus. Spin-orbit interaction in graphite. *Phys. Rev.*, 140:A401–A412, 1965.

[14] Gordon W. Semenoff. Condensed-matter simulation of a three-dimensional anomaly. *Phys. Rev. Lett.*, 53:2449–2452, 1984.

[15] Leonid A. Ponomarenko, Alessandro Principi, Andy D. Niblett, Wendong Wang, Roman V. Gorbachev, Piranavan Kumaravadivel, Alexey I. Berdyugin, Alexey V. Ermakov, Sergey Slizovskiy, Kenji Watanabe, Takashi Taniguchi, Qi Ge, Vladimir I. Fal'ko, Laurence Eaves, Mark T. Greenaway, and Andre K. Geim. Extreme electron–hole drag and negative mobility in the dirac plasma of graphene. *Nature Communications*, 15(1):9869, 2024.

[16] Alev Devrim Güçlü, Pawel Potasz, Marek Korkusinski, and Pawel Hawrylak. *Graphene quantum dots.* Springer, 2014.

[17] S. Das Sarma, Shaffique Adam, E. H. Hwang, and Enrico Rossi. Electronic transport in two-dimensional graphene. *Rev. Mod. Phys.*, 83:407–470, 2011.

[18] C. W. J. Beenakker. Colloquium: Andreev reflection and klein tunneling in graphene. *Rev. Mod. Phys.*, 80:1337–1354, 2008.

[19] Choongyu Hwang, David A. Siegel, Sung-Kwan Mo, William Regan, Ariel Ismach, Yuegang Zhang, Alex Zettl, and Alessandra Lanzara. Fermi velocity engineering in graphene by substrate modification. *Scientific Reports*, 2(1):590, 2012.

[20] Horst L. Stormer, Daniel C. Tsui, and Arthur C. Gossard. The fractional quantum hall effect. *Rev. Mod. Phys.*, 71:S298–S305, 1999.

[21] B. I. Halperin, Patrick A. Lee, and Nicholas Read. Theory of the half-filled landau level. *Phys. Rev. B*, 47:7312–7343, 1993.

[22] R. R. Du, H. L. Stormer, D. C. Tsui, L. N. Pfeiffer, and K. W. West. Experimental evidence for new particles in the fractional quantum hall effect. *Phys. Rev. Lett.*, 70:2944–2947, 1993.

[23] R. L. Willett, R. R. Ruel, K. W. West, and L. N. Pfeiffer. Experimental demonstration of a fermi surface at one-half filling of the lowest landau level. *Phys. Rev. Lett.*, 71:3846–3849, 1993.

[24] R. de Picciotto, M. Reznikov, M. Heiblum, V. Umansky, G. Bunin, and D. Mahalu. Direct observation of a fractional charge. *Nature*, 389(6647):162–164, 1997.

[25] L. Saminadayar, D. C. Glattli, Y. Jin, and B. Etienne. Observation of the $e/3$ fractionally charged laughlin quasiparticle. *Phys. Rev. Lett.*, 79:2526–2529, 1997.

[26] M. Byszewski, B. Chwalisz, D. K. Maude, M. L. Sadowski, M. Potemski, T. Saku, Y. Hirayama, S. Studenikin, D. G. Austing, A. S. Sachrajda, and P. Hawrylak. Optical probing of composite fermions in a two-dimensional electron gas. *Nature Physics*, 2(4):239–243, 2006.

[27] R. Bistritzer and A. H. MacDonald. Moiré butterflies in twisted bilayer graphene. *Phys. Rev. B*, 84:035440, 2011.

[28] Shantanu Mishra, Doreen Beyer, Kristjan Eimre, Shawulienu Kezilebieke, Reinhard Berger, Carlo A. Gröning, Oliver Pignedoli, Klaus Müllen, Pascal Liljeroth, Peter Ruffieux, Xinliang Feng, and Roman Fasel. Topological frustration induces unconventional magnetism in a nanographene. *Nature Nanotechnology*, 15, 2020.

[29] Niko Pavliček, Anish Mistry, Zsolt Majzik, Nikolaj Moll, Gerhard Meyer, David J. Fox, and Leo Gross. Synthesis and characterization of triangulene. *Nature Nanotechnology*, 12, 2017.

[30] A. D. Güçlü, P. Potasz, O. Voznyy, M. Korkusinski, and P. Hawrylak. Magnetism and correlations in fractionally filled degenerate shells of graphene quantum dots. *Phys. Rev. Lett.*, 103:246805, 2009.

[31] Jie Su, Mykola Telychko, Pan Hu, Gennevieve Macam, Pingo Mutombo, Hejian Zhang, Yang Bao, Fang Cheng, Zhi-Quan Huang, Zhizhan Qiu, Sherman J. R. Tan,

Hsin Lin, Pavel Jelínek, Feng-Chuan Chuang, Jishan Wu, and Jiong Lu. Atomically precise bottom-up synthesis of π-extended [5]triangulene. *Science Advances*, 5(7):eaav7717, 2019.

[32] Jie Su, Mykola Telychko, Shaotang Song, and Jiong Lu. Triangulenes: From precursor design to on-surface synthesis and characterization. *Angewandte Chemie International Edition*, 59(20):7658–7668.

[33] Jie Su, Wei Fan, Pingo Mutombo, Xinnan Peng, Shaotang Song, Martin Ondráček, Pavlo Golub, Jiří Brabec, Libor Veis, Mykola Telychko, Pavel Jelínek, Jishan Wu, and Jiong Lu. On-surface synthesis and characterization of [7]triangulene quantum ring. *Nano Letters*, 21(1):861–867, 2021.

[34] Leoš Valenta and Michal Juríček. The taming of clar's hydrocarbon. *Chem. Commun.*, 58:10896–10906, 2022.

[35] Shantanu Mishra, Doreen Beyer, Kristjan Eimre, Junzhi Liu, Reinhard Berger, Oliver Gröning, Carlo A. Pignedoli, Klaus Müllen, Roman Fasel, Xinliang Feng, and Pascal Ruffieux. Synthesis and characterization of π-extended triangulene. *Journal of the American Chemical Society*, 141(27):10621–10625, 2019.

[36] Shantanu Mishra, Kun Xu, Kristjan Eimre, Hartmut Komber, Ji Ma, Carlo A. Pignedoli, Roman Fasel, Xinliang Feng, and Pascal Ruffieux. Synthesis and characterization of [7]triangulene. *Nanoscale*, 13:1624–1628, 2021.

[37] Elia Turco, Annika Bernhardt, Nils Krane, Leoš Valenta, Roman Fasel, Michal Juríček, and Pascal Ruffieux. Observation of the magnetic ground state of the two smallest triangular nanographenes. *JACS Au*, 3(5):1358–1364, 2023.

[38] J. Fernández-Rossier and J. J. Palacios. Magnetism in graphene nanoislands. *Phys. Rev. Lett.*, 99:177204, 2007.

[39] P. Potasz, A. D. Güçlü, and P. Hawrylak. Zero-energy states in triangular and trapezoidal graphene structures. *Phys. Rev. B*, 81:033403, 2010.

[40] A. D. Güçlü, P. Potasz, O. Voznyy, M. Korkusinski, and P. Hawrylak. Magnetism and correlations in fractionally filled degenerate shells of graphene quantum dots. *Phys. Rev. Lett.*, 103:246805, 2009.

[41] A. D. Güçlü, P. Potasz, and P. Hawrylak. Excitonic absorption in gate-controlled graphene quantum dots. *Phys. Rev. B*, 82:155445, 2010.

[42] P. Potasz, A. D. Güçlü, A. Wójs, and P. Hawrylak. Electronic properties of gated triangular graphene quantum dots: Magnetism, correlations, and geometrical effects. *Phys. Rev. B*, 85:075431, 2012.

[43] O. Voznyy, A. D. Güçlü, P. Potasz, and P. Hawrylak. Effect of edge reconstruction and passivation on zero-energy states and magnetism in triangular graphene quantum dots with zigzag edges. *Phys. Rev. B*, 83:165417, 2011.

[44] Elliott H. Lieb. Two theorems on the hubbard model. *Phys. Rev. Lett.*, 62:1201–1204, 1989.

[45] Neil W. Ashcroft and N. David Mermin. *Solid State Physics.* Harcourt College Publishers, New York, 1976.

[46] Tao Wang, Alejandro Berdonces-Layunta, Niklas Friedrich, Manuel Vilas-Varela, Jan Patrick Calupitan, Jose Ignacio Pascual, Diego Peña, David Casanova, Martina Corso, and Dimas G. de Oteyza. Aza-triangulene: On-surface synthesis and electronic and magnetic properties. *Journal of the American Chemical Society*, 144(10):4522–4529, 2022.

[47] Haipeng Wei, Xudong Hou, Tingting Xu, Ya Zou, Guangwu Li, Shaofei Wu, Yanhou Geng, and Jishan Wu. Solution-phase synthesis and isolation of an aza-triangulene and its cation in crystalline form. *Angewandte Chemie International Edition*, 61(40):e202210386, 2022.

[48] J. C. G. Henriques, D. Jacob, A. Molina-Sánchez, G. Catarina, A. T. Costa, and J. Fernández-Rossier. Beyond spin models in orbitally-degenerate open-shell nanographenes. *arXiv*, 2023.

[49] Donglin Li, Orlando J. Silveira, Takuma Matsuda, Hironobu Hayashi, Hiromitsu Maeda, Adam S. Foster, and Shigeki Kawai. On-surface synthesis of triaza[5]triangulene through cyclodehydrogenation and its magnetism. *Angewandte Chemie International Edition*, page e202411893, 2024.

[50] Manuel Vilas-Varela, Francisco Romero-Lara, Alessio Vegliante, Jan Patrick Calupitan, Adrián Martínez, Lorenz Meyer, Unai Uriarte-Amiano, Niklas Friedrich, Dongfei Wang, Fabian Schulz, Natalia E. Koval, María E. Sandoval-Salinas, David Casanova, Martina Corso, Emilio Artacho, Diego Peña, and José Ignacio Pascual. On-surface synthesis and characterization of a high-spin aza-[5]-triangulene. *Angewandte Chemie International Edition*, 62(41):e202307884, 2023.

[51] Isil Ozfidan, Marek Korkusinski, and Pawel Hawrylak. Electronic properties and electron–electron interactions in graphene quantum dots. *physica status solidi (RRL) – Rapid Research Letters*, 10(1):13–23, 2016.

[52] Isil Ozfidan, Marek Korkusinski, A. Devrim Güçlü, John A. McGuire, and Pawel Hawrylak. Microscopic theory of the optical properties of colloidal graphene quantum dots. *Phys. Rev. B*, 89:085310, 2014.

[53] Shuhong Xu, Linfeng Tan, Fan Liu, Yiping Cui, Chunlei Wang, and Rong Zhang. Investigation of optical properties for n- and f-doped triangular shaped carbon molecules. *Journal of Molecular Modeling*, 27(6):154, 2021.

[54] Fanglong Yuan, Ting Yuan, Laizhi Sui, Zhibin Wang, Zifan Xi, Yunchao Li, Xiaohong Li, Louzhen Fan, Zhan'ao Tan, Anmin Chen, Mingxing Jin, and Shihe Yang. Engineering triangular carbon quantum dots with unprecedented narrow bandwidth emission for multicolored leds. *Nature Communications*, 9(1):2249, 2018.

[55] Guohong Li, Adina Luican, and Eva Y. Andrei. Scanning tunneling spectroscopy of graphene on graphite. *Phys. Rev. Lett.*, 102:176804, 2009.

[56] J. M. B. Lopes dos Santos, N. M. R. Peres, and A. H. Castro Neto. Graphene bilayer with a twist: Electronic structure. *Phys. Rev. Lett.*, 99:256802, 2007.

[57] Eva Y. Andrei, Dmitri K. Efetov, Pablo Jarillo-Herrero, Allan H. MacDonald, Kin Fai Mak, T. Senthil, Emanuel Tutuc, Ali Yazdani, and Andrea F. Young. The marvels of moiré materials. *Nature Reviews Materials*, 6(3):201–206, 2021.

[58] Ethan Lake, Adarsh S. Patri, and T. Senthil. Pairing symmetry of twisted bilayer graphene: A phenomenological synthesis. *Phys. Rev. B*, 106:104506, 2022.

[59] Chuanqi Zheng and Xiaoxue Liu. Superconductivity and topological quantum states in two-dimensional moiré superlattices. *Quantum Frontiers*, 3(1):17, 2024.

[60] T. Senthil. Possible nodal superconducting pairing in magic angle twisted graphene layers. *Journal Club for Condensed Matter Physics*, 2025. Commentary on recent studies of superconductivity in magic-angle twisted bilayer graphene.

[61] Jeong Min Park, Yuan Cao, Kenji Watanabe, Takashi Taniguchi, and Pablo Jarillo-Herrero. Tunable strongly coupled superconductivity in magic-angle twisted trilayer graphene. *Nature*, 590(7845):249–255, 2021.

[62] Zeyu Hao, A. M. Zimmerman, Patrick Ledwith, Eslam Khalaf, Danial Haie Najafabadi, Kenji Watanabe, Takashi Taniguchi, Ashvin Vishwanath, and Philip Kim. Electric field–tunable superconductivity in alternating-twist magic-angle trilayer graphene. *Science*, 371(6534):1133–1138, 2021.

[63] Yuan Cao, Jeong Min Park, Kenji Watanabe, Takashi Taniguchi, and Pablo Jarillo-Herrero. Pauli-limit violation and re-entrant superconductivity in moiré graphene. *Nature*, 595(7868):526–531, 2021.

[64] Trithep Devakul, Patrick J. Ledwith, Li-Qiao Xia, Aviram Uri, Sergio de la Barrera, Pablo Jarillo-Herrero, and Liang Fu. Magic-angle helical trilayer graphene, 2023.

[65] Ruiheng Su, Manabendra Kuiri, Kenji Watanabe, Takashi Taniguchi, and Joshua Folk. Superconductivity in twisted double bilayer graphene stabilized by WSe_2. *Nature Materials*, 22(11):1332–1337, 2023.

[66] Tonghang Han, Zhengguang Lu, Giovanni Scuri, Jiho Sung, Jue Wang, Tianyi Han, Kenji Watanabe, Takashi Taniguchi, Hongkun Park, and Long Ju. Correlated insulator and Chern insulators in pentalayer rhombohedral-stacked graphene. *Nature Nanotechnology*, 19(2):181–187, 2024.

[67] Yanhao Tang, Lizhong Li, Tingxin Li, Yang Xu, Song Liu, Katayun Barmak, Kenji Watanabe, Takashi Taniguchi, Allan H. MacDonald, Jie Shan, and Kin Fai Mak. Simulation of Hubbard model physics in $\mathrm{WSe}_2/\mathrm{WS}_2$ moiré superlattices. *Nature*, 579(7799):353–358, 2020.

[68] Cheng Shen, Yanbang Chu, QuanSheng Wu, Na Li, Shuopei Wang, Yanchong Zhao, Jian Tang, Jieying Liu, Jinpeng Tian, Kenji Watanabe, Takashi Taniguchi, Rong Yang, Zi Yang Meng, Dongxia Shi, Oleg V. Yazyev, and Guangyu Zhang. Correlated states in twisted double bilayer graphene. *Nature Physics*, 16(5):520–525, 2020.

[69] Yuan Cao, Daniel Rodan-Legrain, Oriol Rubies-Bigorda, Jeong Min Park, Kenji Watanabe, Takashi Taniguchi, and Pablo Jarillo-Herrero. Tunable correlated states and spin-polarized phases in twisted bilayer–bilayer graphene. *Nature*, 583(7815):215–220, 2020.

[70] Xiaomeng Liu, Zeyu Hao, Eslam Khalaf, Jong Yeon Lee, Yuval Ronen, Hyobin Yoo, Danial Haei Najafabadi, Kenji Watanabe, Takashi Taniguchi, Ashvin Vishwanath, and Philip Kim. Tunable spin-polarized correlated states in twisted double bilayer graphene. *Nature*, 583(7815):221–225, 2020.

[71] Shaowen Chen, Minhao He, Ya-Hui Zhang, Valerie Hsieh, Zaiyao Fei, K. Watanabe, T. Taniguchi, David H. Cobden, Xiaodong Xu, Cory R. Dean, and Matthew Yankowitz. Electrically tunable correlated and topological states in twisted monolayer–bilayer graphene. *Nature Physics*, 17(3):374–380, 2021.

[72] Guorui Chen, Lili Jiang, Shuang Wu, Bosai Lyu, Hongyuan Li, Bheema Lingam Chittari, Kenji Watanabe, Takashi Taniguchi, Zhiwen Shi, Jeil Jung, Yuanbo Zhang, and Feng Wang. Evidence of a gate-tunable Mott insulator in a trilayer graphene moiré superlattice. *Nature Physics*, 15(3):237–241, 2019.

[73] M. Serlin, C. L. Tschirhart, H. Polshyn, Y. Zhang, J. Zhu, K. Watanabe, T. Taniguchi, L. Balents, and A. F. Young. Intrinsic quantized anomalous hall effect in a moiré heterostructure. *Science*, 367(6480):900–903, 2020.

[74] Aaron L. Sharpe, Eli J. Fox, Arthur W. Barnard, Joe Finney, Kenji Watanabe, Takashi Taniguchi, M. A. Kastner, and David Goldhaber-Gordon. Emergent ferromagnetism near three-quarters filling in twisted bilayer graphene. *Science*, 365(6453):605–608, 2019.

[75] Emma C. Regan, Danqing Wang, Chenhao Jin, M. Iqbal Bakti Utama, Beini Gao, Xin Wei, Sihan Zhao, Wenyu Zhao, Zuocheng Zhang, Kentaro Yumigeta, Mark Blei, Johan D. Carlström, Kenji Watanabe, Takashi Taniguchi, Sefaattin Tongay, Michael Crommie, Alex Zettl, and Feng Wang. Mott and generalized Wigner crystal states in WSe_2/WS_2 moiré superlattices. *Nature*, 579(7799):359–363, 2020.

[76] Matthew Yankowitz, Shaowen Chen, Hryhoriy Polshyn, Yuxuan Zhang, K. Watanabe, T. Taniguchi, David Graf, Andrea F. Young, and Cory R. Dean. Tuning superconductivity in twisted bilayer graphene. *Science*, 363(6431):1059–1064, 2019.

[77] Yonglong Xie, Biao Lian, Berthold Jäck, Xiaomeng Liu, Cheng-Li Chiu, Kenji Watanabe, Takashi Taniguchi, B. Andrei Bernevig, and Ali Yazdani. Spectroscopic signatures of many-body correlations in magic-angle twisted bilayer graphene. *Nature*, 572(7767):101–105, 2019.

[78] Yuan Cao, Daniel Rodan-Legrain, Jeong Min Park, Noah F. Q. Yuan, Kenji Watanabe, Takashi Taniguchi, Rafael M. Fernandes, Liang Fu, and Pablo Jarillo-Herrero. Nematicity and competing orders in superconducting magic-angle graphene. *Science*, 372(6539):264–271, 2021.

[79] Kyounghwan Kim, Ashley DaSilva, Shengqiang Huang, Babak Fallahazad, Stefano Larentis, Takashi Taniguchi, Kenji Watanabe, Brian J. LeRoy, Allan H. MacDonald, and Emanuel Tutuc. Tunable moiré bands and strong correlations in small-twist-angle bilayer graphene. *Proceedings of the National Academy of Sciences*, 114(13):3364–3369, 2017.

[80] Xiaobo Lu, Petr Stepanov, Wei Yang, Ming Xie, Mohammed Ali Aamir, Ipsita Das, Carles Urgell, Kenji Watanabe, Takashi Taniguchi, Guangyu Zhang, Adrian Bachtold, Allan H. MacDonald, and Dmitri K. Efetov. Superconductors, orbital magnets and correlated states in magic-angle bilayer graphene. *Nature*, 574(7780):653–657, 2019.

[81] A. Uri, S. Grover, Y. Cao, J. A. Crosse, K. Bagani, D. Rodan-Legrain, Y. Myasoedov, K. Watanabe, T. Taniguchi, P. Moon, M. Koshino, P. Jarillo-Herrero, and E. Zeldov. Mapping the twist-angle disorder and landau levels in magic-angle graphene. *Nature*, 581(7806):47–52, 2020.

[82] Leon Balents, Cory R. Dean, Dmitri K. Efetov, and Andrea F. Young. Superconductivity and strong correlations in moiré flat bands. *Nature Physics*, 16(7):725–733, 2020.

[83] Dillon Wong, Kevin P. Nuckolls, Myungchul Oh, Biao Lian, Yonglong Xie, Sangjun Jeon, Kenji Watanabe, Takashi Taniguchi, B. Andrei Bernevig, and Ali Yazdani. Cascade of electronic transitions in magic-angle twisted bilayer graphene. *Nature*, 582(7811):198–202, 2020.

[84] U. Zondiner, A. Rozen, D. Rodan-Legrain, Y. Cao, R. Queiroz, T. Taniguchi, K. Watanabe, Y. Oreg, F. von Oppen, Ady Stern, E. Berg, P. Jarillo-Herrero, and S. Ilani. Cascade of phase transitions and dirac revivals in magic-angle graphene. *Nature*, 582(7811):203–208, 2020.

[85] Petr Stepanov, Ipsita Das, Xiaobo Lu, Ali Fahimniya, Kenji Watanabe, Takashi Taniguchi, Frank H. L. Koppens, Johannes Lischner, Leonid Levitov, and Dmitri K. Efetov. Untying the insulating and superconducting orders in magic-angle graphene. *Nature*, 583(7816):375–378, 2020.

[86] Shuang Wu, Zhenyuan Zhang, K. Watanabe, T. Taniguchi, and Eva Y. Andrei. Chern insulators, van hove singularities and topological flat bands in magic-angle twisted bilayer graphene. *Nature Materials*, 20(4):488–494, 2021.

[87] Ipsita Das, Xiaobo Lu, Jonah Herzog-Arbeitman, Zhi-Da Song, Kenji Watanabe, Takashi Taniguchi, B. Andrei Bernevig, and Dmitri K. Efetov. Symmetry-broken chern insulators and rashba-like landau-level crossings in magic-angle bilayer graphene. *Nature Physics*, 17(6):710–714, 2021.

[88] Petr Stepanov, Ming Xie, Takashi Taniguchi, Kenji Watanabe, Xiaobo Lu, Allan H. MacDonald, B. Andrei Bernevig, and Dmitri K. Efetov. Competing zero-field chern insulators in superconducting twisted bilayer graphene. *Phys. Rev. Lett.*, 127:197701, 2021.

[89] Asaf Rozen, Jeong Min Park, Uri Zondiner, Yuan Cao, Daniel Rodan-Legrain, Takashi Taniguchi, Kenji Watanabe, Yuval Oreg, Ady Stern, Erez Berg, Pablo Jarillo-Herrero, and Shahal Ilani. Entropic evidence for a pomeranchuk effect in magic-angle graphene. *Nature*, 592(7853):214–219, 2021.

[90] Yu Saito, Jingyuan Ge, Kenji Watanabe, Takashi Taniguchi, and Andrea F. Young. Independent superconductors and correlated insulators in twisted bilayer graphene. *Nature Physics*, 16(9):926–930, 2020.

[91] J. M. B. Lopes dos Santos, N. M. R. Peres, and A. H. Castro Neto. Graphene bilayer with a twist: Electronic structure. *Phys. Rev. Lett.*, 99:256802, 2007.

[92] B. Andrei Bernevig, Zhi-Da Song, Nicolas Regnault, and Biao Lian. Twisted bilayer graphene. i. matrix elements, approximations, perturbation theory, and a $k \cdot p$ two-band model. *Phys. Rev. B*, 103:205411, 2021.

[93] Zhi-Da Song, Biao Lian, Nicolas Regnault, and B. Andrei Bernevig. Twisted bilayer graphene. ii. stable symmetry anomaly. *Phys. Rev. B*, 103:205412, 2021.

[94] B. Andrei Bernevig, Zhi-Da Song, Nicolas Regnault, and Biao Lian. Twisted bilayer graphene. iii. interacting hamiltonian and exact symmetries. *Phys. Rev. B*, 103:205413, 2021.

[95] Biao Lian, Zhi-Da Song, Nicolas Regnault, Dmitri K. Efetov, Ali Yazdani, and B. Andrei Bernevig. Twisted bilayer graphene. iv. exact insulator ground states and phase diagram. *Phys. Rev. B*, 103:205414, 2021.

[96] B. Andrei Bernevig, Biao Lian, Aditya Cowsik, Fang Xie, Nicolas Regnault, and Zhi-Da Song. Twisted bilayer graphene. v. exact analytic many-body excitations in coulomb hamiltonians: Charge gap, goldstone modes, and absence of cooper pairing. *Phys. Rev. B*, 103:205415, 2021.

[97] Jian Kang and Oskar Vafek. Non-abelian dirac node braiding and near-degeneracy of correlated phases at odd integer filling in magic-angle twisted bilayer graphene. *Phys. Rev. B*, 102:035161, 2020.

[98] Jeil Jung, Arnaud Raoux, Zhenhua Qiao, and A. H. MacDonald. Ab initio theory of moiré superlattice bands in layered two-dimensional materials. *Phys. Rev. B*, 89:205414, 2014.

[99] Hoi Chun Po, Liujun Zou, Ashvin Vishwanath, and T. Senthil. Origin of mott insulating behavior and superconductivity in twisted bilayer graphene. *Phys. Rev. X*, 8:031089, 2018.

[100] Noah F. Q. Yuan and Liang Fu. Model for the metal-insulator transition in graphene superlattices and beyond. *Phys. Rev. B*, 98:045103, 2018.

[101] Huaiming Guo, Xingchuan Zhu, Shiping Feng, and Richard T. Scalettar. Pairing symmetry of interacting fermions on a twisted bilayer graphene superlattice. *Phys. Rev. B*, 97:235453, 2018.

[102] Ming Xie and A. H. MacDonald. Weak-field hall resistivity and spin-valley flavor symmetry breaking in magic-angle twisted bilayer graphene. *Phys. Rev. Lett.*, 127:196401, 2021.

[103] Fang Xie, Aditya Cowsik, Zhi-Da Song, Biao Lian, B. Andrei Bernevig, and Nicolas Regnault. Twisted bilayer graphene. vi. an exact diagonalization study at nonzero integer filling. *Phys. Rev. B*, 103:205416, 2021.

[104] Pawel Potasz, Ming Xie, and A. H. MacDonald. Exact diagonalization for magic-angle twisted bilayer graphene. *Phys. Rev. Lett.*, 127:147203, 2021.

[105] J. F. Dodaro, S. A. Kivelson, Y. Schattner, X. Q. Sun, and C. Wang. Phases of a phenomenological model of twisted bilayer graphene. *Phys. Rev. B*, 98:075154, 2018.

[106] Cheng-Cheng Liu, Li-Da Zhang, Wei-Qiang Chen, and Fan Yang. Chiral spin density wave and $d+id$ superconductivity in the magic-angle-twisted bilayer graphene. *Phys. Rev. Lett.*, 121:217001, 2018.

[107] Xiao Yan Xu, K. T. Law, and Patrick A. Lee. Kekulé valence bond order in an extended hubbard model on the honeycomb lattice with possible applications to twisted bilayer graphene. *Phys. Rev. B*, 98:121406, 2018.

[108] Louk Rademaker and Paula Mellado. Charge-transfer insulation in twisted bilayer graphene. *Phys. Rev. B*, 98:235158, 2018.

[109] Mikito Koshino, Noah F. Q. Yuan, Takashi Koretsune, Masayuki Ochi, Kazuhiko Kuroki, and Liang Fu. Maximally localized wannier orbitals and the extended hubbard model for twisted bilayer graphene. *Phys. Rev. X*, 8:031087, 2018.

[110] Alex Thomson, Shubhayu Chatterjee, Subir Sachdev, and Mathias S. Scheurer. Triangular antiferromagnetism on the honeycomb lattice of twisted bilayer graphene. *Phys. Rev. B*, 98:075109, 2018.

[111] Francisco Guinea and Niels R. Walet. Electrostatic effects, band distortions, and superconductivity in twisted graphene bilayers. *Proceedings of the National Academy of Sciences*, 115(52):13174–13179, 2018.

[112] Masayuki Ochi, Mikito Koshino, and Kazuhiko Kuroki. Possible correlated insulating states in magic-angle twisted bilayer graphene under strongly competing interactions. *Phys. Rev. B*, 98:081102, 2018.

[113] Hiroki Isobe, Noah F. Q. Yuan, and Liang Fu. Unconventional superconductivity and density waves in twisted bilayer graphene. *Phys. Rev. X*, 8:041041, 2018.

[114] Cenke Xu and Leon Balents. Topological superconductivity in twisted multilayer graphene. *Phys. Rev. Lett.*, 121:087001, 2018.

[115] Fengcheng Wu, A. H. MacDonald, and Ivar Martin. Theory of phonon-mediated superconductivity in twisted bilayer graphene. *Phys. Rev. Lett.*, 121:257001, 2018.

[116] Teemu J. Peltonen, Risto Ojajärvi, and Tero T. Heikkilä. Mean-field theory for superconductivity in twisted bilayer graphene. *Phys. Rev. B*, 98:220504, 2018.

[117] M. Fidrysiak, M. Zegrodnik, and J. Spałek. Unconventional topological superconductivity and phase diagram for an effective two-orbital model as applied to twisted bilayer graphene. *Phys. Rev. B*, 98:085436, 2018.

[118] J M Pizarro, M J Calderón, and E Bascones. The nature of correlations in the insulating states of twisted bilayer graphene. *Journal of Physics Communications*, 3(3):035024, 2019.

[119] Jian Kang and Oskar Vafek. Strong coupling phases of partially filled twisted bilayer graphene narrow bands. *Phys. Rev. Lett.*, 122:246401, 2019.

[120] Jianpeng Liu, Junwei Liu, and Xi Dai. Pseudo landau level representation of twisted bilayer graphene: Band topology and implications on the correlated insulating phase. *Phys. Rev. B*, 99:155415, 2019.

[121] Bitan Roy and Vladimir Juričić. Unconventional superconductivity in nearly flat bands in twisted bilayer graphene. *Phys. Rev. B*, 99:121407, 2019.

[122] Sujay Ray, Jeil Jung, and Tanmoy Das. Wannier pairs in superconducting twisted bilayer graphene and related systems. *Phys. Rev. B*, 99:134515, 2019.

[123] Yi-Zhuang You and Ashvin Vishwanath. Superconductivity from valley fluctuations and approximate so(4) symmetry in a weak coupling theory of twisted bilayer graphene. *npj Quantum Materials*, 4(1):16, 2019.

[124] Grigory Tarnopolsky, Alex Jura Kruchkov, and Ashvin Vishwanath. Origin of magic angles in twisted bilayer graphene. *Phys. Rev. Lett.*, 122:106405, 2019.

[125] Ya-Hui Zhang, Dan Mao, Yuan Cao, Pablo Jarillo-Herrero, and T. Senthil. Nearly flat chern bands in moiré superlattices. *Phys. Rev. B*, 99:075127, 2019.

[126] J. M. Pizarro, M. Rösner, R. Thomale, R. Valentí, and T. O. Wehling. Internal screening and dielectric engineering in magic-angle twisted bilayer graphene. *Phys. Rev. B*, 100:161102, 2019.

[127] Yuan Da Liao, Zi Yang Meng, and Xiao Yan Xu. Valence bond orders at charge neutrality in a possible two-orbital extended hubbard model for twisted bilayer graphene. *Phys. Rev. Lett.*, 123:157601, 2019.

[128] Zhida Song, Zhijun Wang, Wujun Shi, Gang Li, Chen Fang, and B. Andrei Bernevig. All magic angles in twisted bilayer graphene are topological. *Phys. Rev. Lett.*, 123:036401, 2019.

[129] Jianpeng Liu, Zhen Ma, Jinhua Gao, and Xi Dai. Quantum valley hall effect, orbital magnetism, and anomalous hall effect in twisted multilayer graphene systems. *Phys. Rev. X*, 9:031021, 2019.

[130] Nick Bultinck, Eslam Khalaf, Shang Liu, Shubhayu Chatterjee, Ashvin Vishwanath, and Michael P. Zaletel. Ground state and hidden symmetry of magic-angle graphene at even integer filling. *Phys. Rev. X*, 10:031034, 2020.

[131] Yu Zhang, Zhe Hou, Ya-Xin Zhao, Zi-Han Guo, Yi-Wen Liu, Si-Yu Li, Ya-Ning Ren, Qing-Feng Sun, and Lin He. Correlation-induced valley splitting and orbital magnetism in a strain-induced zero-energy flatband in twisted bilayer graphene near the magic angle. *Phys. Rev. B*, 102:081403, 2020.

[132] Ming Xie and A. H. MacDonald. Nature of the correlated insulator states in twisted bilayer graphene. *Phys. Rev. Lett.*, 124:097601, 2020.

[133] Oskar Vafek and Jian Kang. Renormalization group study of hidden symmetry in twisted bilayer graphene with coulomb interactions. *Phys. Rev. Lett.*, 125:257602, 2020.

[134] Cécile Repellin, Zhihuan Dong, Ya-Hui Zhang, and T. Senthil. Ferromagnetism in narrow bands of moiré superlattices. *Phys. Rev. Lett.*, 124:187601, 2020.

[135] Tomohiro Soejima, Daniel E. Parker, Nick Bultinck, Johannes Hauschild, and Michael P. Zaletel. Efficient simulation of moiré materials using the density matrix renormalization group. *Phys. Rev. B*, 102:205111, 2020.

[136] Daniel E. Parker, Tomohiro Soejima, Johannes Hauschild, Michael P. Zaletel, and Nick Bultinck. Strain-induced quantum phase transitions in magic-angle graphene. *Phys. Rev. Lett.*, 127:027601, 2021.

[137] Ajesh Kumar, Ming Xie, and A. H. MacDonald. Lattice collective modes from a continuum model of magic-angle twisted bilayer graphene. *Phys. Rev. B*, 104:035119, 2021.

[138] Patrick J. Ledwith, Eslam Khalaf, and Ashvin Vishwanath. Strong coupling theory of magic-angle graphene: A pedagogical introduction. *Annals of Physics*, 435:168646, 2021.

[139] Y. H. Kwan, G. Wagner, T. Soejima, M. P. Zaletel, S. H. Simon, S. A. Parameswaran, and N. Bultinck. Kekulé spiral order at all nonzero integer fillings in twisted bilayer graphene. *Phys. Rev. X*, 11:041063, 2021.

[140] Javad Vahedi, Robert Peters, Ahmed Missaoui, Andreas Honecker, and Guy Trambly de Laissardiere. Magnetism of magic-angle twisted bilayer graphene. *SciPost Phys.*, 11:083, 2021.

[141] Cyprian Lewandowski, Stevan Nadj-Perge, and Debanjan Chowdhury. Does filling-dependent band renormalization aid pairing in twisted bilayer graphene? *npj Quantum Materials*, 6(1):82, 2021.

[142] Bin-Bin Chen, Yuan Da Liao, Ziyu Chen, Oskar Vafek, Jian Kang, Wei Li, and Zi Yang Meng. Realization of topological mott insulator in a twisted bilayer graphene lattice model. *Nature Communications*, 12(1):5480, 2021.

[143] Shubhayu Chatterjee, Matteo Ippoliti, and Michael P. Zaletel. Skyrmion superconductivity: Dmrg evidence for a topological route to superconductivity. *Phys. Rev. B*, 106:035421, 2022.

[144] Xiaoqian Liu, Ran Peng, Zhaoru Sun, and Jianpeng Liu. Moiré phonons in magic-angle twisted bilayer graphene. *Nano Letters*, 22(19):7791–7797, 2022.

[145] Mariya Romanova and Vojtěch Vlček. Stochastic many-body calculations of moiré states in twisted bilayer graphene at high pressures. *npj Computational Materials*, 8(1):11, 2022.

[146] Shihao Zhang, Xin Lu, and Jianpeng Liu. Correlated insulators, density wave states, and their nonlinear optical response in magic-angle twisted bilayer graphene. *Phys. Rev. Lett.*, 128:247402, 2022.

[147] Dmitry V. Chichinadze, Laura Classen, Yuxuan Wang, and Andrey V. Chubukov. Su(4) symmetry in twisted bilayer graphene: An itinerant perspective. *Phys. Rev. Lett.*, 128:227601, 2022.

[148] Héctor Ochoa and Rafael M. Fernandes. Degradation of phonons in disordered moiré superlattices. *Phys. Rev. Lett.*, 128:065901, 2022.

[149] Yves H. Kwan, Glenn Wagner, Nick Bultinck, Steven H. Simon, and S. A. Parameswaran. Skyrmions in twisted bilayer graphene: Stability, pairing, and crystallization. *Phys. Rev. X*, 12:031020, 2022.

[150] Johannes S. Hofmann, Eslam Khalaf, Ashvin Vishwanath, Erez Berg, and Jong Yeon Lee. Fermionic monte carlo study of a realistic model of twisted bilayer graphene. *Phys. Rev. X*, 12:011061, 2022.

[151] Zhi-Da Song and B. Andrei Bernevig. Magic-angle twisted bilayer graphene as a topological heavy fermion problem. *Phys. Rev. Lett.*, 129:047601, 2022.

[152] Frank Schindler, Oskar Vafek, and B. Andrei Bernevig. Trions in twisted bilayer graphene. *Phys. Rev. B*, 105:155135, 2022.

[153] Zhaoyu Han and Steven A. Kivelson. Pair density wave and reentrant superconducting tendencies originating from valley polarization. *Phys. Rev. B*, 105:L100509, 2022.

[154] Dumitru Călugăru, Nicolas Regnault, Myungchul Oh, Kevin P. Nuckolls, Dillon Wong, Ryan L. Lee, Ali Yazdani, Oskar Vafek, and B. Andrei Bernevig. Spectroscopy of twisted bilayer graphene correlated insulators. *Phys. Rev. Lett.*, 129:117602, 2022.

[155] Jung Pyo Hong, Tomohiro Soejima, and Michael P. Zaletel. Detecting symmetry breaking in magic angle graphene using scanning tunneling microscopy. *Phys. Rev. Lett.*, 129:147001, 2022.

[156] Clara N. Breiø and Brian M. Andersen. Chern insulator phases and spontaneous spin and valley order in a moiré lattice model for magic-angle twisted bilayer graphene. *Phys. Rev. B*, 107:165114, 2023.

[157] Yuncheng Mao, Daniele Guerci, and Christophe Mora. Supermoiré low-energy effective theory of twisted trilayer graphene. *Phys. Rev. B*, 107:125423, 2023.

[158] Fang Xie, Jian Kang, B. Andrei Bernevig, Oskar Vafek, and Nicolas Regnault. Phase diagram of twisted bilayer graphene at filling factor $\nu = \pm 3$. *Phys. Rev. B*, 107:075156, 2023.

[159] Erin Morissette, Jiang-Xiazi Lin, Dihao Sun, Liangji Zhang, Song Liu, Daniel Rhodes, Kenji Watanabe, Takashi Taniguchi, James Hone, Johannes Pollanen, Mathias S. Scheurer, Michael Lilly, Andrew Mounce, and J. I. A. Li. Dirac revivals drive a resonance response in twisted bilayer graphene. *Nature Physics*, 19(8):1156–1162, 2023.

[160] Gaopei Pan, Xu Zhang, Hongyu Lu, Heqiu Li, Bin-Bin Chen, Kai Sun, and Zi Yang Meng. Thermodynamic characteristic for a correlated flat-band system with a quantum anomalous hall ground state. *Phys. Rev. Lett.*, 130:016401, 2023.

[161] Ipsita Mandal and Rafael M. Fernandes. Valley-polarized nematic order in twisted moiré systems: In-plane orbital magnetism and crossover from non-fermi liquid to fermi liquid. *Phys. Rev. B*, 107:125142, 2023.

[162] SK Firoz Islam, A. Yu. Zyuzin, and Alexander A. Zyuzin. Unconventional superconductivity with preformed pairs in twisted bilayer graphene. *Phys. Rev. B*, 107:L060503, 2023.

[163] E. Suárez Morell, J. D. Correa, P. Vargas, M. Pacheco, and Z. Barticevic. Flat bands in slightly twisted bilayer graphene: Tight-binding calculations. *Phys. Rev. B*, 82:121407, 2010.

[164] Jian Kang and Oskar Vafek. Symmetry, maximally localized wannier states, and a low-energy model for twisted bilayer graphene narrow bands. *Phys. Rev. X*, 8:031088, 2018.

[165] Bikash Padhi, Chandan Setty, and Philip W. Phillips. Doped twisted bilayer graphene near magic angles: Proximity to wigner crystallization, not mott insulation. *Nano Letters*, 18(10):6175–6180, 2018.

[166] Xiang Hu, Timo Hyart, Dmitry I. Pikulin, and Enrico Rossi. Geometric and conventional contribution to the superfluid weight in twisted bilayer graphene. *Phys. Rev. Lett.*, 123:237002, 2019.

[167] Justin H. Wilson, Yixing Fu, S. Das Sarma, and J. H. Pixley. Disorder in twisted bilayer graphene. *Phys. Rev. Res.*, 2:023325, 2020.

[168] Fang Xie, Zhida Song, Biao Lian, and B. Andrei Bernevig. Topology-bounded superfluid weight in twisted bilayer graphene. *Phys. Rev. Lett.*, 124:167002, 2020.

[169] Kasra Hejazi, Xiao Chen, and Leon Balents. Hybrid wannier chern bands in magic angle twisted bilayer graphene and the quantized anomalous hall effect. *Phys. Rev. Res.*, 3:013242, 2021.

[170] Bikash Padhi, Apoorv Tiwari, Titus Neupert, and Shinsei Ryu. Transport across twist angle domains in moiré graphene. *Phys. Rev. Res.*, 2:033458, 2020.

[171] Nick Bultinck, Shubhayu Chatterjee, and Michael P. Zaletel. Mechanism for anomalous hall ferromagnetism in twisted bilayer graphene. *Phys. Rev. Lett.*, 124:166601, 2020.

[172] Shubhayu Chatterjee, Nick Bultinck, and Michael P. Zaletel. Symmetry breaking and skyrmionic transport in twisted bilayer graphene. *Phys. Rev. B*, 101:165141, 2020.

[173] A. Julku, T. J. Peltonen, L. Liang, T. T. Heikkilä, and P. Törmä. Superfluid weight and berezinskii-kosterlitz-thouless transition temperature of twisted bilayer graphene. *Phys. Rev. B*, 101:060505, 2020.

[174] Yves H. Kwan, Glenn Wagner, Nilotpal Chakraborty, Steven H. Simon, and S. A. Parameswaran. Domain wall competition in the chern insulating regime of twisted bilayer graphene. *Phys. Rev. B*, 104:115404, 2021.

[175] Shang Liu, Eslam Khalaf, Jong Yeon Lee, and Ashvin Vishwanath. Nematic topological semimetal and insulator in magic-angle bilayer graphene at charge neutrality. *Phys. Rev. Res.*, 3:013033, 2021.

[176] Eslam Khalaf, Shubhayu Chatterjee, Nick Bultinck, Michael P. Zaletel, and Ashvin Vishwanath. Charged skyrmions and topological origin of superconductivity in magic-angle graphene. *Science Advances*, 7(19):eabf5299, 2021.

[177] Valerio Peri, Zhi-Da Song, B. Andrei Bernevig, and Sebastian D. Huber. Fragile topology and flat-band superconductivity in the strong-coupling regime. *Phys. Rev. Lett.*, 126:027002, 2021.

[178] Cheng Huang, Xu Zhang, Gaopei Pan, Heqiu Li, Kai Sun, Xi Dai, and Zi Yang Meng. Evolution from quantum anomalous hall insulator to heavy-fermion semimetal in twisted bilayer graphene. *arXiv:*, 2023.

[179] Fabian M. Faulstich, Kevin D. Stubbs, Qinyi Zhu, Tomohiro Soejima, Rohit Dilip, Huanchen Zhai, Raehyun Kim, Michael P. Zaletel, Garnet Kin-Lic Chan, and Lin Lin. Interacting models for twisted bilayer graphene: A quantum chemistry approach. *Phys. Rev. B*, 107:235123, 2023.

[180] Kevin P. Nuckolls and Ali Yazdani. A microscopic perspective on moiré materials. *Nature Reviews Materials*, 9(7):460–480, 2024.

[181] Yu Saito, Jingyuan Ge, Louk Rademaker, Kenji Watanabe, Takashi Taniguchi, Dmitry A. Abanin, and Andrea F. Young. Hofstadter subband ferromagnetism and symmetry-broken chern insulators in twisted bilayer graphene. *Nature Physics*, 17(4):478–481, 2021.

[182] Kevin P. Nuckolls, Myungchul Oh, Dillon Wong, Biao Lian, Kenji Watanabe, Takashi Taniguchi, B. Andrei Bernevig, and Ali Yazdani. Strongly correlated chern insulators in magic-angle twisted bilayer graphene. *Nature*, 588(7839):610–615, 2020.

[183] Glenn Wagner, Yves H. Kwan, Nick Bultinck, Steven H. Simon, and S. A. Parameswaran. Global phase diagram of the normal state of twisted bilayer graphene. *Phys. Rev. Lett.*, 128:156401, 2022.

[184] Jiachen Yu, Benjamin A. Foutty, Zhaoyu Han, Mark E. Barber, Yoni Schattner, Kenji Watanabe, Takashi Taniguchi, Philip Phillips, Zhi-Xun Shen, Steven A. Kivelson, and Benjamin E. Feldman. Correlated hofstadter spectrum and flavour phase diagram in magic-angle twisted bilayer graphene. *Nature Physics*, 18(7):825–831, 2022.

[185] Xianqing Lin and Jun Ni. Effective lattice model of graphene moiré superlattices on hexagonal boron nitride. *Phys. Rev. B*, 100:195413, 2019.

[186] Xianqing Lin and Jun Ni. Symmetry breaking in the double moiré superlattices of relaxed twisted bilayer graphene on hexagonal boron nitride. *Phys. Rev. B*, 102:035441, 2020.

[187] Tommaso Cea, Pierre A. Pantaleón, and Francisco Guinea. Band structure of twisted bilayer graphene on hexagonal boron nitride. *Phys. Rev. B*, 102:155136, 2020.

[188] Xianqing Lin, Kelu Su, and Jun Ni. Misalignment instability in magic-angle twisted bilayer graphene on hexagonal boron nitride. *2D Materials*, 8(2):025025, 2021.

[189] Jie Cao, Fenghua Qi, Hai Yang, and Guojun Jin. Superflat energy band induced by moiré electric potential in twisted bilayer graphene. *Phys. Rev. B*, 103:165417, 2021.

[190] Jingtian Shi, Jihang Zhu, and A. H. MacDonald. Moiré commensurability and the quantum anomalous hall effect in twisted bilayer graphene on hexagonal boron nitride. *Phys. Rev. B*, 103:075122, 2021.

[191] Dan Mao and T. Senthil. Quasiperiodicity, band topology, and moiré graphene. *Phys. Rev. B*, 103:115110, 2021.

[192] Jiseon Shin, Youngju Park, Bheema Lingam Chittari, Jin-Hua Sun, and Jeil Jung. Electron-hole asymmetry and band gaps of commensurate double moire patterns in twisted bilayer graphene on hexagonal boron nitride. *Phys. Rev. B*, 103:075423, 2021.

[193] Min Long, Pierre A. Pantaleón, Zhen Zhan, Francisco Guinea, Jose Ángel Silva-Guillén, and Shengjun Yuan. An atomistic approach for the structural and electronic properties of twisted bilayer graphene-boron nitride heterostructures. *npj Computational Materials*, 8(1):73, 2022.

[194] Yiheng Chen, Wen-Ti Guo, Zi-Si Chen, Suyun Wang, and Jian-Min Zhang. First-principles study on the heterostructure of twisted graphene/hexagonal boron nitride/graphene sandwich structure. *Journal of Physics: Condensed Matter*, 34(12):125504, 2022.

[195] Min Long, Zhen Zhan, Pierre A. Pantaleón, Jose Ángel Silva-Guillén, Francisco Guinea, and Shengjun Yuan. Electronic properties of twisted bilayer graphene suspended and encapsulated with hexagonal boron nitride. *Phys. Rev. B*, 107:115140, 2023.

[196] Xianqing Lin, Quan Zhou, Cheng Li, and Jun Ni. Collective excitations of the chern-insulator states in commensurate double moiré superlattices of twisted bilayer graphene on hexagonal boron nitride. *Phys. Rev. B*, 107:195434, 2023.

[197] Procolo Lucignano, Dario Alfè, Vittorio Cataudella, Domenico Ninno, and Giovanni Cantele. Crucial role of atomic corrugation on the flat bands and energy gaps of twisted bilayer graphene at the magic angle $\theta \sim 1.08^\circ$. *Phys. Rev. B*, 99:195419, 2019.

[198] G. Trambly de Laissardière, D. Mayou, and L. Magaud. Localization of dirac electrons in rotated graphene bilayers. *Nano Letters*, 10(3):804–808, 2010.

[199] Alexander Kerelsky, Leo J. McGilly, Dante M. Kennes, Lede Xian, Matthew Yankowitz, Shaowen Chen, K. Watanabe, T. Taniguchi, James Hone, Cory Dean, Angel Rubio, and Abhay N. Pasupathy. Maximized electron interactions at the magic angle in twisted bilayer graphene. *Nature*, 572(7767):95–100, 2019.

[200] Yasumasa Hasegawa and Mahito Kohmoto. Periodic landau gauge and quantum hall effect in twisted bilayer graphene. *Phys. Rev. B*, 88:125426, 2013.

[201] Manato Fujimoto and Mikito Koshino. Moiré edge states in twisted bilayer graphene and their topological relation to quantum pumping. *Phys. Rev. B*, 103:155410, 2021.

[202] Elias Andrade, Pierre A. Pantaleón, Francisco Guinea, and Gerardo G. Naumis. Flat bands and electronic localization in twisted bilayer graphene nanoribbons. *Phys. Rev. B*, 108:235418, 2023.

[203] Hoi Chun Po, Liujun Zou, T. Senthil, and Ashvin Vishwanath. Faithful tight-binding models and fragile topology of magic-angle bilayer graphene. *Phys. Rev. B*, 99:195455, 2019.

[204] Hao Shi and Xi Dai. Heavy-fermion representation for twisted bilayer graphene systems. *Phys. Rev. B*, 106:245129, 2022.

[205] Keshav Singh, Aaron Chew, Jonah Herzog-Arbeitman, B. Andrei Bernevig, and Oskar Vafek. Topological heavy fermions in magnetic field. *arXiv:*, 2023.

[206] S. L. Tomarken, Y. Cao, A. Demir, K. Watanabe, T. Taniguchi, P. Jarillo-Herrero, and R. C. Ashoori. Electronic compressibility of magic-angle graphene superlattices. *Phys. Rev. Lett.*, 123:046601, 2019.

[207] Harpreet Singh Arora, Robert Polski, Yiran Zhang, Alex Thomson, Youngjoon Choi, Hyunjin Kim, Zhong Lin, Ilham Zaky Wilson, Xiaodong Xu, Jiun-Haw Chu, Kenji Watanabe, Takashi Taniguchi, Jason Alicea, and Stevan Nadj-Perge. Superconductivity in metallic twisted bilayer graphene stabilized by wse2. *Nature*, 583(7816):379–384, 2020.

[208] Youngjoon Choi, Hyunjin Kim, Yang Peng, Alex Thomson, Cyprian Lewandowski, Robert Polski, Yiran Zhang, Harpreet Singh Arora, Kenji Watanabe, Takashi Taniguchi, Jason Alicea, and Stevan Nadj-Perge. Correlation-driven topological phases in magic-angle twisted bilayer graphene. *Nature*, 589(7843):536–541, 2021.

[209] Xiaoxue Liu, Zhi Wang, K. Watanabe, T. Taniguchi, Oskar Vafek, and J. I. A. Li. Tuning electron correlation in magic-angle twisted bilayer graphene using coulomb screening. *Science*, 371(6535):1261–1265, 2021.

[210] Yonglong Xie, Andrew T. Pierce, Jeong Min Park, Daniel E. Parker, Eslam Khalaf, Patrick Ledwith, Yuan Cao, Seung Hwan Lee, Shaowen Chen, Patrick R. Forrester, Kenji Watanabe, Takashi Taniguchi, Ashvin Vishwanath, Pablo Jarillo-Herrero, and Amir Yacoby. Fractional chern insulators in magic-angle twisted bilayer graphene. *Nature*, 600(7889):439–443, 2021.

[211] Jeong Min Park, Yuan Cao, Kenji Watanabe, Takashi Taniguchi, and Pablo Jarillo-Herrero. Flavour hund's coupling, chern gaps and charge diffusivity in moiré graphene. *Nature*, 592(7852):43–48, 2021.

[212] Jiang-Xiazi Lin, Ya-Hui Zhang, Erin Morissette, Zhi Wang, Song Liu, Daniel Rhodes, K. Watanabe, T. Taniguchi, James Hone, and J. I. A. Li. Spin orbit driven ferro-

magnetism at half moire filling in magic-angle twisted bilayer graphene. *Science*, 375(6579):437–441, 2022.

[213] Saisab Bhowmik, Bhaskar Ghawri, Nicolas Leconte, Samudrala Appalakondaiah, Mrityunjay Pandey, Phanibhusan S. Mahapatra, Dongkyu Lee, K. Watanabe, T. Taniguchi, Jeil Jung, Arindam Ghosh, and U. Chandni. Broken-symmetry states at half-integer band fillings in twisted bilayer graphene. *Nature Physics*, 18(6):639–643, 2022.

[214] Ipsita Das, Cheng Shen, Alexandre Jaoui, Jonah Herzog-Arbeitman, Aaron Chew, Chang-Woo Cho, Kenji Watanabe, Takashi Taniguchi, Benjamin A. Piot, B. Andrei Bernevig, and Dmitri K. Efetov. Observation of reentrant correlated insulators and interaction-driven fermi-surface reconstructions at one magnetic flux quantum per moiré unit cell in magic-angle twisted bilayer graphene. *Phys. Rev. Lett.*, 128:217701, 2022.

[215] Robert Polski, Yiran Zhang, Yang Peng, Harpreet Singh Arora, Youngjoon Choi, Hyunjin Kim, Kenji Watanabe, Takashi Taniguchi, Gil Refael, Felix von Oppen, and Stevan Nadj-Perge. Hierarchy of symmetry breaking correlated phases in twisted bilayer graphene. *arXiv:*, 2022.

[216] Chun-Chih Tseng, Xuetao Ma, Zhaoyu Liu, Kenji Watanabe, Takashi Taniguchi, Jiun-Haw Chu, and Matthew Yankowitz. Anomalous hall effect at half filling in twisted bilayer graphene. *Nature Physics*, 18(9):1038–1042, 2022.

[217] Sameer Grover, Matan Bocarsly, Aviram Uri, Petr Stepanov, Giorgio Di Battista, Indranil Roy, Jiewen Xiao, Alexander Y. Meltzer, Yuri Myasoedov, Keshav Pareek, Kenji Watanabe, Takashi Taniguchi, Binghai Yan, Ady Stern, Erez Berg, Dmitri K. Efetov, and Eli Zeldov. Chern mosaic and berry-curvature magnetism in magic-angle graphene. *Nature Physics*, 18(8):885–892, 2022.

[218] J. Díez-Mérida, A. Díez-Carlón, S. Y. Yang, Y.-M. Xie, X.-J. Gao, J. Senior, K. Watanabe, T. Taniguchi, X. Lu, A. P. Higginbotham, K. T. Law, and Dmitri K.

Efetov. Symmetry-broken josephson junctions and superconducting diodes in magic-angle twisted bilayer graphene. *Nature Communications*, 14(1):2396, 2023.

[219] Haidong Tian, Xueshi Gao, Yuxin Zhang, Shi Che, Tianyi Xu, Patrick Cheung, Kenji Watanabe, Takashi Taniguchi, Mohit Randeria, Fan Zhang, Chun Ning Lau, and Marc W. Bockrath. Evidence for dirac flat band superconductivity enabled by quantum geometry. *Nature*, 614(7948):440–444, 2023.

[220] P Streda. Theory of quantised hall conductivity in two dimensions. *Journal of Physics C: Solid State Physics*, 15(22):L717, 1982.

[221] Min-Young Choi, Young-Hwan Hyun, and Yoonbai Kim. Angle dependence of the landau level spectrum in twisted bilayer graphene. *Phys. Rev. B*, 84:195437, 2011.

[222] Ya-Hui Zhang, Hoi Chun Po, and T. Senthil. Landau level degeneracy in twisted bilayer graphene: Role of symmetry breaking. *Phys. Rev. B*, 100:125104, 2019.

[223] Kasra Hejazi, Chunxiao Liu, and Leon Balents. Landau levels in twisted bilayer graphene and semiclassical orbits. *Phys. Rev. B*, 100:035115, 2019.

[224] Biao Lian, Fang Xie, and B. Andrei Bernevig. Landau level of fragile topology. *Phys. Rev. B*, 102:041402, 2020.

[225] Jonah Herzog-Arbeitman, Zhi-Da Song, Nicolas Regnault, and B. Andrei Bernevig. Hofstadter topology: Noncrystalline topological materials at high flux. *Phys. Rev. Lett.*, 125:236804, 2020.

[226] Bartholomew Andrews and Alexey Soluyanov. Fractional quantum hall states for moiré superstructures in the hofstadter regime. *Phys. Rev. B*, 101:235312, 2020.

[227] Yarden Sheffer and Ady Stern. Chiral magic-angle twisted bilayer graphene in a magnetic field: Landau level correspondence, exact wave functions, and fractional chern insulators. *Phys. Rev. B*, 104:L121405, 2021.

[228] Biao Lian, Fang Xie, and B. Andrei Bernevig. Open momentum space method for the hofstadter butterfly and the quantized lorentz susceptibility. *Phys. Rev. B*, 103:L161405, 2021.

[229] Jian Kang, B. Andrei Bernevig, and Oskar Vafek. Cascades between light and heavy fermions in the normal state of magic-angle twisted bilayer graphene. *Phys. Rev. Lett.*, 127:266402, 2021.

[230] Yoonseok Hwang, Jun-Won Rhim, and Bohm-Jung Yang. Geometric characterization of anomalous landau levels of isolated flat bands. *Nature Communications*, 12(1):6433, 2021.

[231] Nadia Benlakhouy, Ahmed Jellal, Hocine Bahlouli, and Michael Vogl. Chiral limits and effect of light on the hofstadter butterfly in twisted bilayer graphene. *Phys. Rev. B*, 105:125423, 2022.

[232] Yifei Guan, Adrien Bouhon, and Oleg V. Yazyev. Landau levels of the euler class topology. *Phys. Rev. Res.*, 4:023188, 2022.

[233] Thi-Nga Do, Po-Hsin Shih, Hsin Lin, Danhong Huang, Godfrey Gumbs, and Tay-Rong Chang. Generalized peierls substitution for the tight-binding model of twisted graphene systems in a magnetic field. *Phys. Rev. B*, 105:235418, 2022.

[234] Jonah Herzog-Arbeitman, Aaron Chew, and B. Andrei Bernevig. Magnetic bloch theorem and reentrant flat bands in twisted bilayer graphene at 2π flux. *Phys. Rev. B*, 106:085140, 2022.

[235] Jonah Herzog-Arbeitman, Aaron Chew, Dmitri K. Efetov, and B. Andrei Bernevig. Reentrant correlated insulators in twisted bilayer graphene at 25 t (2π flux). *Phys. Rev. Lett.*, 129:076401, 2022.

[236] Nisarga Paul, Philip J. D. Crowley, Trithep Devakul, and Liang Fu. Moiré landau fans and magic zeros. *Phys. Rev. Lett.*, 129:116804, 2022.

[237] Xiaoyu Wang and Oskar Vafek. Narrow bands in magnetic field and strong-coupling hofstadter spectra. *Phys. Rev. B*, 106:L121111, 2022.

[238] Leonardo A. Navarro-Labastida and Gerardo G. Naumis. 3/2 magic angle quantization rule of flat bands in twisted bilayer graphene and its relationship to the quantum hall effect. *Phys. Rev. B*, 107:155428, 2023.

[239] Jonah Herzog-Arbeitman, Zhi-Da Song, Luis Elcoro, and B. Andrei Bernevig. Hofstadter topology with real space invariants and reentrant projective symmetries. *Phys. Rev. Lett.*, 130:236601, 2023.

[240] Daniel Shaffer, Jian Wang, and Luiz H. Santos. Unconventional self-similar hofstadter superconductivity from repulsive interactions. *Nature Communications*, 13(1):7785, 2022.

[241] Pilkyung Moon and Mikito Koshino. Energy spectrum and quantum hall effect in twisted bilayer graphene. *Phys. Rev. B*, 85:195458, 2012.

[242] Yifei Guan, Oleg V. Yazyev, and Alexander Kruchkov. Reentrant magic-angle phenomena in twisted bilayer graphene in integer magnetic fluxes. *Phys. Rev. B*, 106:L121115, 2022.

[243] Eslam Khalaf, Alex J. Kruchkov, Grigory Tarnopolsky, and Ashvin Vishwanath. Magic angle hierarchy in twisted graphene multilayers. *Phys. Rev. B*, 100:085109, 2019.

[244] Stephen Carr, Chenyuan Li, Ziyan Zhu, Efthimios Kaxiras, Subir Sachdev, and Alexander Kruchkov. Ultraheavy and ultrarelativistic Dirac quasiparticles in sandwiched graphenes. *Nano Letters*, 20(5):3030–3038, 2020.

[245] Dumitru Călugăru, Fang Xie, Zhi-Da Song, Biao Lian, Nicolas Regnault, and B. Andrei Bernevig. Twisted symmetric trilayer graphene: Single-particle and many-body Hamiltonians and hidden nonlocal symmetries of trilayer moiré systems with and without displacement field. *Phys. Rev. B*, 103:195411, 2021.

[246] Chao Lei, Lukas Linhart, Wei Qin, Florian Libisch, and Allan H. MacDonald. Mirror symmetry breaking and lateral stacking shifts in twisted trilayer graphene. *Phys. Rev. B*, 104:035139, 2021.

[247] Fang Xie, Nicolas Regnault, Dumitru Călugăru, B. Andrei Bernevig, and Biao Lian. Twisted symmetric trilayer graphene. II. projected Hartree-Fock study. *Phys. Rev. B*, 104:115167, 2021.

[248] Võ Tien Phong, Pierre A. Pantaleón, Tommaso Cea, and Francisco Guinea. Band structure and superconductivity in twisted trilayer graphene. *Phys. Rev. B*, 104:L121116, 2021.

[249] Maine Christos, Subir Sachdev, and Mathias S. Scheurer. Correlated insulators, semimetals, and superconductivity in twisted trilayer graphene. *Phys. Rev. X*, 12:021018, 2022.

[250] Jiabin Yu, Ming Xie, B. Andrei Bernevig, and Sankar Das Sarma. Magic-angle twisted symmetric trilayer graphene as a topological heavy-fermion problem. *Phys. Rev. B*, 108:035129, 2023.

[251] Yiwei Li, Shihao Zhang, Fanqiang Chen, Liyang Wei, Zonglin Zhang, Hanbo Xiao, Han Gao, Moyu Chen, Shijun Liang, Ding Pei, Lixuan Xu, Kenji Watanabe, Takashi Taniguchi, Lexian Yang, Feng Miao, Jianpeng Liu, Bin Cheng, Meixiao Wang, Yulin Chen, and Zhongkai Liu. Observation of coexisting Dirac bands and moiré flat bands in magic-angle twisted trilayer graphene. *Advanced Materials*, 34(42):2205996, 2022.

[252] Hyunjin Kim, Youngjoon Choi, Cyprian Lewandowski, Alex Thomson, Yiran Zhang, Robert Polski, Kenji Watanabe, Takashi Taniguchi, Jason Alicea, and Stevan Nadj-Perge. Evidence for unconventional superconductivity in twisted trilayer graphene. *Nature*, 606(7914):494–500, 2022.

[253] Xiaoxue Liu, Naiyuan James Zhang, K. Watanabe, T. Taniguchi, and J. I. A. Li. Isospin order in superconducting magic-angle twisted trilayer graphene. *Nature Physics*, 18(5):522–527, 2022.

[254] Jeong Min Park, Yuan Cao, Li-Qiao Xia, Shuwen Sun, Kenji Watanabe, Takashi Taniguchi, and Pablo Jarillo-Herrero. Robust superconductivity in magic-angle multilayer graphene family. *Nature Materials*, 21(8):877–883, 2022.

[255] Phum Siriviboon, Jiang-Xiazi Lin, Xiaoxue Liu, Harley D. Scammell, Song Liu, Daniel Rhodes, K. Watanabe, T. Taniguchi, James Hone, Mathias S. Scheurer, and J. I. A. Li. A new flavor of correlation and superconductivity in small twist-angle trilayer graphene. *arXiv*, 2022.

[256] Cheng Shen, Patrick J. Ledwith, Kenji Watanabe, Takashi Taniguchi, Eslam Khalaf, Ashvin Vishwanath, and Dmitri K. Efetov. Dirac spectroscopy of strongly correlated phases in twisted trilayer graphene. *Nature Materials*, 22(3):316–321, 2023.

[257] Ayshi Mukherjee, Surat Layek, Subhajit Sinha, Ritajit Kundu, Alisha H. Marchawala, Mahesh Hingankar, Joydip Sarkar, L. D. Varma Sangani, Heena Agarwal, Sanat Ghosh, Aya Batoul Tazi, Kenji Watanabe, Takashi Taniguchi, Abhay N. Pasupathy, Arijit Kundu, and Mandar M. Deshmukh. Superconducting magic-angle twisted trilayer graphene hosts competing magnetic order and moiré inhomogeneities. *arXiv*, 2024.

[258] Sergi Batlle-Porro, Dumitru Calugaru, Haoyu Hu, Roshan Krishna Kumar, Niels C. H. Hesp, Kenji Watanabe, Takashi Taniguchi, B. Andrei Bernevig, Petr Stepanov, and Frank H. L. Koppens. Cryo-near-field photovoltage microscopy of heavy-fermion twisted symmetric trilayer graphene. *arXiv*, 2024.

[259] Naiyuan James Zhang, Jiang-Xiazi Lin, Dmitry V. Chichinadze, Yibang Wang, Kenji Watanabe, Takashi Taniguchi, Liang Fu, and J. I. A. Li. Angle-resolved transport non-reciprocity and spontaneous symmetry breaking in twisted trilayer graphene. *Nature Materials*, 23(3):356–362, 2024.

[260] Zekang Zhou, Jin Jiang, Paritosh Karnatak, Ziwei Wang, Glenn Wagner, Kenji Watanabe, Takashi Taniguchi, Christian Schönenberger, S. A. Parameswaran, Steven H. Simon, and Mitali Banerjee. Double-dome unconventional superconductivity in twisted trilayer graphene. *arXiv*, 2024.

[261] Ammon Fischer, Zachary A. H. Goodwin, Arash A. Mostofi, Johannes Lischner, Dante M. Kennes, and Lennart Klebl. Unconventional superconductivity in magic-angle twisted trilayer graphene. *npj Quantum Materials*, 7(1):5, 2022.

[262] Wei Qin and Allan H. MacDonald. In-plane critical magnetic fields in magic-angle twisted trilayer graphene. *Phys. Rev. Lett.*, 127:097001, 2021.

[263] Yang-Zhi Chou, Fengcheng Wu, Jay D. Sau, and Sankar Das Sarma. Correlation-induced triplet pairing superconductivity in graphene-based moiré systems. *Phys. Rev. Lett.*, 127:217001, 2021.

[264] Ethan Lake and T. Senthil. Reentrant superconductivity through a quantum Lifshitz transition in twisted trilayer graphene. *Phys. Rev. B*, 104:174505, 2021.

[265] J. González and T. Stauber. Ising superconductivity induced from spin-selective valley symmetry breaking in twisted trilayer graphene. *Nature Communications*, 14(1):2746, 2023.

[266] Rhine Samajdar, Yanting Teng, and Mathias S. Scheurer. Moiré phonons and impact of electronic symmetry breaking in twisted trilayer graphene. *Phys. Rev. B*, 106:L201403, 2022.

[267] Guorui Chen, Aaron L. Sharpe, Patrick Gallagher, Ilan T. Rosen, Eli J. Fox, Lili Jiang, Bosai Lyu, Hongyuan Li, Kenji Watanabe, Takashi Taniguchi, Jeil Jung, Zhiwen Shi, David Goldhaber-Gordon, Yuanbo Zhang, and Feng Wang. Signatures of tunable superconductivity in a trilayer graphene moiré superlattice. *Nature*, 572(7768):215–219, 2019.

[268] Guorui Chen, Aaron L. Sharpe, Eli J. Fox, Shaoxin Wang, Bosai Lyu, Lili Jiang, Hongyuan Li, Kenji Watanabe, Takashi Taniguchi, Michael F. Crommie, Marc A. Kastner, Zhiwen Shi, David Goldhaber-Gordon, Yuanbo Zhang, and Feng Wang. Tunable orbital ferromagnetism at noninteger filling of a moiré superlattice. *Nano Letters*, 22(1):238–245, 2022.

[269] Imre Hagymási, Mohammad Syahid Mohd Isa, Zoltán Tajkov, Krisztián Márity, László Oroszlány, János Koltai, Assem Alassaf, Péter Kun, Konrád Kandrai, András Pálinkás, Péter Vancsó, Levente Tapasztó, and Péter Nemes-Incze. Observation of competing, correlated ground states in the flat band of rhombohedral graphite. *Science Advances*, 8(35):eabo6879, 2022.

[270] Tonghang Han, Zhengguang Lu, Giovanni Scuri, Jiho Sung, Jue Wang, Tianyi Han, Kenji Watanabe, Takashi Taniguchi, Hongkun Park, and Long Ju. Correlated insulator and chern insulators in pentalayer rhombohedral stacked graphene, 2023.

[271] Kai Liu, Jian Zheng, Yating Sha, Bosai Lyu, Fengping Li, Youngju Park, Yulu Ren, Kenji Watanabe, Takashi Taniguchi, Jinfeng Jia, Weidong Luo, Zhiwen Shi, Jeil Jung, and Guorui Chen. Spontaneous broken-symmetry insulator and metals in tetralayer rhombohedral graphene. *Nature Nanotechnology*, 19(2):188–195, 2024.

[272] Junkai Dong, Taige Wang, Tianle Wang, Tomohiro Soejima, Michael P. Zaletel, Ashvin Vishwanath, and Daniel E. Parker. Anomalous hall crystals in rhombohedral multilayer graphene. i. interaction-driven chern bands and fractional quantum hall states at zero magnetic field. *Physical Review Letters*, 133(20), 2024.

[273] Xidong Duan, Chen Wang, Anlian Pan, Ruqin Yu, and Xiangfeng Duan. Two-dimensional transition metal dichalcogenides as atomically thin semiconductors: opportunities and challenges. *Chem. Soc. Rev.*, 44:8859–8876, 2015.

[274] Manish Chhowalla, Hyeon Suk Shin, Goki Eda, Lain-Jong Li, Kian Ping Loh, and Hua Zhang. The chemistry of two-dimensional layered transition metal dichalcogenide nanosheets. *Nature Chemistry*, 5(4):263–275, 2013.

[275] Qing Hua Wang, Kourosh Kalantar-Zadeh, Andras Kis, Jonathan N. Coleman, and Michael S. Strano. Electronics and optoelectronics of two-dimensional transition metal dichalcogenides. *Nature Nanotechnology*, 7(11):699–712, 2012.

[276] Abdulmenaf Altıntaş, Maciej Bieniek, Amintor Dusko, Marek Korkusiński, Jarosław Pawłowski, and Paweł Hawrylak. Spin-valley qubits in gated quantum dots in a single layer of transition metal dichalcogenides. *Phys. Rev. B*, 104:195412, 2021.

[277] Maciej Bieniek, Marek Korkusiński, Ludmiła Szulakowska, Paweł Potasz, Isil Ozfidan, and Paweł Hawrylak. Band nesting, massive dirac fermions, and valley landé and zeeman effects in transition metal dichalcogenides: A tight-binding model. *Phys. Rev. B*, 97:085153, 2018.

[278] Maciej Bieniek, Ludmiła Szulakowska, and Paweł Hawrylak. Effect of valley, spin, and band nesting on the electronic properties of gated quantum dots in a single layer of transition metal dichalcogenides. *Phys. Rev. B*, 101:035401, 2020.

[279] Yuichi Otsuka, Seiji Yunoki, and Sandro Sorella. Universal quantum criticality in the metal-insulator transition of two-dimensional interacting dirac electrons. *Phys. Rev. X*, 6:011029, 2016.

[280] Maciej Bieniek, Katarzyna Sadecka, Ludmiła Szulakowska, and Paweł Hawrylak. Theory of excitons in atomically thin semiconductors: Tight-binding approach. *Nanomaterials*, 12(9), 2022.

[281] Halyne S. Borges, Celso A. N. Júnior, David S. Brandão, Fujun Liu, V. V. R. Pereira, S. J. Xie, Fanyao Qu, and A. M. Alcalde. Persistent entanglement of valley exciton qubits in transition metal dichalcogenides integrated into a bimodal optical cavity. *Phys. Rev. B*, 107:035404, 2023.

[282] Fengcheng Wu, Fanyao Qu, and A. H. MacDonald. Exciton band structure of monolayer mos_2. *Phys. Rev. B*, 91:075310, 2015.

[283] Duy Le, Alexei Barinov, Edwin Preciado, Miguel Isarraraz, Iori Tanabe, Takashi Komesu, Conrad Troha, Ludwig Bartels, Talat S Rahman, and Peter A Dowben. Spin–orbit coupling in the band structure of monolayer wse2. *Journal of Physics: Condensed Matter*, 27(18):182201, 2015.

[284] Nasser Alidoust, Guang Bian, Su-Yang Xu, Raman Sankar, Madhab Neupane, Chang Liu, Ilya Belopolski, Dong-Xia Qu, Jonathan D. Denlinger, Fang-Cheng Chou, and M. Zahid Hasan. Observation of monolayer valence band spin-orbit effect and induced quantum well states in mox$_2$. *Nature Communications*, 5(1):4673, 2014.

[285] Jiaqi Cai, Eric Anderson, Chong Wang, Xiaowei Zhang, Xiaoyu Liu, William Holtzmann, Yinong Zhang, Fengren Fan, Takashi Taniguchi, Kenji Watanabe, Ying Ran, Ting Cao, Liang Fu, Di Xiao, Wang Yao, and Xiaodong Xu. Signatures of fractional quantum anomalous hall states in twisted mote$_2$. *Nature*, 622(7981):63–68, 2023.

[286] Folkert K. de Vries, Elías Portolés, Giulia Zheng, Takashi Taniguchi, Kenji Watanabe, Thomas Ihn, Klaus Ensslin, and Peter Rickhaus. Gate-defined josephson junctions in magic-angle twisted bilayer graphene. *Nature Nanotechnology*, 16(7):760–763, 2021.

[287] Dahlia R. Klein, Li-Qiao Xia, David MacNeill, Kenji Watanabe, Takashi Taniguchi, and Pablo Jarillo-Herrero. Electrical switching of a bistable moiré superconductor. *Nature Nanotechnology*, 18(4):331–335, 2023.

[288] Daniel Rodan-Legrain, Yuan Cao, Jeong Min Park, Sergio C. de la Barrera, Mallika T. Randeria, Kenji Watanabe, Takashi Taniguchi, and Pablo Jarillo-Herrero. Highly tunable junctions and non-local josephson effect in magic-angle graphene tunnelling devices. *Nature Nanotechnology*, 16(7):769–775, 2021.

[289] Haoning Tang, Yiting Wang, Xueqi Ni, Kenji Watanabe, Takashi Taniguchi, Pablo Jarillo-Herrero, Shanhui Fan, Eric Mazur, Amir Yacoby, and Yuan Cao. On-chip multi-degree-of-freedom control of two-dimensional materials. *Nature*, 632(8027):1038–1044, 2024.

[290] A. Inbar, J. Birkbeck, J. Xiao, T. Taniguchi, K. Watanabe, B. Yan, Y. Oreg, Ady Stern, E. Berg, and S. Ilani. The quantum twisting microscope. *Nature*, 614(7949):682–687, 2023.

[291] Edward McCann and Mikito Koshino. The electronic properties of bilayer graphene. *Reports on Progress in Physics*, 76(5):056503, 2013.

[292] S. Shallcross, S. Sharma, E. Kandelaki, and O. A. Pankratov. Electronic structure of turbostratic graphene. *Phys. Rev. B*, 81:165105, Apr 2010.

[293] J. M. B. Lopes dos Santos, N. M. R. Peres, and A. H. Castro Neto. Continuum model of the twisted graphene bilayer. *Phys. Rev. B*, 86:155449, 2012.

[294] Kazuyuki Uchida, Shinnosuke Furuya, Jun-Ichi Iwata, and Atsushi Oshiyama. Atomic corrugation and electron localization due to moiré patterns in twisted bilayer graphenes. *Phys. Rev. B*, 90:155451, 2014.

[295] Alejandro Lopez-Bezanilla and J. L. Lado. Electrical band flattening, valley flux, and superconductivity in twisted trilayer graphene. *Phys. Rev. Res.*, 2:033357, 2020.

[296] Takahiro Fukui, Yasuhiro Hatsugai, and Hiroshi Suzuki. Chern numbers in discretized Brillouin zone: Efficient method of computing (spin) Hall conductances. *Journal of the Physical Society of Japan*, 74(6):1674–1677, 2005.

[297] Philip L. Taylor and Olle Heinonen. *A Quantum Approach to Condensed Matter Physics*. Cambridge University Press, Cambridge, 2002.

[298] P. Hohenberg and W. Kohn. Inhomogeneous electron gas. *Phys. Rev.*, 136:B864–B871, 1964.

[299] W. Kohn and L. J. Sham. Self-consistent equations including exchange and correlation effects. *Phys. Rev.*, 140:A1133–A1138, 1965.

[300] Holger Fehske, Ralf Schneider, and Alexander Weiße. *Computational Many-Particle Physics*, volume 739 of *Lecture Notes in Physics*. Springer, 2008.

[301] Daniel Miravet, Ludmiła Szulakowska, Maciej Bieniek, Katarzyna Sadecka, Marek Korkusiński, and Paweł Hawrylak. Theory of excitonic complexes in gated wse$_2$ quantum dots. *Phys. Rev. B*, 110:235404, 2024.

[302] Ulrich Schollwöck. The density-matrix renormalization group in the age of matrix product states. *Annals of Physics*, 326(1):96–192, 2011. January 2011 Special Issue.

[303] Román Orús. A practical introduction to tensor networks: Matrix product states and projected entangled pair states. *Annals of Physics*, 349:117–158, 2014.

[304] Stephen Carr, Shiang Fang, Pablo Jarillo-Herrero, and Efthimios Kaxiras. Pressure dependence of the magic twist angle in graphene superlattices. *Phys. Rev. B*, 98:085144, 2018.

[305] Stephen Carr, Shiang Fang, and Efthimios Kaxiras. Electronic-structure methods for twisted moiré layers. *Nature Reviews Materials*, 5(10):748–763, 2020.

[306] Shiang Fang, Stephen Carr, Ziyan Zhu, Daniel Massatt, and Efthimios Kaxiras. Angle-dependent ab initio low-energy hamiltonians for a relaxed twisted bilayer graphene heterostructure. *arXiv:*, 2019.

[307] Ahmed Khalifa, Ganpathy Murthy, and Ribhu K. Kaul. Absence of edge states in the valley chern insulator in moiré graphene. *Phys. Rev. B*, 107:085138, 2023.

[308] Eric Polizzi. Density-matrix-based algorithm for solving eigenvalue problems. *Phys. Rev. B*, 79:115112, 2009.

[309] https://www.alliancecan.ca/.

[310] G. H. Wannier. A result not dependent on rationality for bloch electrons in a magnetic field. *Physica Status Solidi (b)*, 88(2):757–765, 1978.

[311] Päivi Törmä, Sebastiano Peotta, and Bogdan A. Bernevig. Superconductivity, superfluidity and quantum geometry in twisted multilayer systems. *Nature Reviews Physics*, 4(8):528–542, 2022.

[312] Kevin P. Nuckolls, Ryan L. Lee, Myungchul Oh, Dillon Wong, Tomohiro Soejima, Jung Pyo Hong, Dumitru Călugăru, Jonah Herzog Arbeitman, B. Andrei Bernevig, Kenji Watanabe, Takashi Taniguchi, Nicolas Regnault, Michael P. Zaletel, and Ali Yazdani. Quantum textures of the many-body wavefunctions in magic-angle graphene. *Nature*, 620(7974):525–532, 2023.

[313] Matthieu Fortin-Deschenes, Rui Pu, Yan-Feng Zhou, Chao Ma, Patrick Cheung, Kenji Watanabe, Takashi Taniguchi, Fan Zhang, Xu Du, and Fengnian Xia. Uncovering topological edge states in twisted bilayer graphene. *Nano Letters*, 22(15):6186–6193, 2022.

[314] J. Sichau, M. Prada, T. Anlauf, T. J. Lyon, B. Bosnjak, L. Tiemann, and R. H. Blick. Resonance microwave measurements of an intrinsic spin-orbit coupling gap in graphene: A possible indication of a topological state. *Phys. Rev. Lett.*, 122:046403, 2019.

[315] U. R. Singh, M. Prada, V. Strenzke, B. Bosnjak, T. Schmirander, L. Tiemann, and R. H. Blick. Sublattice symmetry breaking and ultralow energy excitations in graphene-on-hBN heterostructures. *Phys. Rev. B*, 102:245134, 2020.

[316] Lars Tiemann, Marta Prada, Vincent Strenzke, and Robert H. Blick. Comment on ”electron spin resonance and collective excitations in magic-angle twisted bilayer graphene”. *arXiv:*, 2022.

[317] M. Fleischmann, R. Gupta, D. Weckbecker, W. Landgraf, O. Pankratov, V. Meded, and S. Shallcross. Moiré edge states in twisted graphene nanoribbons. *Phys. Rev. B*, 97:205128, 2018.

[318] Jianpeng Liu, Junwei Liu, and Xi Dai. Pseudo landau level representation of twisted bilayer graphene: Band topology and implications on the correlated insulating phase. *Phys. Rev. B*, 99:155415, 2019.

[319] G. Trambly de Laissardière, D. Mayou, and L. Magaud. Numerical studies of confined states in rotated bilayers of graphene. *Phys. Rev. B*, 86:125413, 2012.

[320] A. O. Sboychakov, A. L. Rakhmanov, A. V. Rozhkov, and Franco Nori. Electronic spectrum of twisted bilayer graphene. *Phys. Rev. B*, 92:075402, 2015.

[321] Shiang Fang and Efthimios Kaxiras. Electronic structure theory of weakly interacting bilayers. *Phys. Rev. B*, 93:235153, 2016.

[322] Louk Rademaker, Dmitry A. Abanin, and Paula Mellado. Charge smoothening and band flattening due to hartree corrections in twisted bilayer graphene. *Phys. Rev. B*, 100:205114, 2019.

[323] Tomas Löthman, Johann Schmidt, Fariborz Parhizgar, and Annica M. Black-Schaffer. Nematic superconductivity in magic-angle twisted bilayer graphene from atomistic modeling. *Communications Physics*, 5(1):92, 2022.

[324] Jian Kang and Oskar Vafek. Pseudomagnetic fields, particle-hole asymmetry, and microscopic effective continuum hamiltonians of twisted bilayer graphene. *Phys. Rev. B*, 107:075408, 2023.

[325] Oskar Vafek and Jian Kang. Continuum effective hamiltonian for graphene bilayers for an arbitrary smooth lattice deformation from microscopic theories. *Phys. Rev. B*, 107:075123, 2023.

[326] Wangqian Miao, Chu Li, Xu Han, Ding Pan, and Xi Dai. Truncated atomic plane wave method for subband structure calculations of moiré systems. *Phys. Rev. B*, 107:125112, 2023.

[327] B. Hunt, J. D. Sanchez-Yamagishi, A. F. Young, M. Yankowitz, B. J. LeRoy, K. Watanabe, T. Taniguchi, P. Moon, M. Koshino, P. Jarillo-Herrero, and R. C. Ashoori. Massive Dirac Fermions and Hofstadter Butterfly in a van der Waals Heterostructure. *Science*, 340(6139):1427–1430, 2013.

[328] Kevin J. U. Vidarte and Caio Lewenkopf. Magnetic properties of low-angle twisted bilayer graphene at three-quarters filling. *arXiv*, 2024.

[329] Gautam Rai, Lorenzo Crippa, Dumitru Călugăru, Haoyu Hu, Francesca Paoletti, Luca de' Medici, Antoine Georges, B. Andrei Bernevig, Roser Valentí, Giorgio Sangiovanni, and Tim Wehling. Dynamical correlations and order in magic-angle twisted bilayer graphene. *Phys. Rev. X*, 14:031045, Sep 2024.

[330] Nicolas Tancogne-Dejean, Micael J. T. Oliveira, Xavier Andrade, Heiko Appel, Carlos H. Borca, Guillaume Le Breton, Florian Buchholz, Alberto Castro, Stefano Corni, Alfredo A. Correa, Umberto De Giovannini, Alain Delgado, Florian G. Eich, Johannes Flick, Gabriel Gil, Adrián Gomez, Nicole Helbig, Hannes Hübener, René Jestädt, Joaquim Jornet-Somoza, Ask H. Larsen, Irina V. Lebedeva, Martin Lüders, Miguel A. L. Marques, Sebastian T. Ohlmann, Silvio Pipolo, Markus Rampp, Carlo A. Rozzi, David A. Strubbe, Shunsuke A. Sato, Christian Schäfer, Iris Theophilou, Alicia Welden, and Angel Rubio. Octopus, a computational framework for exploring light-driven phenomena and quantum dynamics in extended and finite systems. *The Journal of Chemical Physics*, 152(12):124119, 2020.

Appendix A

Fourier transform identities for continuous model derivation

We aim to prove the following identity:

$$\frac{1}{N}\sum_{\vec{R}^{(1)}} e^{-i\vec{R}^{(1)}\cdot(\vec{k}-\vec{G}'^{(1)}-\vec{k}')} = \sum_{\vec{G}^{(1)}} \delta_{\vec{k}+\vec{G}^{(1)},\vec{k}'+\vec{G}'^{(1)}}. \tag{A.1}$$

To do so, we analyze a general expression involving a sum over real-space lattice vectors. Let's define a function $f(\vec{k})$ as follows:

$$f(\vec{k}) = \frac{1}{N}\sum_{\vec{R}} e^{-i\vec{R}\cdot\vec{k}} = \delta_{\vec{k},\vec{G}}. \tag{A.2}$$

This expression tells us that $f(\vec{k})$ evaluates to 1 if $\vec{k}$ is a reciprocal lattice vector, and 0 otherwise:

$$f(\vec{k}) = \begin{cases} 1, & \vec{k} = \vec{G} \\ 0, & \text{otherwise} \end{cases} \tag{A.3}$$

Let us first verify the case $\vec{k} = \vec{G}$. Recall the definitions for real and reciprocal lattice vectors:

$$\vec{R} = n_1\vec{a}_1 + n_2\vec{a}_2 \tag{A.4}$$

$$\vec{G} = m_1\vec{G}_1 + m_2\vec{G}_2 \tag{A.5}$$

$$G_a a_b = 2\pi\delta_{a,b} \tag{A.6}$$

Using these definitions in Eq. A.2, we get:

$$\frac{1}{N}\sum_{\vec{R}} e^{-i\vec{R}\cdot\vec{G}} = \frac{1}{N}\sum_{\vec{R}} e^{-i(n_1\vec{a}_1+n_2\vec{a}_2)\cdot(m_1\vec{G}_1+m_2\vec{G}_2)} = \frac{1}{N}\sum_{\vec{R}} e^{-i2\pi(n_1m_1+n_2m_2)} = 1. \tag{A.7}$$

Since the exponential evaluates to 1 for all terms in the sum, the result is simply 1. Therefore, Eq. A.3 is satisfied when $\vec{k} = \vec{G}$. Now we examine the case where $\vec{k} \notin$ the reciprocal lattice. In this case, $\exp\left(-i\vec{R}\cdot\vec{k}\right)$ no longer evaluates to unity. Writing out the sum explicitly:

$$\sum_{\vec{R}} e^{-i\vec{R}\cdot\vec{k}} \rightarrow \sum_{n_1,n_2} e^{-i\vec{k}\cdot(n_1\vec{a}_1+n_2\vec{a}_2)} = \sum_{n_1} e^{-i(\vec{k}\cdot\vec{a}_1)n_1} \sum_{n_2} e^{-i(\vec{k}\cdot\vec{a}_2)n_2} \tag{A.8}$$

We'll now analyze each geometric series separately, beginning with:

$$\sum_{n_1} e^{-i(\vec{k}\cdot\vec{a}_1)n_1} = \sum_{n_1}\left(e^{-i(\vec{k}\cdot\vec{a}_1)}\right)^{n_1} = 1 + e^{-i(\vec{k}\cdot\vec{a}_1)} + \left(e^{-i(\vec{k}\cdot\vec{a}_1)}\right)^2 + \dots. \tag{A.9}$$

This is indeed a geometric series, for which the sum is known:

$$1 + q + q^2 + \cdots + q^n = \frac{1-|q|^{n+1}}{1-|q|}, \quad q \neq 1 \tag{A.10}$$

Applying this to our expression:

$$\sum_{n_1} e^{-i(\vec{k}\cdot\vec{a}_1)n_1} = \frac{1-\left(e^{-i(\vec{k}\cdot\vec{a}_1)}\right)^N}{1-\left|e^{-i(\vec{k}\cdot\vec{a}_1)}\right|} \tag{A.11}$$

Returning to the full expression:

$$\frac{1}{N}\sum_{n_1} e^{-i(\vec{k}\cdot\vec{a}_1)n_1} = \frac{1}{N}\cdot\frac{1-\left(e^{-i(\vec{k}\cdot\vec{a}_1)}\right)^N}{1-\left|e^{-i(\vec{k}\cdot\vec{a}_1)}\right|} \xrightarrow[N\to\infty]{} 0 \tag{A.12}$$

We have therefore shown that:

$$\frac{1}{N}\sum_{\vec{R}} e^{-i\vec{R}\cdot\vec{k}} = \delta_{\vec{k},\vec{G}}. \tag{A.13}$$

Appendix B

Interlayer tunneling terms

We present here a detailed derivation of the tunneling matrices $T_1^{\alpha\beta}, T_2^{\alpha\beta}, T_3^{\alpha\beta}$. To begin with, we will remind a few relations that will be useful throughout our calculation: The vectors pointing to the position of an atom within a unit cell have the form:

$$\vec{\tau}_A^{(1)} = (0,0) \tag{B.1}$$

$$\vec{\tau}_B^{(1)} = \frac{a_0}{\sqrt{3}} R_{\theta/2}^{(1)}(0,1) \tag{B.2}$$

$$\vec{\tau}_A^{(2)} = -\frac{a_0}{\sqrt{3}} R_{\theta/2}^{(2)}(0,1) \tag{B.3}$$

$$\vec{\tau}_B^{(2)} = (0,0) \tag{B.4}$$

The reciprocal lattice vectors can be defined as:

$$\vec{G}_{n,m}^{(j)} = n\vec{G}_1^{(j)} + m\vec{G}_2^{(j)} \tag{B.5}$$

And specifically:

$$\vec{G}_1^{(j)} = \frac{4\pi}{a_0\sqrt{3}} R_{\theta/2}^{(j)} \left(-\frac{\sqrt{3}}{2}, \frac{1}{2} \right) \tag{B.6}$$

$$\vec{G}_2^{(j)} = \frac{4\pi}{a_0\sqrt{3}} R_{\theta/2}^{(j)} \left(\frac{\sqrt{3}}{2}, \frac{1}{2} \right) \tag{B.7}$$

The rotation matrices for both layers have the form:

$$R_{\theta/2}^{(1)} = \begin{bmatrix} \cos(\theta/2) & -\sin(\theta/2) \\ \sin(\theta/2) & \cos(\theta/2) \end{bmatrix} \tag{B.8}$$

$$R_{\theta/2}^{(2)} = \begin{bmatrix} \cos(\theta/2) & \sin(\theta/2) \\ -\sin(\theta/2) & \cos(\theta/2) \end{bmatrix} \tag{B.9}$$

Finally, the general form of the tunneling matrix element is:

$$(T_i)^{\alpha\beta} = we^{-i\left[\vec{G}^{(2)}_{n_2,m_2}\cdot\vec{\tau}^{(2)}_{\beta} - \vec{G}^{(1)}_{n_1,m_1}\cdot\vec{\tau}^{(1)}_{\alpha}\right]} \tag{B.10}$$

We start now, considering the case when $i = 1 \to (n_1, m_1) = (0, 0)$. That gives us:

$$(T_1)^{\alpha\beta} = we^{-i\left[0\cdot\vec{\tau}^{(2)}_{\beta} - 0\cdot\vec{\tau}^{(1)}_{\alpha}\right]} = (w)_{\alpha\beta}\,. \tag{B.11}$$

And finally, we have:

$$(T_1)^{\alpha\beta} = w \begin{bmatrix} 1 & 1 \\ 1 & 1 \end{bmatrix} \tag{B.12}$$

The second and third cases are much more complex than this one. Since not all terms will simplify, we have to consider different α and β. In the second one we have $i = 2 \to (n_1, m_1) = (0, 1)$, which gives us, for the AA term:

$$(T_2)^{A,A} = we^{-i\left[\vec{G}^{(2)}_{0,1}\cdot\vec{\tau}^{(2)}_{A} - \vec{G}^{(1)}_{0,1}\cdot\vec{\tau}^{(1)}_{A}\right]} = we^{-i\left[\vec{G}^{(2)}_{0,1}\cdot\vec{\tau}^{(2)}_{A}\right]} \tag{B.13}$$

We will split this calculation into smaller parts and first obtain the product:

$$\vec{G}^{(2)}_{0,1} \cdot \vec{\tau}^{(2)}_{A} = \frac{4\pi}{a_0\sqrt{3}} R^{(2)}_{\theta/2} \left(\frac{\sqrt{3}}{2}, -\frac{1}{2}\right) \cdot \left(-\frac{a_0}{\sqrt{3}}\right) R^{(2)}_{\theta/2}(0,1) \tag{B.14}$$

We will also calculate the product of the vectors with the rotation matrices separately:

$$R^{(2)}_{\theta/2} \begin{pmatrix} -\frac{\sqrt{3}}{2} \\ -\frac{1}{2} \end{pmatrix} = \begin{bmatrix} \cos(\theta/2) & \sin(\theta/2) \\ -\sin(\theta/2) & \cos(\theta/2) \end{bmatrix} \begin{pmatrix} -\frac{\sqrt{3}}{2} \\ -\frac{1}{2} \end{pmatrix} = \begin{pmatrix} -\frac{\sqrt{3}}{2}\cos(\theta/2) - \frac{1}{2}\sin(\theta/2) \\ \frac{\sqrt{3}}{2}\sin(\theta/2) - \frac{1}{2}\cos(\theta/2) \end{pmatrix} \tag{B.15}$$

$$R^{(2)}_{\theta/2} \begin{pmatrix} 0 \\ 1 \end{pmatrix} = \begin{bmatrix} \cos(\theta/2) & \sin(\theta/2) \\ -\sin(\theta/2) & \cos(\theta/2) \end{bmatrix} \begin{pmatrix} 0 \\ 1 \end{pmatrix} = \begin{pmatrix} \sin(\theta/2) \\ \cos(\theta/2) \end{pmatrix} \tag{B.16}$$

When we insert the results back into Eq. B.14, we get:

$$\vec{G}^{(2)}_{0,1} \cdot \vec{\tau}^{(2)}_{A} = -\frac{4\pi}{3} \begin{pmatrix} -\frac{\sqrt{3}}{2}\cos(\theta/2) - \frac{1}{2}\sin(\theta/2) \\ \frac{\sqrt{3}}{2}\sin(\theta/2) - \frac{1}{2}\cos(\theta/2) \end{pmatrix} \cdot \begin{pmatrix} \sin(\theta/2) \\ \cos(\theta/2) \end{pmatrix} \tag{B.17}$$

$$= -\frac{4\pi}{3} \left[\left(-\frac{\sqrt{3}}{2}\cos(\theta/2) - \frac{1}{2}\sin(\theta/2) \right) \sin(\theta/2) + \left(\frac{\sqrt{3}}{2}\sin(\theta/2) - \frac{1}{2}\cos(\theta/2) \right) \cos(\theta/2) \right] \tag{B.18}$$

$$= -\frac{4\pi}{3} \left[-\frac{1}{2}\sin^2(\theta/2) - \frac{1}{2}\cos^2(\theta/2) \right] = -\frac{4\pi}{3}\left(-\frac{1}{2}\right) = \frac{4\pi}{6} = \frac{2\pi}{3} \tag{B.19}$$

That leads us to the final expression:

$$(T_2)^{A,A} = we^{-i\left[\vec{G}^{(2)}_{0,1}\cdot\vec{\tau}^{(2)}_{A} - \vec{G}^{(1)}_{0,1}\cdot\vec{\tau}^{(1)}_{A}\right]} = we^{-i\left[\vec{G}^{(2)}_{0,1}\cdot\vec{\tau}^{(2)}_{A}\right]} = we^{-i\left[\frac{2\pi}{3}\right]} \tag{B.20}$$

Now we consider the BB term:

$$(T_2)^{B,B} = we^{-i\left[\vec{G}^{(2)}_{0,1}\cdot\vec{\tau}^{(2)}_B - \vec{G}^{(1)}_{0,1}\cdot\vec{\tau}^{(1)}_B\right]} = we^{-i\left[-\vec{G}^{(1)}_{0,1}\cdot\vec{\tau}^{(1)}_B\right]} = we^{i\left[\vec{G}^{(1)}_{0,1}\cdot\vec{\tau}^{(1)}_B\right]} \tag{B.21}$$

Again, we split the calculation into smaller pieces:

$$\vec{G}^{(1)}_{0,1}\cdot\vec{\tau}^{(1)}_B = \frac{4\pi}{a_0\sqrt{3}} R^{(1)}_{\theta/2}\left(-\frac{\sqrt{3}}{2}, -\frac{1}{2}\right)\cdot\left(\frac{a_0}{\sqrt{3}}\right) R^{(1)}_{\theta/2}(0,1) \tag{B.22}$$

And calculate the product of the rotation matrices and vectors:

$$R^{(1)}_{\theta/2}\begin{pmatrix} -\frac{\sqrt{3}}{2} \\ -\frac{1}{2} \end{pmatrix} = \begin{bmatrix} \cos(\theta/2) & -\sin(\theta/2) \\ \sin(\theta/2) & \cos(\theta/2) \end{bmatrix}\begin{pmatrix} -\frac{\sqrt{3}}{2} \\ -\frac{1}{2} \end{pmatrix} = \begin{pmatrix} -\frac{\sqrt{3}}{2}\cos(\theta/2) + \frac{1}{2}\sin(\theta/2) \\ -\frac{\sqrt{3}}{2}\sin(\theta/2) - \frac{1}{2}\cos(\theta/2) \end{pmatrix} \tag{B.23}$$

$$R^{(1)}_{\theta/2}\begin{pmatrix} 0 \\ 1 \end{pmatrix} = \begin{bmatrix} \cos(\theta/2) & -\sin(\theta/2) \\ \sin(\theta/2) & \cos(\theta/2) \end{bmatrix}\begin{pmatrix} 0 \\ 1 \end{pmatrix} = \begin{pmatrix} -\sin(\theta/2) \\ \cos(\theta/2) \end{pmatrix} \tag{B.24}$$

Which gives us:

$$\vec{G}^{(1)}_{0,1}\cdot\vec{\tau}^{(1)}_B = \frac{4\pi}{3}\begin{pmatrix} -\frac{\sqrt{3}}{2}\cos(\theta/2) + \frac{1}{2}\sin(\theta/2) \\ -\frac{\sqrt{3}}{2}\sin(\theta/2) - \frac{1}{2}\cos(\theta/2) \end{pmatrix}\cdot\begin{pmatrix} -\sin(\theta/2) \\ \cos(\theta/2) \end{pmatrix} \tag{B.25}$$

$$= \frac{4\pi}{3}\left[-\frac{\sqrt{3}}{2}\cos(\theta/2)(-\sin(\theta/2)) + \frac{1}{2}\sin^2(\theta/2) - \frac{\sqrt{3}}{2}\sin(\theta/2)\cos(\theta/2) - \frac{1}{2}\cos^2(\theta/2)\right] \tag{B.26}$$

$$= \frac{4\pi}{3}\left[\frac{\sqrt{3}}{2}\sin(\theta/2)\cos(\theta/2) + \frac{1}{2}\sin^2(\theta/2) - \frac{\sqrt{3}}{2}\sin(\theta/2)\cos(\theta/2) - \frac{1}{2}\cos^2(\theta/2)\right] \tag{B.27}$$

$$= \frac{4\pi}{3}\left[\frac{1}{2}\sin^2(\theta/2) - \frac{1}{2}\cos^2(\theta/2)\right] = \frac{4\pi}{3} \cdot \left(-\frac{1}{2}\right) = -\frac{2\pi}{3} \tag{B.28}$$

And finally we have:

$$(T_2)^{B,B} = we^{i\vec{G}^{(1)}_{0,1}\cdot\vec{\tau}^{(1)}_B} = we^{-i\left[\frac{2\pi}{3}\right]} \tag{B.29}$$

Now, the AB term, which is much simpler:

$$(T_2)^{A,B} = we^{-i\left[\vec{G}^{(2)}_{0,1}\cdot\vec{\tau}^{(2)}_A - \vec{G}^{(1)}_{0,1}\cdot\vec{\tau}^{(1)}_B\right]} \tag{B.30}$$

$$\vec{G}^{(2)}_{0,1} \cdot \vec{\tau}^{(2)}_A = \frac{2\pi}{3} \tag{B.31}$$

$$\vec{G}^{(1)}_{0,1} \cdot \vec{\tau}^{(1)}_B = -\frac{2\pi}{3} \tag{B.32}$$

We get:

$$(T_2)^{A,B} = we^{-i\left[\frac{2\pi}{3}+\frac{2\pi}{3}\right]} = we^{-i\left[\frac{4\pi}{3}\right]} = we^{i\left[\frac{2\pi}{3}\right]} \tag{B.33}$$

And for the BA analogously:

$$(T_2)^{B,A} = we^{-i\left[\vec{G}^{(2)}_{0,1}\cdot\vec{\tau}^{(2)}_B - \vec{G}^{(1)}_{0,1}\cdot\vec{\tau}^{(1)}_A\right]} = we^{-i[0]} = w \tag{B.34}$$

Collecting all the terms, we get the final form of the T_2 matrix:

$$T_2 = w\begin{bmatrix} e^{-i\left[\frac{2\pi}{3}\right]} & e^{i\left[\frac{2\pi}{3}\right]} \\ 1 & e^{-i\left[\frac{2\pi}{3}\right]} \end{bmatrix} \tag{B.35}$$

We now move on to the third matrix, where $i = 3 \to (n_3, m_3) = (1, 0)$. We will follow an analogous path, and start with the AA term:

$$(T_3)^{A,A} = we^{-i\left[\vec{G}^{(2)}_{1,0}\cdot\vec{\tau}^{(2)}_A - \vec{G}^{(1)}_{1,0}\cdot\vec{\tau}^{(1)}_A\right]} = we^{-i\left[\vec{G}^{(2)}_{0,1}\cdot\vec{\tau}^{(2)}_A\right]} \tag{B.36}$$

We calculate the product first:

$$\vec{G}^{(2)}_{1,0} \cdot \vec{\tau}^{(2)}_A = \frac{4\pi}{a_0\sqrt{3}} R^{(2)}_{\theta/2} \left(-\frac{\sqrt{3}}{2},\ \ \frac{1}{2}\right) \cdot \left(-\frac{a_0}{\sqrt{3}}\right) R^{(2)}_{\theta/2}(0,1) \tag{B.37}$$

And now the product of the matrices and vectors:

$$R^{(2)}_{\theta/2} \begin{pmatrix} -\frac{\sqrt{3}}{2} \\ \frac{1}{2} \end{pmatrix} = \begin{bmatrix} \cos(\theta/2) & \sin(\theta/2) \\ -\sin(\theta/2) & \cos(\theta/2) \end{bmatrix} \begin{pmatrix} -\frac{\sqrt{3}}{2} \\ \frac{1}{2} \end{pmatrix} = \begin{pmatrix} -\frac{\sqrt{3}}{2}\cos(\theta/2) + \frac{1}{2}\sin(\theta/2) \\ \frac{\sqrt{3}}{2}\sin(\theta/2) + \frac{1}{2}\cos(\theta/2) \end{pmatrix} \tag{B.38}$$

$$R^{(2)}_{\theta/2} \begin{pmatrix} 0 \\ 1 \end{pmatrix} = \begin{bmatrix} \cos(\theta/2) & \sin(\theta/2) \\ -\sin(\theta/2) & \cos(\theta/2) \end{bmatrix} \begin{pmatrix} 0 \\ 1 \end{pmatrix} = \begin{pmatrix} \sin(\theta/2) \\ \cos(\theta/2) \end{pmatrix} \tag{B.39}$$

We now insert it back in:

$$\vec{G}^{(2)}_{0,1} \cdot \vec{\tau}^{(2)}_A = \frac{4\pi}{3} \begin{pmatrix} -\frac{\sqrt{3}}{2}\cos(\theta/2) + \frac{1}{2}\sin(\theta/2) \\ \frac{\sqrt{3}}{2}\sin(\theta/2) + \frac{1}{2}\cos(\theta/2) \end{pmatrix} \cdot \begin{pmatrix} \sin(\theta/2) \\ \cos(\theta/2) \end{pmatrix} \tag{B.40}$$

$$= -\frac{4\pi}{3}\left(-\frac{\sqrt{3}}{2}\sin(\theta/2)\cos(\theta/2) + \frac{1}{2}\sin^2(\theta/2) + \frac{\sqrt{3}}{2}\sin(\theta/2)\cos(\theta/2) + \frac{1}{2}\cos^2(\theta/2)\right) \tag{B.41}$$

$$= -\frac{4\pi}{3}\left(\frac{1}{2}\sin^2(\theta/2) + \frac{1}{2}\cos^2(\theta/2)\right) = -\frac{4\pi}{3}\cdot\frac{1}{2} = -\frac{2\pi}{3} \tag{B.42}$$

That gives us:

$$(T_3)^{A,A} = we^{-i\left[\vec{G}^{(2)}_{0,1}\cdot\vec{\tau}^{(2)}_A\right]} = we^{i\left[\frac{2\pi}{3}\right]} \tag{B.43}$$

Now we move on to the BB case:

$$(T_3)^{B,B} = we^{-i\left[\vec{G}^{(2)}_{1,0}\cdot\vec{\tau}^{(2)}_B - \vec{G}^{(1)}_{1,0}\cdot\vec{\tau}^{(1)}_B\right]} = we^{-i\left[-\vec{G}^{(1)}_{1,0}\cdot\vec{\tau}^{(1)}_B\right]} = we^{i\left[\vec{G}^{(1)}_{1,0}\cdot\vec{\tau}^{(1)}_B\right]} \tag{B.44}$$

As before, we calculate the product:

$$\vec{G}^{(1)}_{1,0}\cdot\vec{\tau}^{(1)}_B = \frac{4\pi}{a_0\sqrt{3}} R^{(1)}_{\theta/2}\left(-\frac{\sqrt{3}}{2},\frac{1}{2}\right)\left(\frac{a_0}{\sqrt{3}}\right) R^{(1)}_{\theta/2}(0,1) \tag{B.45}$$

And now the matrices and vectors product:

$$R^{(2)}_{\theta/2}\begin{pmatrix} -\frac{\sqrt{3}}{2} \\ \frac{1}{2} \end{pmatrix} = \begin{bmatrix} \cos(\theta/2) & -\sin(\theta/2) \\ \sin(\theta/2) & \cos(\theta/2) \end{bmatrix}\begin{pmatrix} -\frac{\sqrt{3}}{2} \\ \frac{1}{2} \end{pmatrix} = \begin{pmatrix} -\frac{\sqrt{3}}{2}\cos(\theta/2) - \frac{1}{2}\sin(\theta/2) \\ -\frac{\sqrt{3}}{2}\sin(\theta/2) + \frac{1}{2}\cos(\theta/2) \end{pmatrix} \tag{B.46}$$

$$R^{(2)}_{\theta/2}\begin{pmatrix} 0 \\ 1 \end{pmatrix} = \begin{bmatrix} \cos(\theta/2) & -\sin(\theta/2) \\ \sin(\theta/2) & \cos(\theta/2) \end{bmatrix}\begin{pmatrix} 0 \\ 1 \end{pmatrix} = \begin{pmatrix} -\sin(\theta/2) \\ \cos(\theta/2) \end{pmatrix} \tag{B.47}$$

Which inserted back in, gives us:

$$\vec{G}^{(2)}_{0,1}\cdot\vec{\tau}^{(2)}_A = \frac{4\pi}{3}\left(\begin{pmatrix} -\frac{\sqrt{3}}{2}\cos(\theta/2) - \frac{1}{2}\sin(\theta/2) \\ -\frac{\sqrt{3}}{2}\sin(\theta/2) + \frac{1}{2}\cos(\theta/2) \end{pmatrix}\cdot\begin{pmatrix} -\sin(\theta/2) \\ \cos(\theta/2) \end{pmatrix}\right) \tag{B.48}$$

$$= \frac{4\pi}{3}\left(\frac{\sqrt{3}}{2}\sin(\theta/2)\cos(\theta/2) + \frac{1}{2}\sin^2(\theta/2) - \frac{\sqrt{3}}{2}\sin(\theta/2)\cos(\theta/2) + \frac{1}{2}\cos^2(\theta/2)\right) \tag{B.49}$$

$$= \frac{4\pi}{3}\left(\frac{1}{2}\sin^2(\theta/2) + \frac{1}{2}\cos^2(\theta/2)\right) = \frac{4\pi}{3}\cdot\frac{1}{2} = \frac{2\pi}{3} \tag{B.50}$$

That leads us to:

$$(T_3)^{B,B} = we^{i\left[\vec{G}^{(1)}_{1,0}\cdot\vec{\tau}^{(1)}_B\right]} = we^{i\left[\dfrac{2\pi}{3}\right]} \tag{B.51}$$

And finally the AB and BA terms:

$$(T_3)^{A,B} = we^{-i\left[\vec{G}^{(2)}_{1,0}\cdot\vec{\tau}^{(2)}_A - \vec{G}^{(1)}_{1,0}\cdot\vec{\tau}^{(1)}_B\right]} \tag{B.52}$$

$$\vec{G}^{(2)}_{1,0}\cdot\vec{\tau}^{(2)}_A = -\frac{2\pi}{3} \tag{B.53}$$

$$\vec{G}^{(1)}_{1,0}\cdot\vec{\tau}^{(1)}_B = \frac{2\pi}{3} \tag{B.54}$$

$$(T_3)^{A,B} = we^{-i\left[\vec{G}^{(2)}_{1,0}\cdot\vec{\tau}^{(2)}_A - \vec{G}^{(1)}_{1,0}\cdot\vec{\tau}^{(1)}_B\right]} = we^{-i\left[\frac{2\pi}{3}+\frac{2\pi}{3}\right]} = we^{i\left[\frac{4\pi}{3}\right]} = we^{-i\left[\frac{2\pi}{3}\right]} \tag{B.55}$$

$$(T_3)^{B,A} = we^{-i\left[\vec{G}^{(2)}_{1,0}\cdot\vec{\tau}^{(2)}_B - \vec{G}^{(1)}_{1,0}\cdot\vec{\tau}^{(1)}_A\right]} = we^{-i[0]} = w \tag{B.56}$$

That gives us the final form of the T_3 matrix:

$$T_3 = w\begin{bmatrix} e^{i\left[\frac{2\pi}{3}\right]} & e^{-i\left[\frac{2\pi}{3}\right]} \\ 1 & e^{i\left[\frac{2\pi}{3}\right]} \end{bmatrix} \tag{B.57}$$

Appendix C

Relaxation details of twisted trilayer graphene

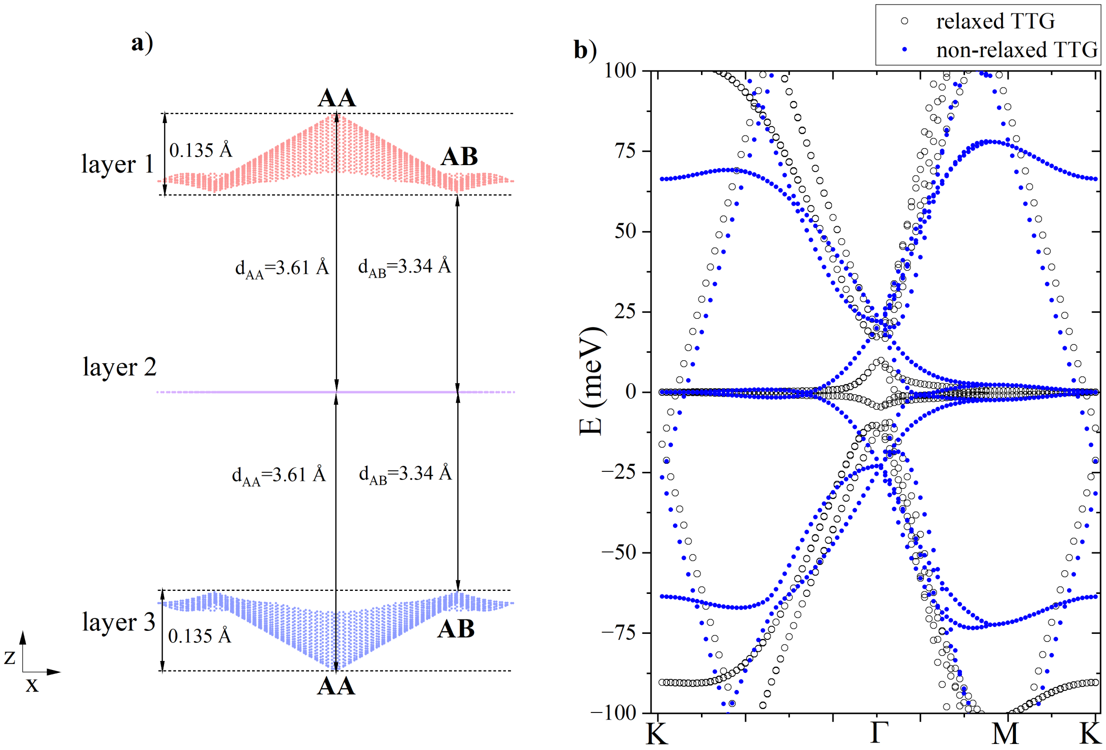

Figure C.1: Relaxation details: (a) Schematic side view of relaxed TTG layers. The interlayer distance varies across the moiré unit cell depending on the local stacking. The middle layer remains rigid and top/bottom layers are adjusted. The layers are closest in the AB-stacked regions, where the interlayer spacing is $d_{\mathrm{AB}} = d_{\mathrm{min}} = 3.34\,\text{Å}$. The largest separation occurs in the AA-stacked regions, where $d_{\mathrm{AA}} = d_{\mathrm{max}} = 3.61\,\text{Å}$. (b) Band structure of non-relaxed and relaxed TTG denoted by blue dots and black circles, respectively. No gap between the flat and remote bands is observed for non-relaxed structure. Relaxation leads to flattening of the flat band, renormalization of the remote bands, and gaps opening between the flat and the remote bands at the Γ point.